Measurement and Manipulation in Microchannels using AC Electric Fields

by

Paul Wood
BASc, University of Waterloo, 2007

A Dissertation Submitted in Partial Fulfillment
of the Requirements for the Degree of

MASTER OF APPLIED SCIENCE

in the Department of Mechanical Engineering

Supervisory Committee

Measurement and Manipulation in Microchannels Using AC Electric Fields
by

Paul Wood
BASc, University of Waterloo, 2007

Supervisory Committee

Dr. David Sinton (Mechanical Engineering)
Supervisor

Dr. Rustom Bhiladvala (Mechanical Engineering)
Departmental Member

Dr. Alexandre Brolo (Chemistry)
Outside Member

Abstract

Supervisory Committee
Dr. David Sinton (Mechanical Engineering)
Supervisor
Dr. Rustom Bhiladvala (Mechanical Engineering)
Departmental Member
Dr. Alexandre Brolo (Chemistry)
Outside Member

In this work, alternating current (AC) electric fields are used in combination with microfluidics to manipulate micro- and nano-sized particles and to probe the electrical characteristics of microchannels with potential application in portable diagnostics. This work was carried out as contribution to a collaborative research project involving researchers from chemistry, electrical engineering and mechanical engineering at the University of Victoria, in addition to researchers from the BC Cancer Deeley Research Centre.

The manipulation of particles or cells within a microchannel flow is central to many microfluidic applications. In the context of diagnostics that utilize antibodies in serum, for example, the removal of cells from the sample is often required. Continuous removal of particles and cells is particularly critical in the case of flow-through nanohole array based sensing, as these serve as fine filters and thus are very susceptible to clogging. In this work, chevron shaped, interdigitated electrodes are used to produce dielectrophoretic forces in combination with hydrodynamic drag to displace particles from their corresponding streamlines to the center of a microchannel. Analytical and finite element modeling are used to provide insight into the focusing mechanism.

Dielectrophoresis (DEP) also offers opportunities for particle manipulation in combination with porous media. In this preliminary work, the viability of dielectrophoresis tuned nano-particle transport in a nanohole array is investigated through analytical and numerical modeling. The effects of hydrodynamic drag and Brownian motion are considered in the context of applied voltage, flow rate and particle size. Preliminary flow-through tests are performed experimentally as proof of concept.

The final contribution focuses primarily on external infrastructure that enables AC microfluidic diagnostics, with particular relevance to portable device applications and so-called point-of-care devices. Cell phones, and mp3 players are examples of consumer electronics that are easily operated and are ubiquitous in both developed and developing regions. Audio output (play) and input (record) signals are voltage-based and contain frequency and amplitude information. Audio signal based concentration, conductivity, flow rate, and particle detection measurements are demonstrated in a microfluidic platform.

Table of Contents

List of Figures

Nomenclature

Symbol	Description	Units
A_C	Cross-sectional area	m^2
A_S	Surface area	m^2
Λ	Molar conductivity	$S \cdot m^2/mol$
α	Shear rate	1/s
Ca	Capillary Number	-
c	Concentration	mol/m^3
C	Capacitance	F
D	Diffusivity	m^2/s
e	Elementary charge	$1.60217646 \times 10^{-19}$ C
ε, ϵ	Permittivity	F/m
$\varepsilon_0, \epsilon_0$	Permittivity of free space	8.854187×10^{-12} F/m
E	Electric field strength	V/m
F	Faraday's constant	96485 C/mol
F	Force	N
f	Frequency	Hz
g	Gravitational constant	$9.81 m/s^2$
γ	Surface tension coefficient	N/m
h	Planck's constant	$6.6260698 \times 10^{-34}$ m^2kg/s
I	Intensity	W/m^2

$Im[\ ]$	Imaginary part	-
j	Imaginary unit	-
j^*	Molar flux	$mol/m^2 \cdot s$
K_{cell}	Cell constant	-
k	Boltzmann constant	$1.3806504 \times 10^{-23}$ J/K
KE	Kinetic energy	J
$K(\omega)$	Clausius-Mossotti factor	-
L	Length	m
λ	Wavelength	m
λ_D	Debye length	m
m	Mass	kg
μ	Dynamic viscosity	Pa·s
N_A	Avogadro's number	6.0221415×10^{23}
p	Pressure	Pa
p	Dipole moment	D
Pe	Peclet number	-
Φ	Potential	V
q	Charge	C
R	Universal gas constant	8.314 kJ/K·mol
R	Resistance	Ω
r	Radius	m
Re	Reynold's Number	-
$Re[\ ]$	Real part	-

ρ	Density	kg/m^3
σ, ρ	Charge density	C/m^2
σ,κ	Conductivity	S/m
T	Temperature	K
t	Time	s
τ	Time constant	s
U_e	Potential energy	J
V	Velocity	m/s
$\forall$	Volume	m^3
v	Ion mobility	$m^2/V \cdot s$
ω	Frequency	rad/s
z	Valence number	C
ξ	Zeta potential	mV

Acknowledgments

There are several people who have made this work possible and to whom I owe thanks. I am greatly appreciative of my supervisor and mentor, David Sinton, for his insights, guidance, and patience as I develop as a researcher. His confidence in my work inspires me to take risks and continue improving.

I would like to thank everyone from the lab-on-chip nanohole sensors project, particularly Alex Brolo and Reuven Gordon, for their ongoing feedback and for sharing their expertise on a near weekly basis. Their input to this work has been invaluable.

I would like to thank everyone from the microfluidics lab: Ali Kazemi for showing me the ropes and passing down his microfabrication knowledge, Slava Berejnov for answering every question I've ever had about anything, Carlos Escobedo for his insights and enthusiasm, Joe Wang for most things chemistry related, Brent Scarff for bringing baby cookies to my attention, and to everyone for making lab time fun.

I would like to thank Roger Khayat at the University of Western Ontario for allowing a high school student to work in his research lab and for steering me in the direction of engineering. I'd also like to thank all my past teachers who encouraged curiousity. Lastly, I express a deep gratitude to my family for their support in countless school science projects and all my endeavours, and to my girlfriend Lisa for her ongoing patience, encouragement, and contagious enthusiasm.

1.0 Introduction

1.1 Microfluidics and the Marketplace

Microfluidics is the science and technology of systems that process or manipulate small (10^{-9} to 10^{-18} litres) amounts of fluid, using channels with characteristic dimensions ranging from 1-1000 micrometres. Microfluidic technologies were first used in analysis where they offered numerous useful capabilities, including the ability to use very small quantities of samples and reagents, to carry out separations and detection with high resolution and sensitivity, low cost, short time for analysis, and small footprints for analytical devices [Whitesides (2006)].

The first conceptual and experimental papers on micro total analysis systems, published in 1990 and 1993 respectively, mark pivotal moments in microfluidics' relatively short history [Manz et al. (1990), Harrison et al. (1993)]. The visionary appeal and interdisciplinary nature of the field has lead to its rapid growth and adoption in research programs across a variety of disciplines in science and engineering, as evidenced by growing numbers of publications and patents [Kamholz (2004)]. Many of the advantages associated with microscale regimes, such as reduced reagent volume, parallel processing, and portability are intuitive; but as experimentation with micro scale phenomena yields counter-intuitive results, scientists are uncovering new inherent functionality with unexpected promise. By understanding and leveraging micro scale phenomena, scientists are able to perform techniques not possible on the macro scale, allowing new functionality and experimental paradigms to emerge [Beebe (2002)]. For these reasons, microfluidics, in the context of micro total analysis systems, has emerged as a disruptive technology. By definition, a disruptive technology is one in which products dramatically change markets due to their performance, and are not achievable by simple linear extrapolation of existing products or technologies [Moore (2002)].

The notion of an integrated total analysis tool, whether used for medical diagnostics, analytical chemistry, food analysis or bio-threat detection, is appreciated both by those working within the field, as well as those engaged in other technical or non-technical fields [Becker (2009a)]. In microfluidics, the swift endorsement of a new,

disruptive technology started a process, which has been observed with other technologies, known as the Gardner hype cycle [Fenn and Raskino (2008)]. Since the mid 1990s, the Gardner Hype Cycle, shown for microfluidics in Figure 1, has been used to describe the maturing of new disruptive technologies facing conflicting expectations and technological deliverables [Becker (2008)]. In the first stage of the cycle, a "technology trigger" launches an innovation through invention with serendipitous timing and market uptake. In the context of microfluidics, this trigger can be tied to the first conceptual paper on micro total analysis systems, published in 1990 [Manz et al. (1990)]. The "technology trigger" initiates the start of a technology hype which culminates in the "peak of inflated expectations" [Becker (2009b)]. The growth in technology hype in microfluidics spanned roughly a decade, from 1990 to 2000, during which time microfluidics was expected to revolutionize practices in biology and chemistry. During this time, microfluidics was featured both in Time magazine [Gorman et al. (1999)] and on the cover of Forbes magazine [Moukheiber (1998)]. Companies including Caliper, Aclara, Nanogen and Orchid Biocomputers were founded and declared initial public offerings (IPOs) fuelling the excitement with economic prospects. During this time, microfluidic applications were proposed with the expectation that they would generate large revenues with attractive profit margins in a relatively short amount of time. Such applications have been coined "killer applications".

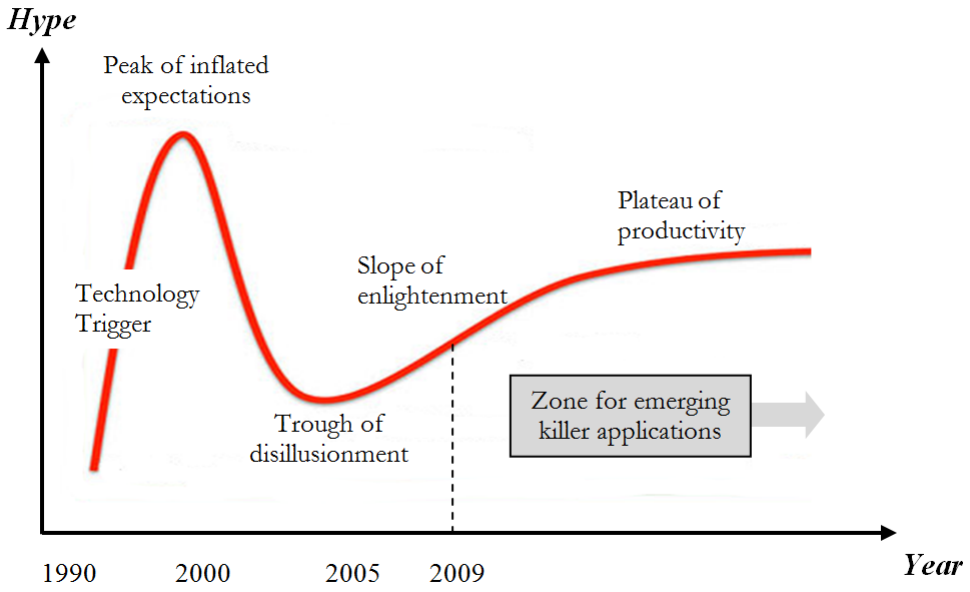

Figure 1.1: Gardner hype cycle for microfluidics.

Not surprisingly, microfluidics did not meet these lofty expectations; revenues did not grow as expected, start-up companies folded, and the promise of revolution in the life sciences failed to materialize. Failure to meet expectations then triggered the next stage of the hype cycle, the "trough of disillusionment"; this has been speculated to have occurred in 2004 [Becker (2009b)]. Much of the visionary appeal of microfluidics had dissipated for investors and others not actively involved in the field, but despite this fact, microfluidics had a strong scientific, technological and manufacturing base and remained advantageous over many currently employed practices in biology and chemistry. A second wave of start-up companies employing microfluidics in their products are now appearing, signalling the onset of the slope of enlightenment on the Gardner Hype Cycle. Microfluidics has gone from being viewed as a stand-alone technology, as in the case of micro total analysis systems, to an enabling technology or tool that can be applied in a variety of formats analogous to microelectronics.

That being said, currently there is no "killer application" for microfluidics. Instead microfluidics is used in a variety of smaller niche applications such as capillary electrophoresis chips for genetic analysis, microfluidic chips for protein crystallization, and point-of-care diagnostics among others. At present all of these applications are either

in early development stages or at a comparatively early stage in their product life cycle [Stephan (2004)]. The microfluidic industry as a whole is a relatively large size, however products are not directed towards end-user markets where they are purchased by private customers, but rather are sold in a business to business configuration which includes the research and academic market. As a result, commercial volumes and revenues generated per product are comparatively low [Stephan (2005)]. "Killer applications" will likely result only during the transition from products sold between businesses to products sold to a consumer market. The first so-called killer applications are expected to appear in high-end markets; that is high in both price and performance, such as cancer diagnostics. Penetration into more cost-sensitive markets with higher volumes tends to follow from success in high-end markets [Becker (2009a)]. Labour intensive manufacturing methods with low up front capital costs are well suited for prototyping a variety of design concepts in research environments, but as the field of microfluidics grows commercially, device development efforts will have to increasingly rely on designs for manufacturability at high volumes.

From an academic standpoint, the progress to date in microfluidics has been highly admirable; the field continues to be dynamic and there is a growing emphasis on application development. Knowledge of microscale fluid phenomena and experimental techniques have advanced at a rapid pace. The development of soft lithography [Duffy et al. 1998] in microfluidics has facilitated low-cost device prototyping in academic settings, expediting the process from concept development to testing.

The interdisciplinary nature of the field has unified scientists from otherwise disparate fields who are now applying their highly specialized skills to a breadth of fundamental problems across all areas of science and engineering. The fundamentals of microfluidics are notable: much of the world's technology requires the manipulation of fluids, and extending those manipulations to small volumes, with precise dynamic control over concentrations, while discovering and exploring new phenomena occurring in fluids at the microscale has relevance in many fields [Whitesides (2006)].

Nanofluidics is the study of fluids confined to structures with characteristic dimensions on the order of nanometers. The overwhelming influence of diffusion and exceedingly high surface area to volume ratios on the nanoscale distinguishes this size

regime from its micro scale counterpart. With the Gardner Cycle of microfluidics in recent memory, the growth of nanofluidics has been more monotonic [Eijkel and van den Berg (2005)]. One area in which nanofluidics has been demonstrated to offer significant advancements is in transport of reactants to surface-based sensors via rapid diffusion [Schoch et al. (2008)]. Such an approach is particularly well suited to sensors that utilize nanostructures for sensing through vibrational or photonic modes [Erickson et al (2007)].

1.2 Aims and Motivations

This work involves the development of practical microfluidic technology for use in biomedical diagnostic with a specific focus on alternating current (AC) electric fields. The use of AC electric fields in microfluidic environments can enable particle manipulation, sorting, mixing and pumping. The study and application of AC electric fields in microfluidics was the original motivation of this work, starting in September 2007. In October 2007, a strategic grant award was received by Drs. David Sinton, Alex Brolo and Reuven Gordon to fund the development of lab-on-chip nanohole array sensors for cancer diagnostics. At this time, the original scope of this work was modified to serve the needs of the newly awarded grant. The resulting work is my contribution to this collaborative research project that involves researchers from Chemistry, electrical engineering and mechanical engineering departments at the University of Victoria, in addition to researchers from the BC Cancer Deeley Research Centre. Within the context of this project, AC electric fields have applicability in the control of particles and cells as sample preparation and concentration for sensing, as well as monitoring the microfluidic environment including sensing bulk concentration, bulk flow rate, and particle transport.

1.3 Thesis Overview

In this work, alternating current (AC) electric fields are used in combination with microfluidics to manipulate micro- and nano-sized particles and to probe the electrical characteristics of microchannels with potential application in portable diagnostics. The

contributions of this thesis include three works, presented sequentially in chapters four, five and six; there are seven chapters in total.

In Chapter 1, a brief history of microfluidics provides context for the subsequent aims and motivations of the thesis. Chapter 2 includes a brief overview of experimental methods including micro- and nanoscale fabrication methods and sample visualization techniques. In Chapter 3, micro- and nanoscale transport phenomena are discussed, covering all hydrodynamic, charge, and dipole based interactions relevant to chapter four through six. Chapter 4 discusses a continuous particle focusing scheme based on dielectrophoresis and a planar electrode configuration. Particle dynamics are studied with a combination of analytical and numerical modelling, and experiments are carried out as proof of concept. In Chapter 5, dielectrophoretic based particle manipulation is extended to three dimensional electrode structures under the context of enhancing the utility of surface plasmon resonance based sensors. Once again particle dynamics are studied using a combination of analytical and numerical modelling. A strong emphasis is placed on the fabrication with basic operation and flow visualization demonstrated as proof of concept. In Chapter 6, a demonstration of audio signals to achieve on-chip electrochemical diagnostic tests is reported. Application of theory and experimental results support the utility of portable consumer electronics such as cell phones, mp3 players and laptops equipped with sound cards in interfacing with impedance based microfluidic devices towards portable, point-of-care diagnostics. The thesis is concluded in Chapter 7 where major contributions are summarized and potential for future work is highlighted.

2.0 Experimental Methods

2.1 Introduction

While the term *microfluidics* was coined in the 1990's, microfluidic devices first appeared in the late 1970's and, at this time, were fabricated in silicon and glass. The first fully integrated gas chromatography system was demonstrated on a silicon wafer [Terry et al. (1979)] in 1979. To date, this paper has received more than 300 citations but long went unrecognized, receiving most of those citations after the formal introduction of micro total analysis systems in 1990. When microfluidics emerged as a new field, it was hoped that photolithography and associated technologies that had been successful in microelectronics, and in microelectromechanical systems (MEMS), would be directly applicable to microfluidics. Silicon and glass, however, have been largely displaced by plastics. Silicon, in particular, is expensive, and opaque to visible and ultraviolet light, so cannot be used with conventional optical methods of detection. Glass has desirable optical properties but gas impermeability poses issues when working with living cells. Furthermore, the glass etching process used to create microchannels typically requires hydrofluoric acid; a chemical known to be extremely corrosive, requiring extreme care and precautions when handling.

Much of the exploratory research in microfluidics has been carried out in a polymer called poly(dimethylsiloxane) or PDMS [Whitesides (2006)]. PDMS is optically transparent at wavelengths down to 280nm, deformable, non-toxic, and can seal reversibly or irreversibly through the formation of covalent bonds [McDonald et al. (2000)]. The ease with which new concepts can be tested in PDMS and its ability to embody useful components, such as pneumatic valves, have made it the key material for exploratory research and engineering at early stages of microfluidics development. PDMS is, however, susceptible to solvent swelling and surface adsorption. More specialized systems requiring chemical and thermal stability can be created in glass, silicon or even steel. Other polymers, such as poly(methyl methacrylate) or PMMA have also been used in combination with adhesives and laser ablation techniques [Wang et al. (2009), Wu and Nguyen (2005)].

Beyond material selection, there are fundamentally two ways to make things very small: using a “top-down approach” or a “bottom-up” approach [Zhang et al (2004)]. The “top-down” approach uses tools to remove material from an object to create the final product. Techniques used to create micro- and larger nano-sized features such as electrical discharge micromachining (EDM), photolithography and focused ion beam (FIB) milling, fall under this category. The bottom up approach involves assembling smaller building blocks, typically to create materials spanning nanometers. Interestingly, microfluidics can serve as an enabling tool for bottom up techniques such as particle self-assembly [Schabas (2008)]. In the work described herein, all employed fabrication techniques can be categorized as “top-down” approaches.

2.2 Focused Ion Beam Milling

Focused Ion Beam (FIB) milling is a maskless etching technique. The basic FIB instrument consists of a vacuum system and chamber, a liquid metal ion source (typically Gallium), an ion column, a sample stage, detectors, gas delivery system, and a computer to run the complete instrument [Giannuzzi and Stevie (2005)]. A simple schematic of a focused ion beam (FIB) system is shown below:

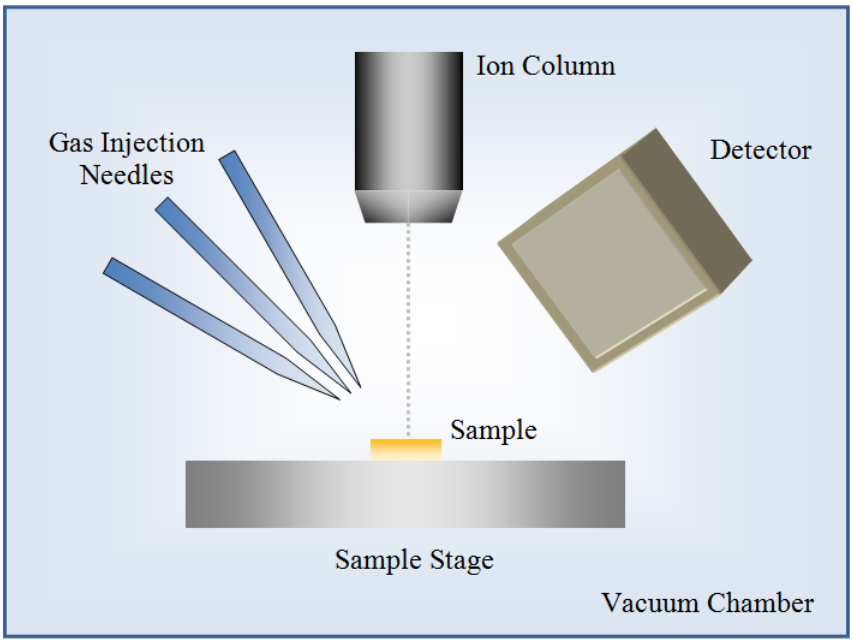

Figure 2.1: Schematic of a basic focused ion beam (FIB) system.

FIBs produce a focused beam of positive ions that can be used for imaging, milling, or even depositing material on a surface. Ion currents are adjusted for each operating mode, with milling requiring the highest current. Ions are well suited to the milling process, carrying more mass than electrons and thus offering a greater impact through momentum transfer during the milling process [Orloff et al. (2002)]. In this work, focused ion beam milling was employed to fabricate arrays of nano-sized through-holes. The fabrication was conducted at Simon Fraser University (SFU) by collaborating group member Fatima Eftekhari.

2.3 Photolithography

There are several families of lithography including: X-ray, electron, and optical. In microfluidics, optical lithography that exploits the spectral band in the upper UV range, between 300 and 450 nm, is the most common [Tabeling (2006)]. Optical or photolithography is a micro fabrication process that uses light to transfer a geometric pattern from a photomask to a light-sensitive chemical photoresist. There are two

categories of photoresist: positive and negative. When using the appropriate solvent, positive photoresists become soluble when exposed to UV light while exposed portions of negative photoresist become insoluble. The photoresist must be both sufficiently transparent to allow the illumination of the whole thickness of the deposited layer and sufficiently sensitive to the light to induce chemical reactions. This delicate balance limits the thickness of a large number of photoresists. SU-8, developed at IBM, is a negative photoresist unique in its ability to be deposited in thick (tens of microns) layers while maintaining high photosensitivity [Tabeling (2006)]. As a result, it has become the gold standard in microfluidics-directed fabrication.

The minimum feature size acheivable by photolithography is dictated by diffraction; the scattering of light when it encounters obstacles comparable to its wavelength. As incident light strikes the micron size features of the photomask diffraction occurs at the edges of these features. The size of the region affected by diffraction, δ, as shown in Figure 2.2, is dependent on the wavelength of light used in exposure as well as the thickness of the photoresist [Tabeling (2006)].

$$\delta \approx 3\sqrt{\lambda s} \tag{2.1}$$

Here, δ is roughly the width of the diffraction zone, λ is the wavelength of the incident light, and s is the height of the photoresist coating. Within this diffraction region, the photoresist is exposed to light, of lower intensity than the incident light, and may be polymerized rendering it insoluble where a negative photoresist is used. This is problematic where closely spaced features are employed and precise feature dimensions are required.

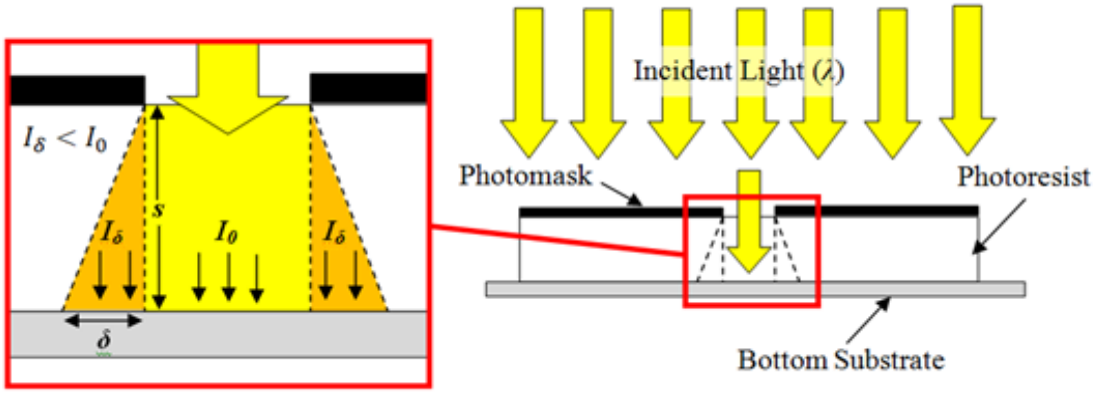

Figure 2.2: The geometry patterned on a photomask is transferred to a photoresist coated substrate using photolithography. The regions of photoresist receiving direct and diffracted light, respectively, are shown on the left.

In Figure 2.2, I_δ and I_0 are the light incident and diffracted light intensity respectively. In the case where micron sized features are closely spaced, a minimum spacing of 2δ is required to create distinct features.

Photolithography and soft lithography procedures for fabrication of microfluidic devices are now well established and thus have not been covered in detail here. For a more detailed description of the photolithography and soft lithography process used in microfluidics, the reader is referred to a number of previous theses written by this research group [Mckechnie (2006), Schabas (2007), Oskooei (2008)].

2.4 Fluorescence Microscopy

Fluorescence microscopy is a technique that has been well developed for visualization of cell components and biological mechanisms [Rost (1992)]. It has also been employed for direct visualization of a number of processes in microfluidics, including cross stream diffusive mixing [Kamholz and Yager (2001)], particle motion in optical traps [Blakely et al. (2008)], and the onset of flow at nanofluidic-microfluidic junctions [Eftekhari et al. (2009)].

Aptly named, fluorescence microscopy operates using the principle of fluorescence. Fluorescence is a process by which molecules excited by electromagnetic radiation almost immediately emit a photon [Guilbault (1990)]. The process can be summarized into three stages [Sinton (2004)]: (i) a photon is absorbed by a fluorophore, increasing its energy to an excited state; (ii) the fluorophore remains in this excited state for a finite period, called the fluorescence lifetime, which typically lasts 1-10 ns; (iii) the fluorophore then releases this photon returning to its ground state. During this process, some of the absorbed energy from the photon is dissipated through interactions with other molecules, conformal changes, and energy dissipating vibrations [Sinton (2004)]. In accordance with the equation for the energy of a photon, shown below, the emitted photon is of lower energy and thus longer wavelength.

$$Energy = \frac{h \times (speed\ of\ light)}{\lambda} \tag{2.2}$$

where h is Planck's constant and λ is the wavelength of the associated electromagnetic wave. The difference in wavelength between the absorbed and emitted photon is called the Stokes' shift [Sinton (2004)]. The Stokes' shift is specific to the type of fluorescent particle used in experiments.

The operating principle of fluorescence microscopy is shown schematically in Figure 2.3. A filter cube equipped with a dichroic mirror facilitates the selective transmission of specific wavelengths required to observe fluorescence. The filter cube consists of two perpendicular filters, the excitation and emission filters, with a dichroic mirror positioned between them at a 45^{o} angle. The excitation and emission filters permit only that light which is in the excitation and emission wavelength range of the fluorescent sample respectively. The dichroic mirror is selectively transparent to the longer wavelength and reflects the shorter wavelength, and is thus able to direct light. After passing through the excitation filter, excitation light is reflected downwards through the microscope objective onto the fluorescent sample. Once a Stokes' shift takes place, the light is re-emitted at a longer wavelength where it travels upwards passing through the dichroic mirror and emission filter before reaching the detector [Schabas (2007)].

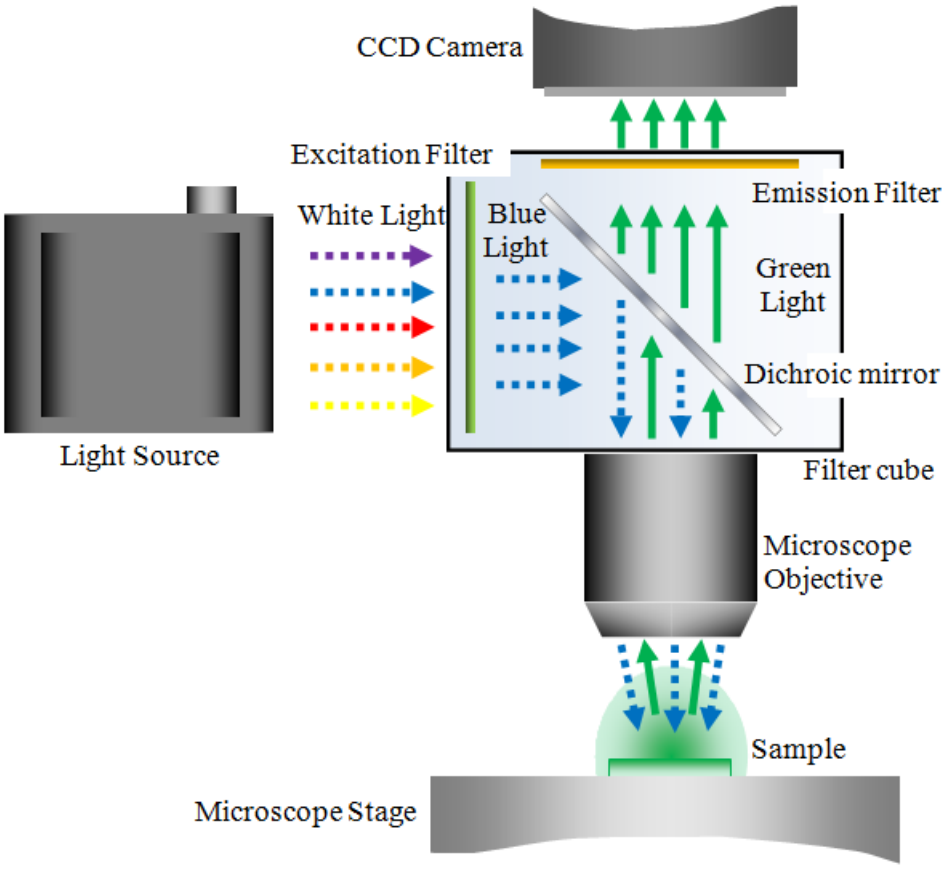

Figure 2.3: Schematic illustrating the operation of a microscope used to image fluorescent samples.

3.0 Microscale Transport Phenomena

This chapter provides an overview of the microscale transport phenomena relevant to the core contributions of this work. These core contributions are presented in chapters 4, 5 and 6 in a more manuscript style format.

Microfluidics refers to fluid flow in channels and structures with characteristic dimensions on the order of 1-1000 μm; for reference, a human hair is typically 50-100 μm in diameter. Microfluidic channels, while very small, can be found in systems varying in size by orders of magnitude. Trees, the human body, ink-jet printers, fuel cells, and genetic analysis microchips vary greatly in both size and application, but all carry out specific tasks made possible by leveraging microscale transport phenomena. The same laws of physics that govern our macro environment also apply to the micro scale, but, for a variety of reasons, downsizing drastically alters the observed behaviour of fluids. These flow regimes often contradict daily experiences with fluids in human scale environments, and thus lead to counter-intuitive results at the micro scale [Squires and Quake (2005)]. For example, high surface to volume ratios, high rates of heat and mass transport, elektrokinetic effects, laminar flow regimes and accurate control of force fields are all characteristic of microfluidic flows distinguishing them from their macro-scale counterparts.

3.1 Convection

The continuum assumption forms the basis of most micro- and even nano-scale flow theory. This assumption is valid where molecular spacing, or mean free path in the case of gases, is significantly less than the characteristic dimension of the flow. Under such conditions discrete quantities like mass and force give way to continuous fields like density and force density that are defined per unit volume [Squires and Quake (2005)]. The velocity field for a Newtonian fluid obeys the Navier-Stokes equations which, for incompressible fluids such as liquids or gases at low Mach numbers, will read in vector form:

$$\overbrace{\rho\Big(\underbrace{\frac{\partial\vec{V}}{\partial t}}_{\text{Unsteady acceleration}}+\underbrace{\vec{V}\cdot\nabla\vec{V}}_{\text{Convective acceleration}}\Big)}^{\text{Acceleration term}}=\overbrace{\underbrace{-\nabla p}_{\text{Pressure gradient}}+\underbrace{\mu\nabla^2\vec{V}}_{\text{Viscosity}}}^{\text{Surface forces}}+\underbrace{\rho\vec{g}}_{\text{body forces}} \tag{3.1}$$

While this equation can be applied to both macro- and micro-sized flows, several unique phenomena are inherent only on the microscale. One such characteristic is the preservation of low Reynolds number at high velocities. The Reynolds number, shown below, is a dimensionless quantity describing the relative influence of inertial and viscous forces on flow behaviour [White (2003)].

$$Re=\frac{\rho U l}{\mu} \tag{3.2}$$

Here, ρ is the fluid density, U is the characteristic velocity, l is the characteristic length, and μ is dynamic viscosity of the fluid. The Navier-Stokes equation can be non-dimensionalized using the characteristic velocity, U, and length, l, as scaling parameters:

$$\vec{V}^*=\frac{\vec{V}}{U};\ t^*=\frac{t}{l/U};\ \nabla^*=\frac{\nabla}{1/l};\ p^*=\frac{p}{\mu U/l};\ g^*=\frac{g}{U^2/l};\ \text{substituting} \tag{3.3a}$$

$$\frac{\rho U^2}{l}\left(\frac{\partial\vec{V}^*}{\partial t}+\vec{V}^*\cdot\nabla\vec{V}^*\right)=-\frac{\mu U}{l^2}\nabla^* p^*+\frac{\mu U}{l^2}\nabla^{*2}\vec{V}^*+\frac{\rho U^2}{l}g^*;\ \text{rearranging} \tag{3.3b}$$

$$Re\left(\frac{\partial\vec{V}^*}{\partial t}+\vec{V}^*\cdot\nabla\vec{V}^*-\rho g^*\right)=-\nabla^* p^*+\nabla^{*2}\vec{V}^* \tag{3.3c}$$

Using this selection of scaling parameters, when inertial forces are small compared to viscous forces, as is the case at low Reynolds number (*Re<1*), the non-linear inertial and body force terms can be neglected. The Navier-Stokes equation then simplifies to the Stokes equation:

$$-\nabla p+\mu\nabla^2\vec{V}=0 \tag{3.4}$$

The continuity equation is given as:

$$\frac{\partial \rho}{\partial t} + \nabla \cdot \left(\rho \vec{V}\right) = 0 \tag{3.5a}$$

$$\nabla \cdot \vec{V} = 0 \tag{3.5b}$$

It is important to note that the unsteady term vanishes when time is non-dimensionalized using the convective timescale of the flow. There are cases in practice when this scaling is inappropriate and unsteady effects cannot be neglected in small scale flows [Lin et al. (2008)]. This topic will be revisited later in thesis where the position and drag on a particle in a microchannel is considered.

Density, ρ, is constant for the case of incompressible flow. Without inertial non-linearity, microfluidic systems have regular, deterministic flows. Consequently, velocity distributions in microchannel-based pressure driven flows can be solved analytically. Furthermore, body forces, such as those induced by applied magnetic or electric fields, can be accurately predicted and engineered. At steady state, in the absence of body forces, analytical solutions have been derived for channels of rectangular cross section as commonly used in microfluidics. The velocity profile in a microchannel with a rectangular cross section is given as [Nguyen and Wereley (2002)]:

$$u(y,z) = \frac{16a^3}{\mu\pi^3}\left(-\frac{dp}{dx}\right)\sum_{i=1,2,\ldots}^{\infty}(-1)^{(i-1)/2}\left[1 - \frac{cosh(i\pi z/2a)}{cosh(i\pi b/2a)}\right]\frac{cos(i\pi y/2a)}{i^3} \tag{3.6}$$

where *2a* and *2b* are the width and height of the microchannel respectively. In channels with large width to height aspect ratios (>10:1), shown in Figure 3.1, a two-dimensional Poiseuille flow approximation is valid everywhere outside of the region within about one channel height from the side walls [Deen (1998)].

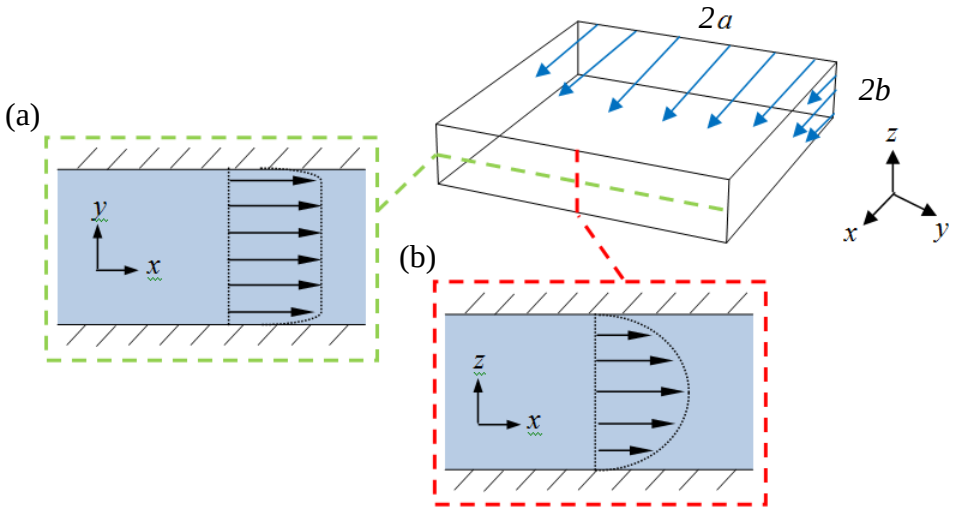

Figure 3.1: Velocity profile for pressure driven flow along the (a) width and (b) height of a rectangular microchannel.

3.2 Particles in Low Reynolds Number Flows

The advective motion of small particles relative to the fluids in which they are immersed can be classified into several processes: (i) particles may move together in bulk through a fluid, (ii) they may move relative to one another owing to shearing motion of the suspending fluid, or (iii) particles may remain stationary as in a packed bed [Happel and Brenner (1973)]. In this work, we consider particles moving together in a bulk dilute solution such that there are negligible interactions between particles; particle-wall interactions, however, are considered.

Particles suspended in a fluid may experience a net force arising from the difference between the density of a particle and the density of its surrounding medium. In this instance, a particle is subject to both buoyancy force and gravity, or what is often termed buoyancy corrected particle weight. The buoyancy force will be equivalent to the weight of fluid displaced by the object, while the gravitation force acting on an object is independent of its surrounding medium. For an object fully immersed in fluid its buoyancy corrected weight is:

$$F_{net} = (\rho_f - \rho_o)\forall_o g \tag{3.7}$$

where ρ_f is the density of the fluid, ρ_o is the density of the object, $\forall_0$ is the volume of the object, and g is acceleration due to gravity. When the density of the particle and surrounding medium are equal, the force of gravity and buoyancy will be equal, and no net force will arise.

Low Reynolds number flows are governed by Stokes' equations, and thus particles suspended in this flow regime are subject to Stokes' drag. In this case, the drag force is proportional to velocity but opposite in direction [Vogel (2003)]:

$$\vec{F}_{drag} = -b\vec{V} \tag{3.8}$$

where b is a constant that depends on the properties of the fluid and the dimension of the object, and V is the relative velocity of the object and surround medium. For the case of a spherical particle traveling in an infinitely quiescent fluid the equation for Stokes' drag becomes [Vogel (2003)]:

$$\vec{F}_{drag} = -6\pi\mu r_p\vec{V} \tag{3.9}$$

where μ is the dynamic viscosity of the surrounding fluid and r is the radius of the sphere. Inherent in this formulation is an assumption of no slip at the surface of the sphere.

When particles are suspended in microchannel flows, they are often travelling in proximity to channel walls. For the case of particles in shearing flow between two parallel walls, as shown in Figure 3.2, Faxen's Law [Happel and Brenner (1973)] gives the following relation for drag force:

$$F_{DRAG} = \frac{6\pi\mu\, r_p}{\beta} V; \quad \text{with}$$

$$\beta = \left[\frac{1-0.6526\left(\frac{r_p}{h}\right)+0.4003\left(\frac{r_p}{h}\right)^3-0.297\left(\frac{r_p}{h}\right)^4}{\left({}^3/_2\right)}\right] \tag{3.10}$$

where h is the distance between the center of the particle and the wall. This relation is also valid for Poiseuille flow between parallel plates when the diameter of the particle is significantly smaller (<50 times) than the height of the channel. Often, particles flowing in a microchannel have diameters in the same order of magnitude as the channel height. When a particle is travelling in proximity to two parallel, stationary, infinite no slip surfaces, Faxen's law can be extrapolated to give [Wakiya (1957)]:

$$F_{DRAG} = \frac{6\pi\mu r_p}{\beta} V; \text{ with}$$

$$\beta = \frac{1-0.6526\left(r_p/h\right)+0.3160\left(r_p/h\right)^3-0.242\left(r_p/h\right)^4}{1-(1/9)\left(r_p/h\right)^2} \tag{3.11}$$

This equation applies to the specific case of a particle flowing at a distance, h, from the channel wall where the distance between walls is 4h as shown in figure 3.2.

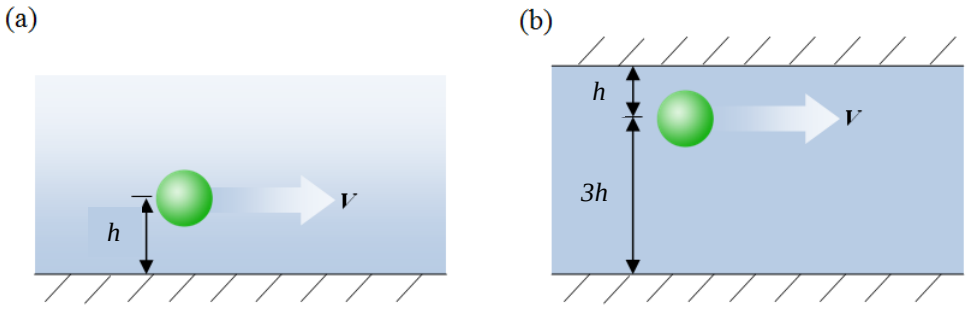

Figure 3.2: A spherical particle traveling close to (a) a single, infinite no-slip surface and (b) a particle traveling between two parallel, infinite no-slip surfaces.

The last case to be considered is that for a spherical particle moving axially along a tube of circular cross-section. For a spherical particle traveling along the center of a tube of circular cross-section under Poiseuille flow, analytical solutions are available [Happel and Brenner (1973)]. The solution developed by Haberman and Sayre [Haberman and Sayre (1958)] is most robust, having also considered cases of very large particle diameter to tube diameter ratios (>0.6). The drag force acting on a sphere under such conditions is given as [Haberman and Sayre (1958)]:

$F_{drag} = 6\pi\mu r_p\left(\overrightarrow{V_p}K_1 - \vec{V}_0 K_2\right)$; where

$K_1 = \frac{1-0.75957\left(r_p/R_0\right)^5}{1-2.1050\left(r_p/R_0\right)+2.0865\left(r_p/R_0\right)^3+0.72603\left(r_p/R_0\right)^6}$; and

$$K_2 = \frac{1-(2/3)\left(r_p/R_0\right)^2-0.20217\left(r_p/R_0\right)^5}{1-2.1050\left(r_p/R_0\right)+2.0865\left(r_p/R_0\right)^3-1.7068\left(r_p/R_0\right)^5+0.72603\left(r_p/R_0\right)^6} \quad (3.12)$$

Here, R_0 is the radius of the circular, cylindrical tube, $\vec{V}$ is the velocity of the particle, and $\overrightarrow{V_p}$ is the approach velocity of the fluid at the center of the tube.

3.3 Diffusion

As a further consequence of laminar flow, mixing in microchannels is generally driven by diffusion only. Nevertheless, the rates of heat and mass transfer are more pronounced at short length scales. For example, haemoglobin in water takes 10^6 seconds to diffuse 1 cm, but only 1 second to diffuse 10 μm [Beebe (2002)]. Assuming that fluid density and viscosity are independent of concentration, the concentration distribution does not influence the flow field. This allows the hydrodynamic problem to be decoupled from the mass transfer problem [Bird et al. (1960)]. Assuming a constant diffusion coefficient, the conservation of individual species is then given by the convection-diffusion equation:

$$\underbrace{\frac{\partial c}{\partial t} + \vec{V}\cdot\nabla \mathrm{c}}_{\text{convective mass transfer}} = \underbrace{D\nabla^2 c}_{\text{diffusive mass transfer}} \quad (3.13)$$

Here, c is the concentration of the species of interest, and D is the diffusion coefficient. The convection-diffusion equation considers only ordinary diffusion in accordance with Fick's Law, neglecting other forms of species transport such as electro-migration

[Probstein (2003)]. Smaller particles will diffuse more rapidly than larger particles. The relative influence of advection and diffusion is characterized by the Peclet number:

$$Pe = \frac{\vec{V}_{avg} L}{D} \tag{3.14}$$

where $\vec{V}_{avg}$ is average flow velocity, *L* is the characteristic length, and *D* is the diffusion coefficient. At very low Peclet numbers, the convection term becomes negligible and mass transport is dominated by diffusion. Conversely, at very large Peclet numbers the diffusion becomes negligible and mass transport is dominated by convection. In typical microfluidic applications, Peclet numbers fall into the intermediate range where both phenomena contribute to mass transport.

3.4 Brownian Motion

Brownian motion is the seemingly random movement of particles suspended in a fluid; which results from asymmetry in kinetic impacts of molecules that make up the fluid [Einstein (1956)]. This form of diffusion becomes increasingly apparent as particle size approaches the sub-micron size range, coming within orders of magnitude of water molecules, which are typically 0.2 nm in size [Cook et al. (1974)].

In the absence of external forces, all suspended particles, regardless of their size, have the same translational kinetic energy. The average translational kinetic energy for any particle is equal to *1.5kT*, partitioned as *0.5kT* per degree of freedom, and therefore the velocity of a particle undergoing Brownian motion is given as [Probstein (2003)]:

$$\frac{1}{2} m {V_{avg}}^2 = \frac{3}{2} kT \tag{3.15a}$$

$$V_{avg} = \sqrt{\frac{3kT}{m}} \tag{3.15b}$$

Here, *m* is the mass of the particle, *T* is the temperature, and *k* is the Boltzmann constant. These thermally induced fluctuations cause a small particle in aqueous solution to vary in

direction many millions of times per second, and therefore in practical terms, only net displacement over a longer time scale can be observed [Probstein (2003)].

3.5 Surface Tension

High surface area to volume ratios are an inherent consequence of miniaturization. This characteristic drives the dominance of surface forces, reducing the influence of inertial and body forces [Pennathur et al. (2008)]. Surface tension arises when molecules located at an interface are more strongly attracted to one side of the interface. Curved interfaces will naturally arise due to tension at the surface. A surface in tension around a fluid will increase its pressure according to the Young-Laplace equation:

$$\Delta p = \gamma \left(\frac{1}{R_1} + \frac{1}{R_2} \right) \tag{3.16}$$

where γ is the surface tension coefficient and R_1 and R_2 are the radii of curvature of the inerface. This pressure difference can be leveraged to passively pump fluids [Juncker et al. (2002)], but can also cause undesired influence over pressure driven flow [Eftekhari et al. (2009)]. The influence of capillary forces is measured by the capillary number which indicates the ratio between viscous and surface tension forces:

$$Ca = \frac{\mu U}{\gamma} \tag{3.17}$$

where μ is the dynamic viscosity of the fluid and U is the characteristic velocity. Low capillary numbers are typical at micro- and nano-scale interfaces, indicating a dominance of surface-based forces. For instance, at 20ºC, the surface tension of pure water in contact with air is 73 mN/meter [Raicu and Popescu (2008)], and therefore, a water-air interface travelling at 1 mm/s in a channel with a circular cross-section of diameter 100 μm, has a capillary number on the order of 1×10^{-5}.

The Marangoni effect describes motion resulting from surface tension gradients along an interface. This effect has been exploited in microfluidics where surface tension

gradients have been created using localized heating via through optics or by joule heating in electrically resistive elements [Farahi et al. (2004), Farahi et al. (2005)].

3.6 Electrical double layer

Solid surfaces acquire a surface charge when in contact with a liquid electrolyte. There are four mechanisms by which this occurs including: (i) differences in the affinity of the two phases for electrons; (ii) differences in the affinity of the two phases for ions; (iii) physical entrapment of non-mobile charge in one phases, or most commonly (iv) surface charge is caused by the dissociation of surface groups and specific absorption of ions in the solution to the surface [Probstein (2003)]. This most common mechanism, the ionization of surface groups, is considered in this work. Depending on the number and type of acid and basic groups present in solution, the solid has either a positive or negative surface charge density. The surface charge density is described as [Probstein (2003)]:

$$\sigma_s = \frac{\sum_i q_i}{A} \tag{3.18}$$

where $q_i=z_ie$ is the net charge of ion i, z_i is the valency of ion i, e is the electron charge, and A is the surface area. At a specific pH value of the solution, the surface bears no net charge, which is about pH 2 for glass [Schoch et al (2008)].

As a result of the fixed charge at the solid interface, ions in the electrolyte of opposite charge, termed counter-ions, will accumulate near the electrode while ions of like charge, termed co-ions, are repelled. Evidently there is no charge neutrality within this screening region because the number of counter-ions will be large compared with the number of co-ions. This screening region, consisting of bound and mobile charges, is called the electrical double layer (EDL) [Probstein (2003)].

The model of the electrical double layer has evolved with time. The earliest model of the electrical double layer is typically attributed to Helmholtz and was treated as a simple capacitor based on a physical model in which a single layer of ions absorbed on the surface. Guoy and Chapman later made significant improvements by introducing a

diffuse model of the electrical double layer where the potential decreases exponentially away from the surface due to absorbed fixed counter-ions from the solution [Schoch et al (2008)]. The current representation of the electrical double layer is called the Gouy-Chapman-Stern model. Stern introduced a layer between the inner and outer Helmholtz planes, see Figure 3.3, in which the charge and potential distribution are assumed to be linear, and a diffuse layer further from the wall where the Guoy-Chapman theory is applied [Schoch et al (2008)].

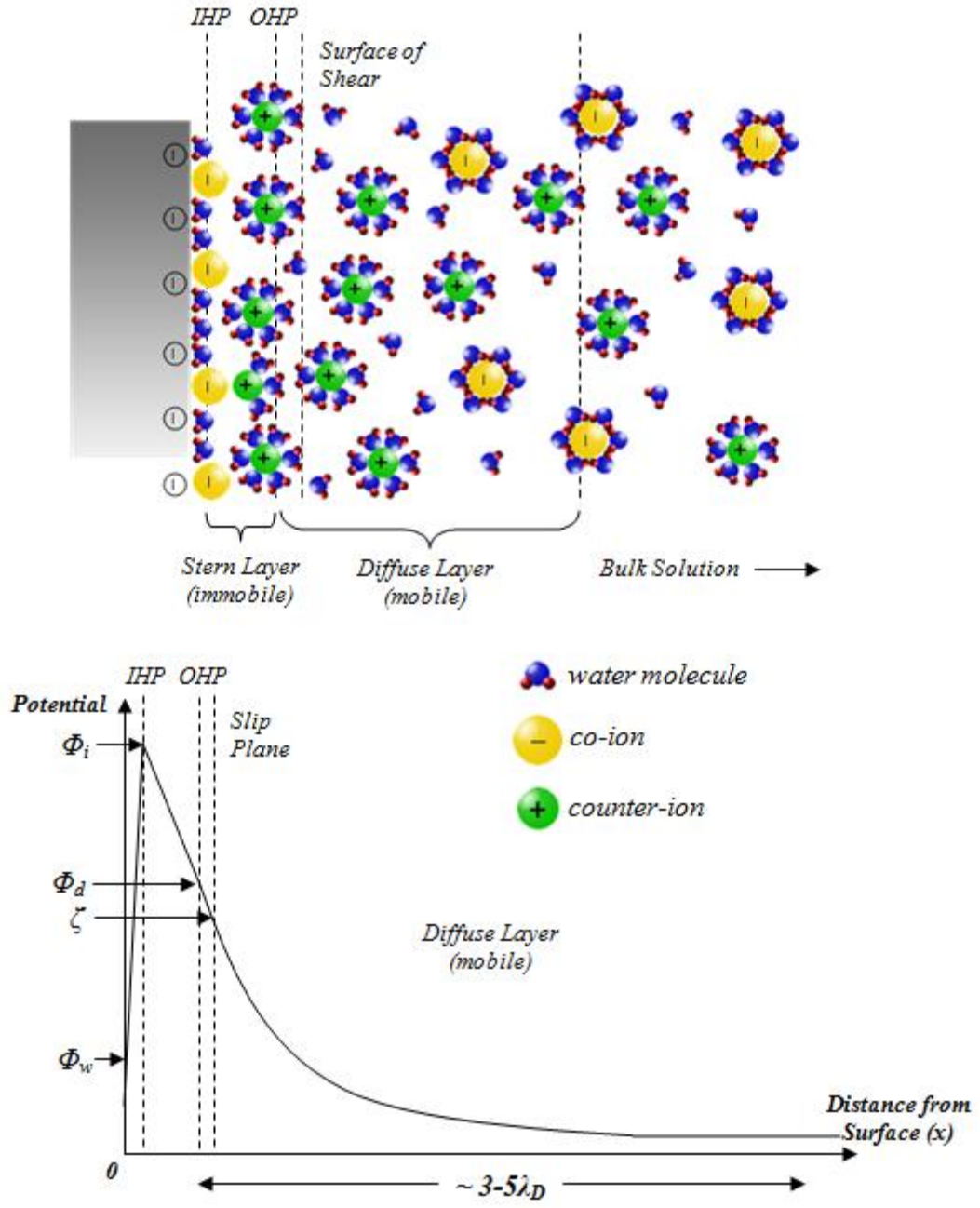

Figure 3.3: Gouy-Chapman-Stern model of the electrical double layer at the solid-liquid interface. The (a) distribution of ions and resulting (b) potential distribution are shown. Potentials are indicated at the wall, Φ_w, the inner Helmholtz plane, Φ_i, the outer Helmholtz plane, Φ_d, and the slip plane, ζ.

This model, shown in Figure 3.3, is divided into three layers. The first layer is at the inner Helmholtz plane and bears the potential Φ_i, where co-ions and counter ions are not hydrated and are specifically absorbed to the surface. The second layer is defined by the outer Helmholtz plane with potential Φ_d, consisting of a layer of bound, hydrated, and partially hydrated counter-ions. The outermost and third layer is the diffuse layer, composed of mobile co-ions and counter-ions, in which resides the slip plane bearing the ζ potential. In most cases, the outer Helmholtz plane and the slip plane are situated close to each other, allowing the approximation of Φ_d with the ζ potential for practical purposes [Schoch et al (2008)].

The distribution of charged species near a charged surface will be determined by the interplay between electro-migration, ordinary diffusion, and convection. For dilute solutions, the molar flux can be represented by the adding the electro-migration term to Fick's law:

$$j^* = \underbrace{-vzFc\nabla\varphi}_{\text{electro-migration}} - \underbrace{D\nabla \mathrm{c}}_{\substack{\text{ordinary}\\ \text{diffusion}}} + \underbrace{\mathrm{c}\vec{\mathrm{u}}}_{\text{convection}} \tag{3.19}$$

where j^* is the molar flux, v is the ion mobility, F is Faraday's constant, c is concentration and D is the diffusion coefficient. Diffusivity and ion mobility are directly related through the Nernst-Einstein equation:

$$D = RTv = kN_A Tv \tag{3.20}$$

where R is the universal gas constant, k is the Boltzman constant, N_A is Avogadro's number and T is temperature. Evaluating the charge distribution perpendicular to a flat surface, as is commonly seen in microchannels, the analysis simplifies to a single dimension. Substituting the relation between ion mobility and diffusivity and acknowledging the disappearance of net molar flux and convective terms at steady state, the balanced molar flux equation becomes:

$$\left[\frac{-ze}{kT}\right]\frac{\partial\varphi}{\partial x} = \frac{1}{c}\frac{\partial c}{\partial x} \tag{3.21}$$

Integrating over *x*, the direction perpendicular to the surface, and recognizing that charge potential goes to zero and ion concentration approaches bulk concentration as $x \rightarrow \infty$ the concentration of ions in the electrical double layer are then described by the Boltzmann distribution:

$$c(x) = c_0 exp\left[\left(\frac{-ze}{kT}\right)\varphi(x)\right] \tag{3.22}$$

Here, c_0 is the bulk concentration, *z* is the valence charge, *e* is the elementary charge, *k* is the Boltzman constant and Φ is the electrostatic potential. Notably, the concentration of ions decreases exponential away from the charged surface. For a medium of uniform dielectric constant, electric potential is relate to charge distribution by means of the Poisson's equation:

$$\nabla^2\varphi = -\frac{\rho_E}{\epsilon} = \frac{-F}{\epsilon}\sum z_i c_i \tag{3.23}$$

where ρ_E is the electric charge density and ϵ is the permittivity of the solution, and z_i and c_i are the valence and concentration of the i^{th} species respectively. The variation of electrostatic potential with distributed charge is determined by combining equations 3.21 and 3.22 to produce the Poisson-Boltzman equation:

$$\frac{d^2\varphi}{dx^2} = \frac{-F}{\epsilon}\sum_N z_i\left[c_{i0} exp\left(-\frac{z_i e}{kT}\varphi(x)\right)\right] \tag{3.24}$$

In the common case of a single symmetric electrolyte ($z=z_+=z_-$), the Poisson-Boltzmann equation becomes:

$$\frac{d^2\varphi}{dx^2} = \frac{2zF c_0}{\epsilon} sinh\left(\frac{zF}{RT}\varphi(x)\right) \tag{3.25}$$

The Poisson-Boltzmann equation can be solved analytically assuming that the surface potential is small everywhere ($z_i\Phi_i$ < 25.7mV at 25°C) and by expanding the exponential

(using the relation $e^{-\alpha} = 1-\alpha$ for small α), which results in the Debye-Hückel approximation:

$\frac{d^2\varphi}{dx^2} = \frac{\varphi(x)}{\lambda_D^2}$; where

$$\lambda_D = \sqrt{\frac{\epsilon RT}{2F^2 z^2 c}} \tag{3.26}$$

Integrating the Debye-Hückel approximation subject to the conditions: $\Phi=\Phi_w$ at $x=0$ and $\Phi=0$, $d\Phi/dx=0$ as $x\rightarrow\infty$ gives,

$$\phi = \phi_w exp\left(-\frac{x}{\lambda_D}\right) \tag{3.27}$$

At higher surface potentials, the Debye-Hückel approximation is no longer valid and the Poisson-Boltzmann equation must be solved explicitly. This is done analytically only under the assumption that the electrolyte is symmetrical where the valence of the co-ion is equal to the valence of the counter-ion. By twice integrating the Poisson-Boltzman equation we obtain the Gouy-Chapman equation [Rahaman (2003)]:

$$tanh\left(\frac{zF\phi(x)}{4RT}\right) = tanh\left(\frac{zF\phi_w}{4RT}\right) exp\left(\frac{-x}{\lambda_D}\right) \tag{3.28}$$

In the Guoy-Chapman model, presented in Figure 3.4a, surface charge is balanced by an influx of counter-ions and small reduction of co-ions. When the Debye-Hückel approximation is used instead, the two ion types are assumed to be of equal significance, as shown in Figure 3.4b [Schoch et al (2008)].

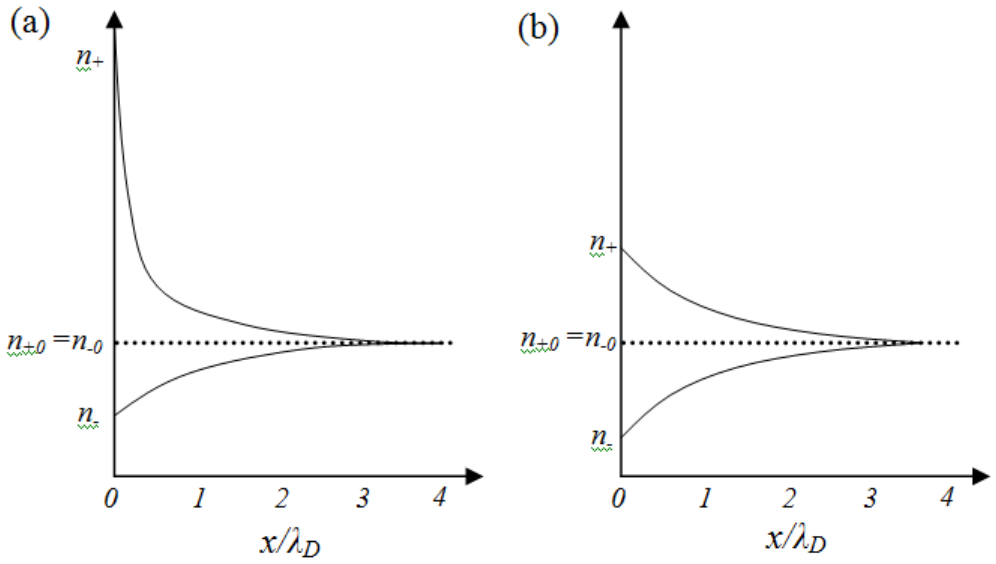

Figure 3.4: Volume densities of positive and negative ions near a negatively charged surface using the (a) Gouy-Chapman model with an excess of positively charged ion and (b) the Debye-Hückel approximation with a roughly symmetrical co-ion and counter-ion distribution.

At low surface potentials, the movement of counter-ions and co-ions cause significantly less disruption to overall volume densities; thus less error is incurred through the use of the Debye-Hückel approximation at low surface potentials than at higher potentials.

3.7 Surface Charge

For electro-neutrality, the surface charge density must be balanced by the charge density in the adjacent solution:

$$\sigma_w = -\int_0^\infty \rho_E dx \tag{3.29}$$

Substituting for ρ_E from the Poisson equation:

$$\sigma_w = \epsilon_0 \epsilon_r \int_0^\infty \nabla^2 \phi(x) dx = \left(\epsilon_0 \epsilon_r \frac{d\phi}{dx}\right)_0^\infty = -\epsilon_0 \epsilon_r \left(\frac{d\phi}{dx}\right)_{x=0} \quad (3.30)$$

Integration of the Poisson Boltzmann equation yields:

$$\left(\frac{d\phi}{dx}\right)_{x=0} = -\left(\frac{8RTc}{\epsilon_0 \epsilon_r}\right)^{1/2} sinh\left(\frac{zF\phi_w}{2RT}\right) \quad (3.31)$$

Combining the equation 3.29 and equation 3.30 yields:

$$\sigma_w = (8\epsilon_0 \epsilon_r RTc)^{1/2} sinh\left(\frac{zF\phi_w}{2RT}\right) \quad (3.32)$$

For low potentials, the Debye-Hückel approximation is valid and the equation becomes:

$$\sigma_w = \epsilon_0 \epsilon_r \frac{\phi_w}{\lambda_D} \quad (3.33)$$

3.8 Electrode-electrolyte interface

The electrode-electrolyte interface can be modeled by an equivalent electrical circuit. The interface between the electrode and the ionic solution can be represented by its capacitance, C_{EDL}, which is the capacitance sum of the Stern layer, C_S, and the diffuse (Gouy-Chapman) layer, C_D:

$$\frac{1}{C_{EDL}} = \frac{1}{C_S} + \frac{1}{C_D} \quad (3.34)$$

The stern layer can be modeled as a simple capacitor:

$$C_S = \frac{\epsilon_0 \epsilon_r A}{d_S} \quad (3.35)$$

where d_S is roughly the thickness of the stern layer. The stern layer thickness depends on the size of the ions and on the surface properties of the material, but is typically on the order of 0.2nm [Gupta et al. (2007)]. The Stern layer capacitance per unit area is typically on the order of 20μF/cm^2 [Timmer et al. (2002)]. The diffuse layer capacitance is obtained by differentiating the equation for surface charge with respect to surface potential:

$$C_D = \frac{d\sigma_w}{d\phi_w} = \frac{\epsilon_o \epsilon_r}{\lambda_D} cosh\left(\frac{zF\phi_w}{2RT}\right) \tag{3.36}$$

Once again at low potential, the Debye-Hückel approximation is valid and there the diffuse layer capacitance becomes:

$$C_D = \frac{\epsilon_o \epsilon_r}{\lambda_D} \tag{3.37}$$

Previous work has shown the Debye-Hückel approximation to be valid for wall potentials on the order of 26mV [Conlisk (2005)] and zeta potentials as high as 50 mV and 75 mV [Rice and Whitehead (1965), Hogg et al. (1966)]. At potentials higher than these, greater co-ion and counter-ion concentration differences are present and the Gouy-Chapman model is more appropriate. Outside of the electrical double layer, the bulk solution can be modelled simply as a resistor whose electrical properties are characterized by its conductivity.

3.9 Time-dependent Electrical Double Layer

The transient formation of the electrical double layer is also of interest, particularly where an alternating potential is applied to a solid-liquid interface. Researchers [Han et al. (2009)] have experimentally investigated the formation of the electrical double layer under an applied alternating square-wave voltage with peak to peak value of 1V and a rise time of less than 0.5μs. The discrete changes in potential across the EDL and electrolyte during the charging of the electrical double layer are shown in the schematic below.

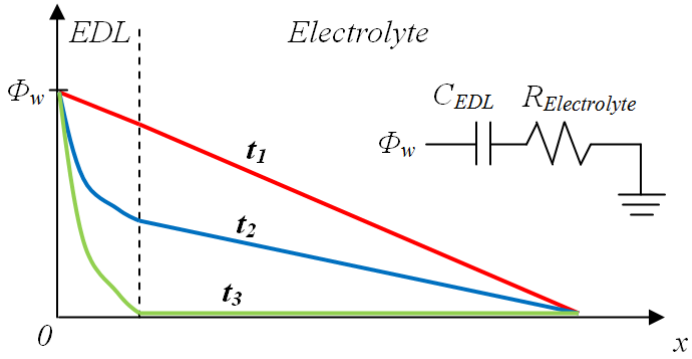

Figure 3.5: Schematic showing the potential distribution in the electrical double and electrolyte. Three times are shown corresponding to the instant a surface charge is applied (t_1), the transient EDL charging phase (t_2) and after the electrical double layer is fully charged (t_3). The corresponding equivalent electrical circuit is shown inset.

As previously stated, the electrical double layer and electrolyte can be modelled by an electrically equivalent capacitor and resistor in series. As such, the behaviour of the electrolyte and electrical double layer, during the onset of an applied surface potential at the solid-liquid interface, should be in accordance with well established RC circuit behaviour. The potential drop across the capacitive electrical double layer and resistive electrolyte as predicted by an electrically equivalent circuit is shown in figure 3.6.

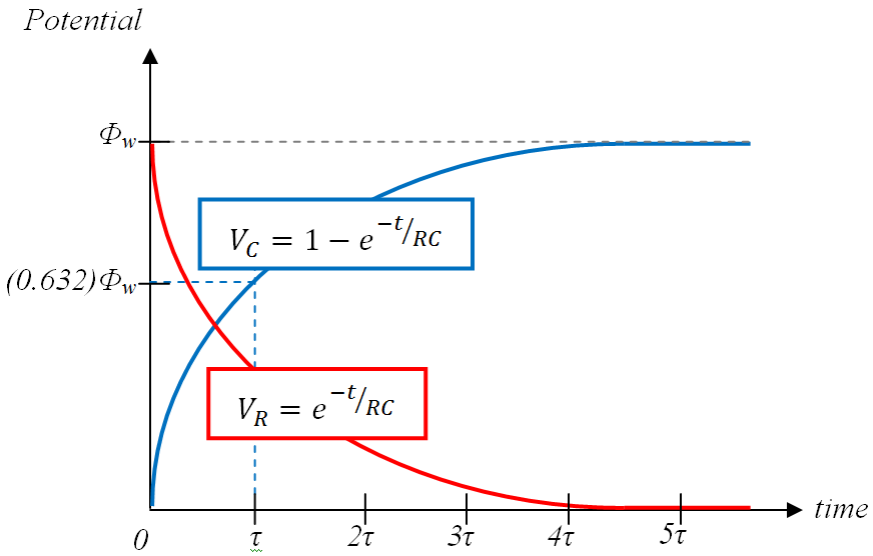

Figure 3.6: The behaviour of the electrical double layer and electrolyte during the onset of a surface charge as explained using an equivalent RC circuit.

In the case of an RC circuit and the electrical double layer in series with the solution resistance, the circuit time constant is given as:

$$\tau = RC \tag{3.38}$$

In the context of electrical RC circuits, the time constant is defined as the period of time over the voltage drop across the resistive element reduces to 36.8% of its peak value [Sedra and Smith (2004)].

Considering ionic solutions, when the electrolyte concentration increases, the decay time will be determined by two competitive processes. On one hand, C_{EDL} becomes larger for most electrodes at higher electrolyte concentration, as shown by previous researchers [Gao et al. (1993), Benavente et al. (1996)]. On the other hand, the resistance of the electrolyte reduces due to higher density of charge carriers. For systems that allow direct contact between electrode and electrolyte, little change in decay time results with changes in electrolyte concentration.

Previous work [Han et al. (2009)] has defined a charging time for the electrical double layer, $\tau_{10\%}$, representing the time required for the voltage drop across the bulk

electrolyte to decay to 10% of its peak value. They reported that for sodium chloride [NaCl] based electrolytes, the charging time for concentrations of 1mM and less is approximately 50 milliseconds [Han et al. (2009)]. Therefore, at applied frequencies higher than 10Hz, the electrical double layer will never fully form. Impedance based measurement using high excitation frequencies, therefore, may be able to probe the formation rate of the electrical double layer. In turn, impedance based measurements at high frequencies may show sensitivity to phenomena affecting ion transport during EDL formation, such as convective transport across electrodes.

3.10 EDL Interaction Force

In addition to the hydrodynamic implications of particles travelling in close proximity to a wall, EDL interaction will play a key role. In the following analysis, a sphere of radius *a* located at a distance *d* from a second sphere or from an infinite surface, as shown in Figure 3.7, is considered.

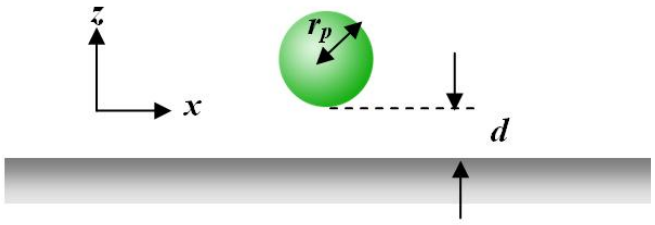

Figure 3.7: Illustration of a spherical particle at a distance, *d*, away from a planar wall.

Hogg et al. derived an analytical expression for the potential energy of interaction between two spherical particles, U_e, using Derjaguin's method, and arrived at the equation [Hogg et al. (1966)]:

$$U_e(d) = \frac{\pi \epsilon_r \epsilon_0 r_{p1} r_{p2} (\zeta_1^2 + \zeta_2^2)}{a_1 + a_2} \left[\frac{2\zeta_1 \zeta_2}{\zeta_1^2 + \zeta_2^2} ln\left(\frac{1 + exp(-d/\lambda_D)}{1 - exp(-d/\lambda_D)} \right) + ln\left(1 - exp\left(\frac{-2d}{\lambda_D} \right) \right) \right] \quad (3.39)$$

where r_{p1} and r_{p2} are the radii of the two spheres, ζ_1 and ζ_2 are the zeta potentials of the two spheres, and *d* is the distance between spheres. For the case of a sphere near a planar

wall, the EDL interaction potential can be obtained by setting r_{p1}=r$_p$, r_{p2}=∞, ζ_1=ζ_p, and ζ_2=ζ_w:

$$U_e(d) = \pi\epsilon_r\epsilon_0 r_p\left(\zeta_p^2 + \zeta_w^2\right)\left[\frac{2\zeta_p\zeta_w}{\zeta_p^2+\zeta_w^2} ln\left(\frac{1+exp\left(-d/\lambda_D\right)}{1-exp\left(-d/\lambda_D\right)}\right) + ln\left(1 - exp\left(\frac{-2d}{\lambda_D}\right)\right)\right] \qquad (3.40)$$

Accordingly, the EDL interaction force can be obtained by differentiating the potential energy equation with respect to *d*, the distance between the edge of the particle and the wall:

$$F_{EDL} = -\frac{\partial U_e}{\partial d} = \frac{2\pi\epsilon_r\epsilon_0 r_p}{\lambda_D}\left(\zeta_p^2 + \zeta_w^2\right)\left[\frac{2\zeta_p\zeta_w}{\zeta_p^2+\zeta_w^2}\left(\frac{exp\left(-d/\lambda_D\right)}{1-exp\left(-2d/\lambda_D\right)}\right) - \left(\frac{exp\left(-2d/\lambda_D\right)}{1-exp\left(-2d/\lambda_D\right)}\right)\right] \qquad (3.41)$$

When *d* is on the order of the Debye length, λ_D, the EDL interaction force is significant, but it decays very quickly for d greater than λ_D.

3.11 Dielectrophoresis

Dielectrophoresis (DEP) is a phenomenon in which motion of polarizable particles results from the application of non-uniform electric fields [Hughes (2002)]. The force depends on the induced dipole and the electric field gradient, not on the particle's charge as is the case with electrophoresis. As a result, dielectrophoresis has been used to precipitate DNA and proteins [Washizu and Kurosawa (1990)], to manipulate bacteria [Casanella et al. (2003)] and to manipulate and separate cells [Bennett et al. (2003)] as well as sub cellular components such as microtubules [Tsiper and Soos (2002)].

Dielectrophoresis was first reported by Herbert Pohl at Princeton University in 1958 [Pohl (1958)], but has recently re-emerged as a highly active research area in the context of microfluidic devices. The main features of dielectrophoresis (DEP) can be summarized as follows: (i) particles experience DEP force only when the applied electric field is non-uniform; (ii) the DEP force does not depend on the polarity of the applied electric field and is observed for AC as well as DC excitations; (iii) particles are attracted to regions of stronger electric field when undergoing positive DEP, and repelled from regions of stronger electric field when undergoing negative DEP; (iv) DEP is most readily observed for particles with diameters ranging from 1μm to 1000 μm.

Dielectrophoresis is best explained from the standpoint of fundamental electrostatic interactions. The development of fundamental dielectrophoresis theory shown here is a summary of two previous works [Ghallab and Badawy (2004), Jones (2003)]. A standard dipole with the separation distance of the charges defined by the magnitude of the vector *d* is shown in Figure 3.8. The vector *r* indicates the position of the dipole relative to the origin of the electric field, *E*. In this simple dipole model, the separation distance between dipoles, *d*, is infinitesimally small compared to that of *r* and the charges $+q$ and $-q$ are equal in magnitude.

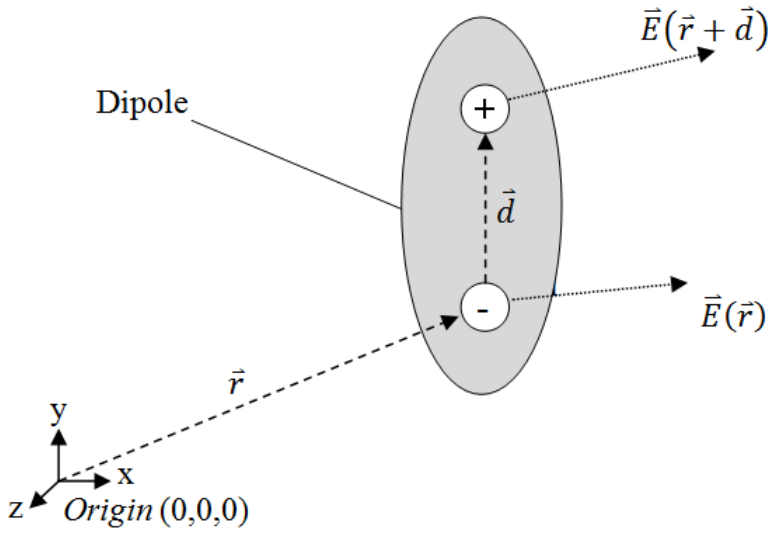

Figure 3.8: Representation of an elementary dipole in a non-uniform electric field.

Because the applied electric field strength, *E(r)*, is non-uniform, the two charges ($+q$ and $-q$) will experience different values of the vector field. The net force on the dipole is given as:

$$\vec{F} = \underbrace{q\vec{E}(\vec{r}+\vec{d})}_{\vec{F}_+} - \underbrace{q\vec{E}(\vec{r})}_{\vec{F}_-} \tag{3.42}$$

Using Taylor series expansion:

$$\vec{E}(\vec{r}+\vec{d}) = \vec{E}(\vec{r}) - \vec{d}\cdot\nabla\vec{E}(\vec{r}) + higher\ order\ terms \tag{3.43}$$

Because d is very small, we can neglect all higher order terms, which are simply multiplied by higher powers of d. Substitution into the net force equation yields:

$$\vec{F} = q\vec{d} \cdot \nabla\vec{E} = \vec{p} \cdot \nabla\vec{E} \tag{3.44}$$

where p is the dipole moment. The ideal electric dipole moment, p, is a measure of the polarity of a system of electric charges and is suitable for the case of infinitely small particles. For a small spherical neutral particle in a dielectric medium with permittivity ϵ_m, the effective dipole moment, p_{eff}, is derived from the electrostatic potential of a dipole:

$$\phi = \frac{\vec{p}_{eff} \cdot \vec{r}}{4\pi\epsilon_m r^3} \tag{3.45}$$

When the dipole is replaced by a small neutral sphere with radius a and permittivity of ϵ_p, the perturbed electric fields around the sphere either bend toward the sphere or away from it. For the case where both the sphere and surrounding medium are lossless dielectrics (ie. both materials have finite dielectric constant and zero conductivity), the new electrostatic potential has the form:

$$\phi = \frac{(\epsilon_p - \epsilon_m) \cdot r_p^3 \cdot \vec{E} \cdot \vec{r}}{(\epsilon_p + 2\epsilon_m) r^3} \tag{3.46}$$

The ideal dipole moment p can now be replaced with the sphere's effective dipole moment, p_{eff}:

$$\vec{p}_{eff} = 4\pi r_p^3 \epsilon_m \left(\frac{\epsilon_p - \epsilon_m}{\epsilon_p + 2\epsilon_m}\right) \vec{E} \tag{3.47}$$

The net force acting on a sphere with radius r_p located in a non-uniform electric field becomes:

$\vec{F} = \vec{p}_{eff} \cdot \nabla\vec{E}$; substitution yields

$$\vec{F} = 2\pi r_p^3 \epsilon_m \left(\frac{\epsilon_p - \epsilon_m}{\epsilon_p + 2\epsilon_m}\right) \nabla\left|\vec{E}\right|^2 \quad (3.48)$$

This equation serves as the idealized dielectrophoretic force equation in which both particle and medium act as perfect dielectric materials. In a more realistic case, conductivity of both particle and medium will influence polarization and this influence will vary with applied frequency. In this case, both the particle and medium have a complex permittivity of $(\epsilon_p)^*$ and $(\epsilon_m)^*$ respectively. When exposed to a spatially non-uniform AC electric field, the time averaged DEP force, F_{DEP}, is defined as:

$$\vec{F}_{DEP} = 2\pi r_p^3 \epsilon_m Re[K(\omega)] \nabla E_{rms}^2 \quad (3.49)$$

where

$$K(\omega) = \left(\frac{\epsilon_p^* - \epsilon_m^*}{\epsilon_p^* + 2\epsilon_m^*}\right) \quad (3.50)$$

Here, $K(\omega)$ is the complex Clausius-Mossotti factor, and the complex permittivity of the particle and medium are defined as follows:

$$\epsilon_p^* = \epsilon_p - j\frac{\sigma_p}{\omega} \quad (3.51a)$$

and

$$\epsilon_m^* = \epsilon_m - j\frac{\sigma_m}{\omega} \quad (3.51b)$$

where σ_p and σ_m are the conductivity of the particle and the medium, respectively, and ω is the angular frequency of the applied field. The real part of the Clausius-Mossotti factor, that determines the direction of the dielectrophoretic force, can be expanded by substituting for the complex permittivity values:

$$Re[K(\omega)] = \frac{\epsilon_p - \epsilon_m}{\epsilon_p + 2\epsilon_m} + \frac{3(\epsilon_m \sigma_p - \epsilon_p \sigma_m)}{\tau_{MW}(\sigma_p + 2\sigma_m)^2(1+\omega^2\tau_{MW}^2)}; \text{ where}$$

$$\tau_{MW} = \frac{\epsilon_p - \epsilon_m}{\epsilon_p + 2\epsilon_m} \tag{3.52}$$

is the Maxwell-Wagner charge relaxation time. The low and high frequency limits for *Re[K(ω)]* will be identified as:

$$Re[K(\omega)] = \frac{\sigma_p - \sigma_m}{\sigma_p + 2\sigma_m}, \quad \text{for } \omega \rightarrow 0 \tag{3.53}$$

$$Re[K(\omega)] = \frac{\epsilon_p - \epsilon_m}{\epsilon_p + 2\epsilon_m}, \quad \text{for } \omega >> 0 \tag{3.54}$$

At low frequencies, conductivity dictates the value of *Re[K(ω)]* while permittivity dominates at high frequencies. In general, dielectrophoresis can be applied to conducting or insulating particles with different outcomes. If a particle has a higher conductivity and lower permittivity than the surrounding medium, as in the case of a gold particle suspended in an aqueous solution, it will undergo positive dielectrophoresis at low frequencies and negative dielectrophoresis at high frequencies. Conversely, if the particle has a lower conductivity and higher permittivity than the surrounding medium, as in the case of a latex sphere suspended in a conducting aqueous solution, it will undergo negative dielectrophoresis at low frequencies and positive dielectrophoresis at high frequencies. These simple cases are summarized the figure 3.9 below.

As previously discussed, when a solid particle is brought into contact with a liquid, an electrical double layer will typically form. The surface conductance created by the electrical double layer, will affect particles under low frequency electric fields where

conductance influences dielectrophoretic force. In both dielectrophoretic configurations, there exists a cross-over frequency, ω_c, at which no dielectrophoretic force acts on a particle ($Re[K(\omega)]=0$). The cross-over frequency also acts as a point of transition where the direction of the dielectrophoretic force changes. This cross-over frequency can be calculated as follows:

$$\omega_c = \sqrt{\frac{(\sigma_m - \sigma_p)(\sigma_p + 2\sigma_m)}{(\epsilon_p - \epsilon_m)(\epsilon_p + 2\epsilon_m)}} \tag{3.55}$$

If a particle were to exhibit a conductivity and permittivity that were both either higher or lower than the surrounding medium, then no crossover frequency would exist, and that particle would experience positive or negative dielectrophoresis, respectively, across all frequency ranges.

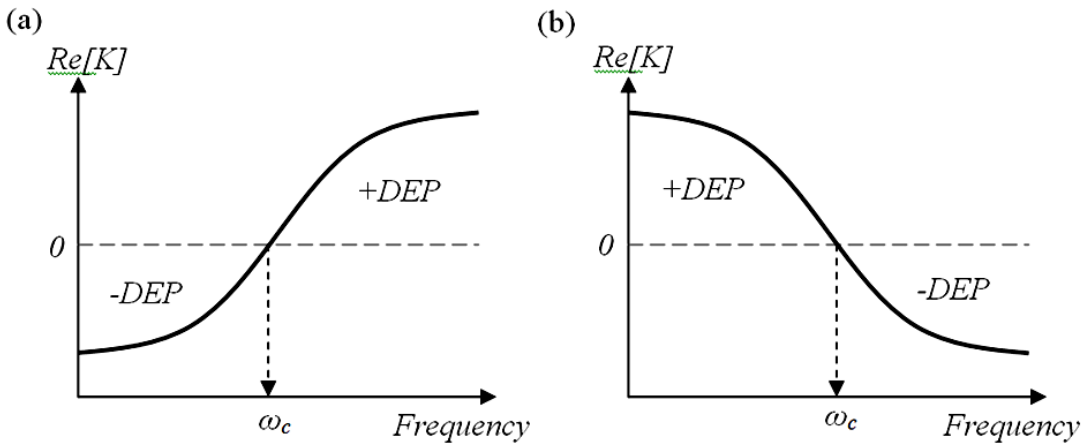

Figure 3.9: Dielectrophoretic spectra for (a) $\sigma_p<\sigma_m$ and $\epsilon_p>\epsilon_m$ and (b) $\sigma_p>\sigma_m$ and $\epsilon_p<\epsilon_m$.

The real part of the Clausius-Mossotti factor will vary between values of -0.5 to 1.0 for perfect dielectric particles and perfectly conducting particles respectively. The imaginary part of the Clausius-Mossotti factor is considered in the case of traveling-wave dielectrophoresis or electro-rotation [Lei et al. (2009), Falokun and Markz (2007)]. These phenomena require the application of multiphase excitation signals and therefore are not discussed in this work. Furthermore, the use of spherical particles throughout this

work negates particle orientation effects; particle rotation is only of interest when rotation based forces arise or where particle displacement results. For further explanation of traveling-wave dielectrophoresis and electro-rotation, comprehensive review articles on dielectrophoresis are available [Cummings and Khusid (2007), Hughes (2002), Jones (2003)].

3.12 Influence of Surface Conductance on Particle Behaviour

For spherical particles in an electrolyte of given ionic strength, the volume of the electrical double layer varies with the square of the particle radius while the volume of the particle varies with the cube of its radius. As a result, the influence of the electrical double layer becomes more pronounced as the size of the particle is reduced. Previous work [Hughes and Green (2002)] has demonstrated that the effective conductivity of a particle can be described as the sum of three components: the native conductivity of the particle, σ_{native}, and the conductance of the diffuse double layer, K_d, and the Stern layer, K_S. The total conductivity is then written as:

$$\kappa_p = \kappa_{native} + \frac{2K_s + 2K_d}{r} \tag{3.56}$$

Here, r is the radius of the particle. For latex spheres, the bulk conductivity is negligible and the effective conductivity of the particle is dominated by surface conductance. The conductance of the diffuse layer can be expressed as [Lyklema (1991)]:

$$K_d = \frac{\left(4F^2 cz^2 D\lambda_D (1+3m/z^2)\right)}{RT}\left(cosh\left[\frac{zF\zeta}{2RT}\right] - 1\right) = \sigma_d \mu_d \tag{3.57}$$

where D is the diffusion coefficient, z is the valency of the counter-ion, F the Faraday constant, R the molar gas constant, T the temperature, λ_D is the Debye length, σ_d is the diffuse ion counter charge due to an excess of ions outside the slip plane, μ_d is the mobility of these ions in the diffuse part of the double layer, and m is a dimensionless parameter describing the electro-osmotic contribution to K_d given as:

$$m = \left(\frac{RT}{F}\right)^2 \frac{2\epsilon_m}{3\mu D} \tag{3.58}$$

where μ_s and μ_m are the mobilities of the ion species in the Stern layer and the bulk medium, respectively. The conductivity of the immobile Stern layer is given more simply as [Lyklema (1991)]:

$$K_s = \frac{\sigma_s \mu_s \kappa_m}{2zFc\,\mu_m} \tag{3.59}$$

Here, μ_s and μ_m are the mobilities of the ion species in the Stern layer and the bulk medium, respectively, whereas σ_s is the charge density of the Stern layer and κ_m is the bulk conductivity of the medium. If the electrolyte is symmetrical, it is possible to replace the conductivity term and concentration with molar conductivity, Λ:

$$K_s = \frac{\sigma_s \mu_s \Lambda}{2zF\mu_m} \tag{3.60}$$

When the values of the mobilities of the co-ions and counter-ions are equal the equation for Stern layer conductance simplifies to:

$$K_s = \sigma_s \mu_s \tag{3.61}$$

At low frequencies, surface conductivity plays a pivotal role in the dielectrophoretic behaviour of particles. Surface conductivity will influence the cross-over frequency exhibited by particles in solution, as well as the direction and magnitude of dielectrophoretic force, causing particles to deviate from expected behaviour where surface conductivity is not taken into account.

4.0 Continuous Dielectrophoretic Particle Focusing Using a Planar Electrode Arrangement

4.1 Introduction

The manipulation of particles or cells within a microchannel flow is central to many microfluidic applications. In the context of diagnostics that utilize antibodies in serum, for example, the removal of cells from the sample is required. Continuous removal of particles and cells is particularly critical in the case of flow-through nanohole array based sensing, as these serve as fine filters and thus are very susceptible to clogging.

More generally, particle/cell manipulation and sorting methods have been developed under the heading of cytometry. Cytometry is a process that measures the physical and/or chemical characteristics of cells or other biologically relevant particles. It typically consists of both particle/cell manipulation and detection elements. Most commercially available flow cytometers are expensive, bench-top laboratory instruments dedicated to a specific set of experiments or tests. Microfluidics-based flow cytometers offer reduced size and cost, creating opportunities for portability and disposability in addition to requiring smaller sample volumes [Chung and Kim (2007)].

In the context of cytometry, particles are detected and analyzed using methods that require the systematic positioning of particles. These include optical methods, such as scattering and/or fluorescence, and electrical methods using either direct current, as in the case of the Coulter counter, or alternating current for impedance analysis [Holmes et al. (2006)]. Traditionally, focusing is accomplished using additional fluid streams in sheath flow configurations that necessitate sample dilution [Mao et al. (2008), Pamme et al. (2003), Lin and Lee (2003)]. Such schemes are well developed, having been used in combination with planar structures and minimal additional fluid streams to create three-dimensional sheath flow [Howell et al. (2008)]. Other works have demonstrated undiluted particle focusing based on obstacle arrays constructed from polydimethylsiloxane (PDMS) [Choi and Park (2008)], standing surface acoustic waves [Shi et al. (2008)] and dielectrophoresis [Yu et al. (2005)].

While charge-based particle manipulations are well developed, dielectrophoresis offers opportunities for manipulation of electrically neutral particles. In the context of microfluidic devices, the ease of fabrication and electric field non-uniformities associated with planar electrode designs make them well suited for dielectrophoresis applications. Dielectric focusing has been achieved using insulating structures to create non-uniform electric fields for dielectric focusing or separation [Cummings and Khusid (2007)]. Recent work demonstrated three-dimensional focusing of particles using positive dielectrophoresis in combination with a dielectric structure placed between two electrodes parallel to the flow to achieve three-dimensional focusing [Chu et al. (2009)]. The dielectric structure was created by polymerizing a wall of photoresist along the length of the channel between patterned electrodes. SU-8 based insulators have been used to focus cells in a similar two-step photolithography process that yields an array of electrodes and insulators orthogonal to the direction of flow [Demierre et al. (2008)].

Non-uniform electric fields inherent with planar electrode configurations, however, are sufficient to achieve dielectrophoresis without integration of insulators to create field non-uniformities. Previous dielectrophoresis based works of this type have demonstrated sorting and trapping of idealized dielectric particles using planar electrodes [Gascoyne and Vykoukal (2002), Hughes (2002), Choi and Park (2005), Kralj et al. (2006), Wang et al. (2006)], but have yet to demonstrate simple, single step photolithography based dielectrophoretic focusing schemes; particularly with the use of relatively unrefined biological samples. In this work, chevron shaped, interdigitated electrodes are used to produce dielectrophoretic forces in combination with hydrodynamic drag to displace particles from their corresponding streamlines to the center of a microchannel. Fabrication is accomplished using single step lithography and all alignment is performed by hand with the aid of a 2X magnification microscope. A schematic of the device and corresponding particle motion is shown in Figure 4.1.

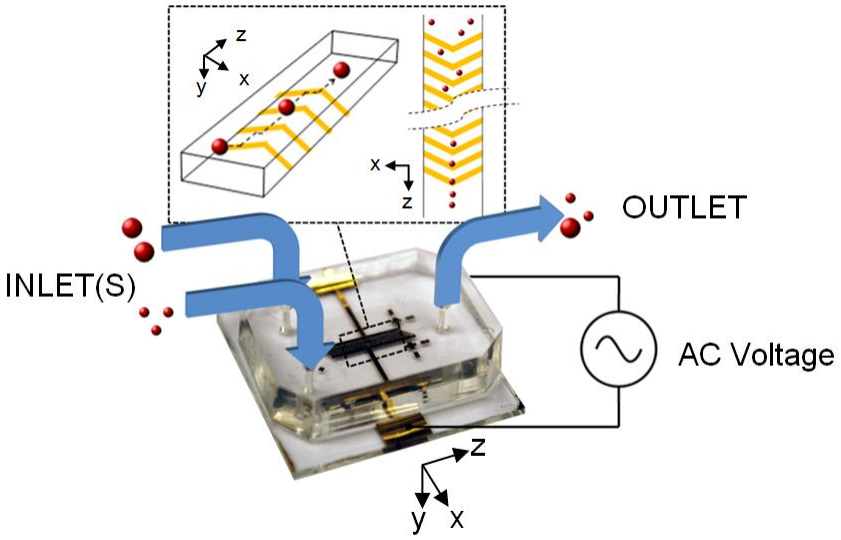

Figure 4.1: Microfluidic chip with interdigitated, 45º chevron-shaped electrode array and corresponding particle motion inset. The microfluidic channel used to transport particles over the interdigitated array measures 600 µm in width and 30 µm in height.

Analytical and finite element modeling are used to provide insight into the focusing mechanism. Furthermore, an extension of this work to the direct dielectrophoretic manipulation of cells in whole blood is discussed.

In the focusing scheme discussed herein, particles are pushed to the top of the microchannel ensuring that particles pass through the anticipated detection region in single file, negating the possibility of superimposed particles evading detection. While particles or cells coming in contact with the channel wall can lead to fouling, thus interfering with optical or electrochemical measurements, suitable surface treatments to reduce fouling are available [Yao et al. (2004), McClain et al. (2001), Tung et al. (2004), Dittrich and Schwille (2003), Li and Harrison (1997)].

4.2 Experimental Preparation

4.2.1 Microchip Fabrication and Assembly

All microfluidic assemblies were prepared using in-house fabrication techniques. A complete microchip was assembled using an upper and a lower substrate of PDMS and gold patterned glass respectively.

The base substrates were gold coated microscope slides, purchased from EMF-Corp (Ithaca, NY), on which electrodes were patterned. The gold coated slides were first immersed in acetone and sonicated for 3 minutes, rinsed in isopropanol and air dried. A thin layer of negative photoresist (SU-8 10; Microchem, Newton, MA) was spin-coated (Specialty Coating Systems, Indianapolis, IN) onto the substrate with ramping at 3,000 rpm/30 seconds. The substrate was baked on covered contact hot plates at 65°C for 5 minutes and 95°C for 10 minutes. A photomask that defines the desired electrode pattern was generated in CAD software and printed by a high-resolution image setter on a transparency (Island Graphics, Victoria, BC). The substrate, placed under the photomask, was then exposed to collimated ultra-violet (UV) light (Tamarack Scientific, Corona, CA) for 60 seconds to ensure adequate polymerization of SU-8 for subsequent steps. The substrate was then baked at 65°C for 5 minutes and 95°C for 10 minutes. The substrate was allowed to cool, then immersed in SU-8 developer liquid (Microchem) to dissolve the unexposed portions of the photoresist. After developing, the substrate was rinsed with isopropanol and air dried. Ethanol was added to the substrate to induce wetting between small cross-linked SU-8 features for the subsequent etching steps. Gold etchant (Transene Company, Danvers, MA) was carefully added to the substrate using an eye dropper to preserve the desired pattern and avoid excessive lateral gold etching under the SU-8 mask. The substrate was then rinsed with isopropanol and air dried. Chromium etchant (Sigma Aldrich, St. Louis, MO) was also applied using an eye dropper, following a pre-wetting step with ethanol, to remove the chromium adhesion layer. Substrates were then rinsed in isopropanol and air dried. With etching complete, the substrate was then immersed in Remover PG (Microchem) to dissolve the cross linked SU-8 mask. The completed bottom substrate contained an interdigitated array of chevron shaped electrodes oriented at 45º with an electrode width and spacing of 70 μm and 40 μm respectively.

The top substrate was fabricated by replica moulding in poly(dimethylsiloxane) (PDMS; Dow Corning, Midland, MI), following established soft-lithographic protocols [Duffy et al. (1998)]. The specific equipment and procedure employed is detailed elsewhere [Coleman et al. (2006)]. Holes for inlet and outlet tubing were punched in the PDMS prior to assembly. Both PDMS and glass surfaces were plasma-treated (Harrick

Scientific, Pleasantville, NY) for 30 seconds to yield silanol surface groups that covalently bind glass to PDMS to render hydrophilic channel walls. The PDMS channel, measuring 600 μm in width and 30 μm in height, was aligned on top of the interdigitated electrode array leaving the external gold contacts exposed. Lastly, external wires were attached to the gold contacts using silver conductive epoxy (MG Chemical, Toronto, Canada).

4.2.2 Sample Preparation and Visualization

Fluorescent polystyrene microspheres (Duke Scientific, Fremont, CA) measuring 9.9 μm, 5.0 μm and 3.0 μm were diluted in salt solution prepared using de-ionized water and sodium chloride crystals (NaCl; ACP Chemicals, Montreal, Quebec) to achieve 50 mS/cm conductivity. Solutions were loaded into 1mL disposable syringes (Becton-Dickenson, Franklin Lakes, NJ) and delivered to the microfluidic chip using pressure induced by syringe pumps (PHD 2000, Harvard Apparatus, Hollison, MA) via Teflon tubing (1/16 in. diameter, S.P.E. Limited, North York, ON). Digital images were captured using a Regita 1300i CCD camera (QImaging, Surrey, BC) in combination with a Leica DM LM microscope (Leica Microsystems Inc., Richmond Hill, ON). An Agilent 33220A waveform generator (Agilent, Santa Clara, CA) delivered voltage to the device at an amplitude of $10V_{pk\cdot pk}$ and a frequency of 1 MHz. Use of high frequencies helped to prevent electrolysis, joule heating and double layer effects allowing surface conductance to be neglected [Gascoyne and Vykoukal (2005)]. Porcine whole blood treated with anti-coagulant K3 EDTA (Innovative Research, Novi, MI) was diluted in a 50:1 ratio in phosphate buffered saline (PBS). Sucrose was added to balance osmotic pressure. The sample was then delivered to the microfluidic chip using the same procedure employed for the polystyrene microsphere solution. The microfluidic chip was rinsed with surfactant, placed in a sonicator (Fisher Scientific, Hampton, NH) for 5 minutes, and rinsed with de-ionized water between uses.

4.3 Theoretical Analysis

4.3.1 Hydrodynamic Drag

An analytical and finite element model was developed to provide insight into the focusing mechanism. The model describes the influence of hydrodynamic and dielectrophoretic forces that dictate the paths traversed by particles.

The equation for viscous drag is appropriate for low Reynolds number flows such as those encountered in microchannels. In this case, the hydrodynamic drag force is linearly proportional to particle velocity and is referred to as Stokesian drag. For particles traveling in an infinitely quiescent fluid, with zero fluid slip at the particle surface, the Stokes' drag force is given by:

$$F_{DRAG} = 6\pi\mu r_p V \tag{4.1}$$

where r_p is the radius of the particle and V is the velocity of the particle relative to the viscous fluid. In the context of this work, particle-wall interactions are probable and must be taken into account. For the case of particles in shear flow, travelling close to an infinite no-slip surface, Faxen's Law [Happel and Brenner (1973)] gives the following relation for drag force:

$$F_{DRAG} = \frac{6\pi\mu r_p}{\beta} V; \text{ with}$$

$$\beta = \left[\frac{1-0.6526\left(\frac{r_p}{h}\right)+0.4003\left(\frac{r_p}{h}\right)^3-0.297\left(\frac{r_p}{h}\right)^4}{(3/2)}\right] \tag{4.2}$$

where h is the distance between the center of the particle and the wall. If the sphere is free to rotate, it will do so with an angular velocity in the same direction as if it were rolling along the wall [Happel and Brenner (1973)]. The angular velocity of the particle in shearing flow between two parallel plates is given by the shear rate [White (2003)]:

$$\omega = \alpha = \frac{\partial V_z}{\partial y} \tag{4.3}$$

In the absence of all other external forces, the fluid flow simply advects the sphere at a velocity matching the velocity field along the center of the particle.

Due to the large aspect ratio (~20:1) of the microchannel, a two dimensional Poiseuille flow approximation is valid everywhere outside of the region within about one channel height of the side walls [Deen (1998)]. Thus a simplified expression for average velocity can be derived from the Navier-Stokes equations:

$$V_{avg} = \frac{\Delta P}{2\mu}\left(-\frac{2}{3}L^2\right) = \frac{Q}{A} \tag{4.4}$$

Spatial variations in velocity are, nevertheless, significant in the vertical direction. Specific velocities pertaining to different particle sizes will be addressed in the following section.

4.3.2 Dielectrophoresis

Dielectrophoresis (DEP), as discussed in detail in section 3.11, is a phenomenon in which motion of polarizable particles results from the application of non-uniform electric fields [Hughes (2002)]. In micro- and nanoscale regimes, body forces induced by electric fields are highly predictable and controllable due to the viscous nature of low Reynolds number flows. Under such conditions, dielectrophoresis is a powerful and versatile tool; particularly when the forces resulting from the dielectric properties of a particle and its surrounding medium in a non-uniform electric field are frequency dependent. The dielectric force vector is defined as [Gascoyne and Vykoukal (2005)]:

$$F_{DEP} = 2\pi r_p^3 \varepsilon_0 \varepsilon_m Re[K(\omega)]\nabla E_{rms}^2; \text{ with}$$

$$K(\omega) = \frac{\varepsilon_p^* - \varepsilon_m^*}{\varepsilon_p^* + 2\varepsilon_m^*} \quad \text{and} \quad \varepsilon^* = \varepsilon - i\frac{\sigma}{\omega} \tag{4.5}$$

Here, the direction of the dielectrophoretic force is given by the sign of the real part of the Clausius Mossotti factor, Re[$K(\omega)$], which varies between values -0.5 and 1.0, loosely corresponding to insulating and conducting particles respectively.

The relative polarizability of particles and their surrounding medium are frequency dependent, and thus particles can experience both negative DEP (repulsive) or positive DEP (attractive) within a given experimental configuration, simply by adjusting the applied frequency. The frequencies at which particles transition between positive and negative dielectrophoresis are referred to as cross-over frequencies. The polarizability of particles is typically influenced by their surface conductivity, however, this only becomes significant at frequencies considerably less than 1 MHz [Duerr et al. (2003)] and thus will not be considered here.

4.4 Results and Discussion

4.4.1 Modeling

In this work, pressure-driven flow is used to transport particles across an interdigitated array of electrodes where they experience negative dielectrophoresis (nDEP), as shown schematically in figure 4.2. Displacement of particles from their corresponding streamlines is driven by the gradient in an applied electric field, $\nabla|E^2|$. To accurately determine the motion of particles, the E-field was determined using finite element modeling (FEM) software Comsol Multiphysics. An electrode width and spacing of 70 μm and 40 μm respectively, was used for both modeling and experiments. Salt solution with conductivity of 50mS/cm was used in modeling for comparison against experimental results.

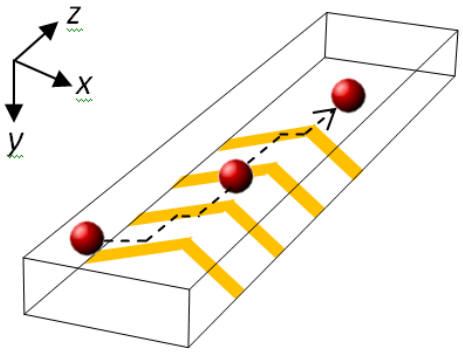

Figure 4.2: Schematic of particle displacement in a microchannel containing an array of interdigitated, chevron shaped electrodes. An electrode width and height or 70 µm and 40 µm respectively, was used for both modeling and experiments.

In the special case of interdigitated electrodes with equal width and spacing, the square of the E-field can be approximated by a sinusoidal function [Kralj et al. (2006)]. Micro fabrication constraints, however, often necessitate the use of smaller electrode spacing and larger electrode widths to maximize electric field gradients. For the general case of unconstrained electrode spacing and width, the magnitude of the square of the electric field gradient is assumed to be constant, which shows close fit with the numerical solution shown in Figure 4.4c:

$$|\nabla E^2| = \frac{(E^2)_{max}}{(w+s)/2} \tag{4.6}$$

where *w* and *s* are the width and spacing of electrodes respectively. The magnitude of y-component of the E-field squared, was determined upstream and downstream from the lagging edge of the electrode; the E-field is highest at electrode edges. The y-component of the E-field is plotted against distance from the electrode surface in Figure 4.3.

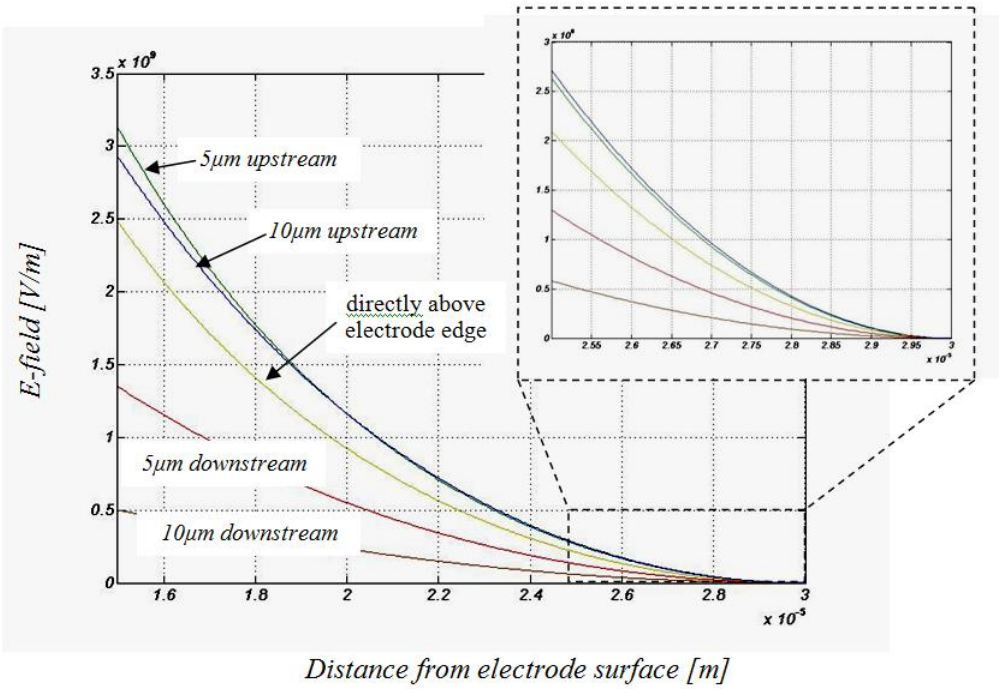

Figure 4.3: Magnitude of E-field in y-direction plotted against distance away from the surface of electrodes (starting from y = 30μm).

Particles are quickly repelled from the electrode edges, where high electric field gradients exist, to regions of lower electric field gradients at the top of the microchannel, as shown in Figures 4.4a and 4.4b. The height of particles in the microchannel is determined by balancing the buoyancy-corrected particle weight with dielectrophoretic repulsion toward the top of the microchannel. Direct particle-wall contact is prohibited by repulsive electrical double layer forces at close range; typically tens to hundreds of nanometers. The buoyancy-corrected particle weight is given by:

$$F_{BG} = \frac{4}{3}\pi r_p^3 g\left(\rho_p - \rho_f\right) \tag{4.7}$$

where g is the acceleration due to gravity, ρ_p is the density of the particle and ρ_f is the density of the medium. The buoyancy-corrected weight of particles is measured as fractions of pico-Newtons and thus was neglected in relation to dielectrophoretic forces for the particles used in this work. Both dielectrophoretic force and particle weight vary with particle size cubed, and thus they remain in equal proportion for all particle sizes, all

other conditions being held constant. The electrical double layer repulsion between a particle and the upper PDMS wall was found to be significantly higher than the vertical component of DEP force for separation distances on the order of several Debye lengths. As a result, particles will travel unimpeded at a fixed height close the top of the microchannel (ie. within a few Debye lengths ~200nm). With the particle height fixed, the analysis was simplified to two-dimensions over the periodic structure of the electrodes. The electric field strength along a plane 5μm from the top of the microchannel, shown in Figure 4.4c, is used to evaluate the dielectric force exerted on particles in the microchannel. Particles settle at roughly one particle radius from the top of the microchannel and thus 5μm was selected to accommodate the largest particles. Particles velocities were determined by evaluating the velocity field one particle radius from the top of the microchannel for all particle sizes studied respectively. Given the direction of flow and rotation, lift forces resulting from shear induced particle rotation would act to push particles to the bottom of the microchannel. An expression for lift force acting on a rotating sphere was derived by higher-order approximations and is given by Saffman's expression [Saffman (1965)]:

$$F_L = 6.46 v \rho r_p^2 U(|\alpha|/v)^{1/2} - \frac{11}{8}\rho U \alpha r_p^3 + \pi \rho U \omega r_p^3 \qquad (4.8)$$

Here, v is the kinematic viscosity, ρ is the density of the fluid, r_p is the radius of the particle, α is the shear rate, U is the fluid velocity on the stream line through the centre of the sphere and ω is the rotational angular speed of the sphere. The rotational angular speed is determined by equation 4.3. Assuming a linear velocity gradient across the diameter of the particle, the lift force was found to be on the order of femto-Newtons. The vertical component of dielectrophoretic force is several orders of magnitude higher, as measured in tens to hundreds of pico-Newtons, and thus these forces created through particle rotation were neglected.

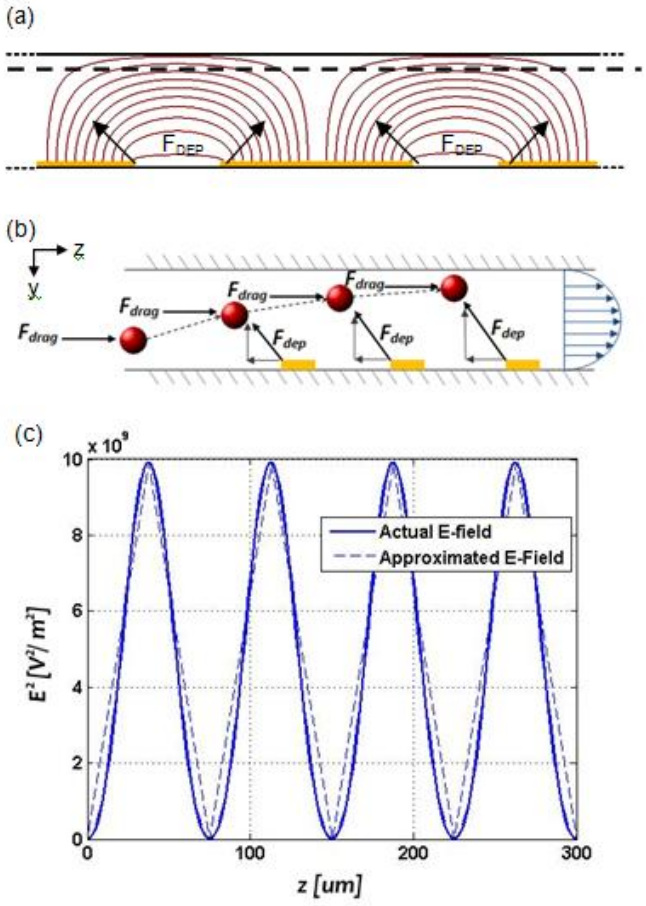

Figure 4.4: Schematic of (a) electric field lines distribution in microchannel with particle height indicated by a dashed line (5µm from top of the 30µm channel), (b) forces and corresponding path traversed by particles and numerical results of (c) electric field strength resulting from 10Vpp applied voltage in the plane indicated by the dashed line.

This velocity can be expressed both in absolute terms and relative to average velocity as follows:

$$V_0 = \frac{\Delta P}{2\mu}\left(r_p^2 - 2Lr_p\right) = \frac{r_p^2 - 2Lr_p}{-(2/3)L^2} V_{avg} \tag{4.9}$$

While the sphere will undergo rotation while traveling close to a wall, the particle velocity will be matched by the velocity of the fluid aligned with the center of the particle.

Hydrodynamic and dielectrophoretic forces combine to displace particles from their streamlines to the center of the microchannel. The controlled and predictable nature of flow inside microchannels makes it possible to predict, with high accuracy, the impact of hydrodynamic and dielectrophoretic forces. As shown in Figure 4.5, dielectrophoretic force is exerted on a particle in both the stream-wise and transverse directions. The dielectric particles used in this work are repelled from electrode edges where electric field gradients are highest. Stream-wise hydrodynamic and dielectrophoretic force components will be subtractive as particles approach regions of high electric fields and additive as particles depart from regions of high electric field. As a result, particles will oscillate between high and low stream-wise velocities when travelling over the interdigitated electrode array. Due to the angled nature of the electrode array, transverse dielectrophoretic forces will act to further the imbalance of particle residence time upstream and downstream of high electric field gradients respectively. Transverse particle motion will therefore be strongly biased in one direction, in this case, resulting in a net particle displacement toward the center of the microchannel.

The particle velocity induced by dielectrophoretic force, can be determined by balancing DEP and drag forces:

$$F_{DEP} = F_{DRAG} \tag{4.10}$$

Substituting equations 4.2 and 4.5 yields:

$$\frac{6\pi\mu r_p}{\beta} V = 2\pi r_p^3 \varepsilon_0 \varepsilon_m Re[K(\omega)] \nabla E_{rms}^2 \tag{4.11}$$

Formulations for velocity in the transverse and stream wise directions, respectively, are then given as follows:

$$V_x = \frac{2\pi r_p^3 \varepsilon_0 \varepsilon_m Re[K(\omega)] \nabla E_x^2}{6\pi\mu r_p} \beta \tag{4.12a}$$

$$V_z = \frac{2\pi r_p^3 \varepsilon_0 \varepsilon_p Re[K(\omega)] \nabla E_z^2}{6\pi\mu r_p} \beta + V_0 \quad (4.12b)$$

The net transverse displacement of particles is determined by taking the difference between transverse displacement of particles upstream and downstream of each electrode. When a particle approaches a high electric field gradient, the corresponding transverse displacement is approximated here as follows:

$$x_A = V_x t_A = \frac{2\pi r_p^3 \varepsilon_0 \varepsilon_m Re[K(\omega)] |\nabla E_x^2|}{6\pi\mu r_p} \beta \cdot t_A; \text{ with}$$

$$t_A = \frac{((w+s)/2) + x_A \tan\theta}{V_0 - V_z} \quad (4.13a)$$

Similarly, when a particle departs from a region of high electric field gradient, the corresponding transverse displacement is approximated here as follows:

$$x_D = V_x t_D = \frac{2\pi r_p^3 \varepsilon_0 \varepsilon_m Re[K(\omega)] |\nabla E_x^2|}{6\pi\mu r_p} \beta \cdot t_D; \text{ with}$$

$$t_D = \frac{((w+s)/2) - x_D \tan\theta}{V_0 + V_z} \quad (4.13b)$$

The total transverse displacement over the length of the microchannel is given by the product of the net displacement per electrode and the total number of electrodes, N, in the interdigitated array:

$$x_T = (x_A - x_D)N \quad (4.14)$$

Figure 4.5 illustrates the force vectors and resulting particle displacement. Electrodes are orientated at 45 degrees to maximize the net transverse displacement over the length of the microchannel.

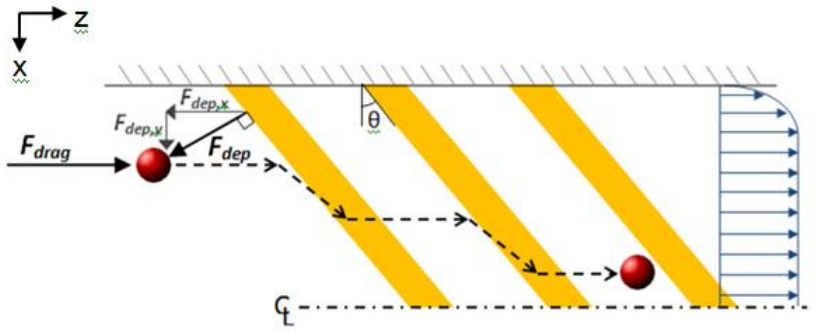

Figure 4.5: Schematic of particle displacement travelling over interdigitated electrodes. Electrodes were orientation at 45° in both modeling and experiments.

The model describing the relationship between hydrodynamic and dielectrophoretic forces can be used to predict the viability of the focusing mechanisms under a variety of conditions. The influence of flow rate and particle size is revealed by the model in Figure 4.6.

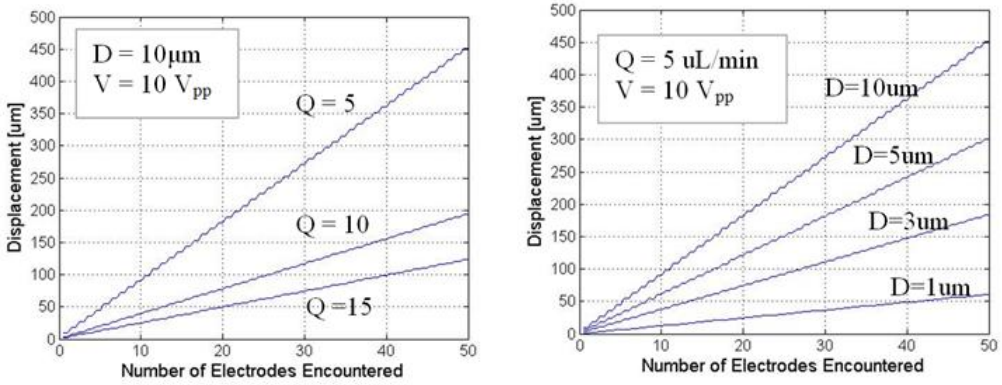

Figure 4.6: Predicted particle displacements for an applied voltage of 10Vpk-pk given (a) varying flow rates and (b) particle sizes (bottom).

4.4.2 Consideration of Unsteady Conditions

The oscillatory nature of forces imparted on particles as they travel over an interdigitated electrode array necessitates consideration of unsteady effects. The forcing and viscous diffusion time scales can be compared to evaluate the interplay between vorticity generation and dissipation. The forcing time scale and viscous diffusion time scale are taken as follows:

$$t_{forcing} = \frac{(w+s)/2}{V_z}; \text{ and} \quad (4.15)$$

$$t_{vd} = \frac{h^2}{v} \quad (4.16)$$

Here, *w* and *s* are the electrode width and spacing respectively, V_z is the axial velocity, *h* is the distance between the center of the sphere and the wall and *v* is kinematic viscosity. The value of *h* is taken for the largest particle diameter employed (10μm) and the value of V_z is taken as the average flow rate for the highest flow rate employed (15 μL/min) to study the conditions most susceptible to influence from unsteady effects. The kinematic viscosity of water ($1x10^{-6}$ m^2/s) was also used. Using these parameters, the forcing time scale was found to be more than 2 orders greater than the viscous diffusion time suggesting that it is reasonable to neglect unsteady behaviour.

Furthermore, steady state is attained more rapidly in the presence of a wall than without it. For the case of impulsive motion of a sphere close to a planar wall, the relation between applied force and the rate at which steady state is approached is given as [Happel and Brenner (1973)]:

$$\frac{F}{6\pi\mu r_p V_z} = 1 + \frac{9}{16}\frac{r_p}{h} + \frac{1}{2}\frac{r_p h^2}{\sqrt{\pi}(\sqrt{vt})^3} \quad (4.17)$$

where *F* is the applied force, and *v* is kinematic viscosity, *t* is steady state development time, and *h* is the distance between the center of the particle and the wall. The applied force will be that induced by dielectrophoresis in the axial direction. The time required to reach steady state is almost instantaneous, on the order of picoseconds. At flow rates of 15μL/min, the direction of dielectrophoretic force changes less than every 6 milliseconds and therefore it is probably reasonable to assume that unsteady influences are negligible.

4.4.3 Experimental Results

Focusing was performed experimentally using 9.9 μm, 5.0 μm and 3.0 μm spherical polystyrene beads. The relative position of 9.9 μm at the inlet and outlet of the focusing channel are shown in Figure 4.7. Particles were transported at a flow rate of 5 μL/min across fifty interdigitated chevron-shaped electrodes powered by a $10V_{pk\text{-}pk}$ excitation voltage operating at 1 MHz. Flow rate thresholds for complete focusing over the length of the channel (300 μm displacement in 50 electrodes or less) were not in disagreement with model predictions, however, further experimentation is required to validate the model.

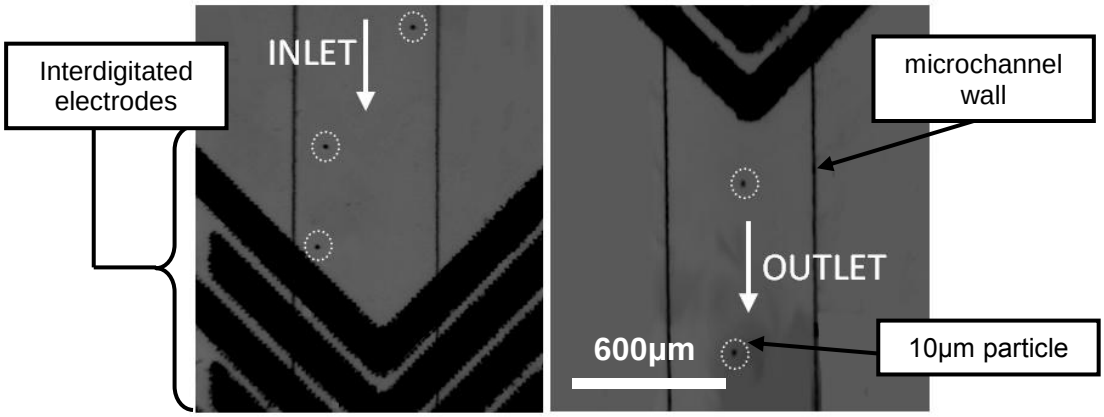

Figure 4.7: Microscope images of 9.9 μm polystyrene spheres entering (left) and existing (right) the interdigitated electrode array with electrode with of 70 μm and electrode spacing of 40 μm.

The focusing device was also used in conjunction with diluted porcine whole blood treated with anti-coagulant K3 EDTA. Transverse displacement of ~6 μm red blood cells was observed only at flow rates an order of magnitude lower than that predicted for equivalent sized polystyrene microspheres. Visualization was also greatly hindered by an absence of fluorescent staining and nonspecific adhesion to microchannel walls.

The composition of the red blood cells adopts that of the supporting medium and thus the relative permittivity between particle (cell) and medium will inherently yield much smaller dielectrophoretic forces and must be mitigated by using lower flow rates, or higher applied voltages. The problem of nonspecific cell to channel adhesion can be addressed using previously cited surface treatments to prevent biofouling. Specifically,

coating of the microfluidic channels with Bovine serum albumin (BSA) is expected to prevent much of the nonspecific adhesion of red blood cells to channel walls. Furthermore, use of stained blood cells would aid cell visualization and indicate the utility of this focusing device with biological cells.

4.5 Summary

In this paper, a sheathless particle focusing scheme was demonstrated using dielectrophoresis in combination with a simple planar, chevron-shaped, interdigitated electrode arrangement. The focusing mechanism used a combination of hydrodynamic and dielectrophoretic forces to displace particles from their corresponding streamlines to the center of a microchannel. Analytical and numerical modeling was used to quantify the performance of this device. Experiments conducted using 9.9 μm, 5.0 μm and 3.0 μm polystyrene microspheres are found to be in agreement with the developed model. Focusing of red blood cells suspended in diluted whole blood was also shown to be viable using this device.

5.0 Dielectrophoresis for Tuneable Transport in Flow-Through Nanohole Arrays

5.1 Introduction

The mechanism behind macro-scale filtration is straight forward; solid entities larger than the nominal pore size of a filter are prevented from passing, while solvent and smaller particles pass readily through the pores. On the nanoscale, however, molecules and ions are often prohibited from entering pores which are physically much larger because of electrostatic interactions [Bhattacharjee et al. (2001), Szymezyk et al. (2005)]. The commonly adopted techniques for retaining particles in this manner leverage repulsive intermolecular and colloidal forces, such as electrostatic and hydration forces between particle and the pore walls [Kang et al. (2001), Wang et al. (1995), Childress and Elimelech (2000), Ma et al. (2000)]. These forces act selectively on particles, hindering their entry into, and transport through, the pores compared to the solvent. Nevertheless, the ranges of these forces are extremely small and are typically dictated by chemistry of the membrane, the particles, and the solvent [Molla and Bhattacharjee (2008)].

Dielectrophoresis (DEP) offers opportunities for particle manipulation, in the context of filtration media, where forces are based on dipole interactions rather than are particle charge or surface chemistry. Toward this goal, dielectrophoresis was recently used to control the sedimentation of micro-particles through micro-porous media [Molla and Bhattacharjee (2008)]. Extensions of this phenomena to particles on the order of 100nm and 200nm and media with pore sizes on the order of 300nm is of interest in this work, motivated by several research challenges: (i) dielectrophoretic force quickly decays with reductions in particle size rendering many conventional DEP devices ineffective at this scale; (ii) current micro- and nano-scale fabrication methods are highly amiable to coplanar electrode configurations and as a result, dielectrophoresis is much less explored with three dimensional geometries fabricated by other means; (iii) surface-based sensors benefit both from the increased surface area offered by porous media and active attraction or repulsive of analyte from sensing surfaces.

Metallic nanohole arrays support surface electromagnetic waves that enable enhanced optical transmission [Sinton et al. (2008), Gordon et al. (2008)], as shown in Figure 5.1b. The optical transmission is dependent on the refractive index immediately above the metallic surface, which is altered by surface adsorption, and thus may be exploited for sensing. To date, most nanohole arrays used in optical sensing have been employed in flow-over configurations [De Leebeeck et al. (2007), Im et al. (2009)], similar to conventional surface patterned sensors. Three dimensional nanohole structures operated in a flow-through format, however, offer additional benefits. The rapid diffusion characteristics of nanofluidics enables much improved transport of reactants to the in-hole surface which has been shown to dominate with respect to sensing [Ferreira et al. (2009)]. In addition the flow-through nanohole array serves as a sieve and thus has the potential for improved limits of detection over previous surface based sensing methods. As a result, flow-through nanohole arrays, as shown in Figure 5.1a, exhibit increased sensitivity and reduced analysis time compared to their flow-over counterparts [Eftekhari et al. (2009)].

Active enhancement of micro and nano-scale transport using dielectrophoresis is hoped to further the utility of the flow-through configuration. In addition to transporting molecular analytes to the in-hole surface, flow-through nanohole arrays may also be used in conjunction with nanoparticles in a variety of foreseeable formats. The geometry of nanohole arrays in gold films enables the generation of highly localized non-uniform electric fields (potentially enabling dielectrophoresis) and creates physical boundaries to restrict Brownian motion to a single degree of freedom: partially alleviating dielectrophoresis scaling issues. The potential for combined dielectrophoresis and flow-through plasmonic sensing encompasses three areas of particular interest: the dielectrophoretic trapping/collection of dielectric particles in nanoholes for analyte collection; the ability to remove particles/contaminants from the nanoholes; the collection of metal nanoparticles in nanoholes that can take advantage of the enhanced in-hole electromagnetic field for surface enhanced Raman spectroscopy (SERS) [Hu et al. (2009)]. In this preliminary work, the viability of dielectrophoresis tuned nano-particle transport in a nanohole array is investigated through analytical and numerical modeling. The effects of hydrodynamic drag and Brownian motion are considered in the context of

applied voltage, flow rate and particle size. Preliminary flow-through tests are performed experimentally as proof of concept. The motive for this work is driven by the potential for localization of biomarkers on the surface of particles to improve figures of merit in optical sensing such as detection limits, sensitivity and selectivity. Extensions towards the use of gold nanoparticles would permit for the use of surface enhanced raman scattering (SERS) to achieve these improved figures of merit.

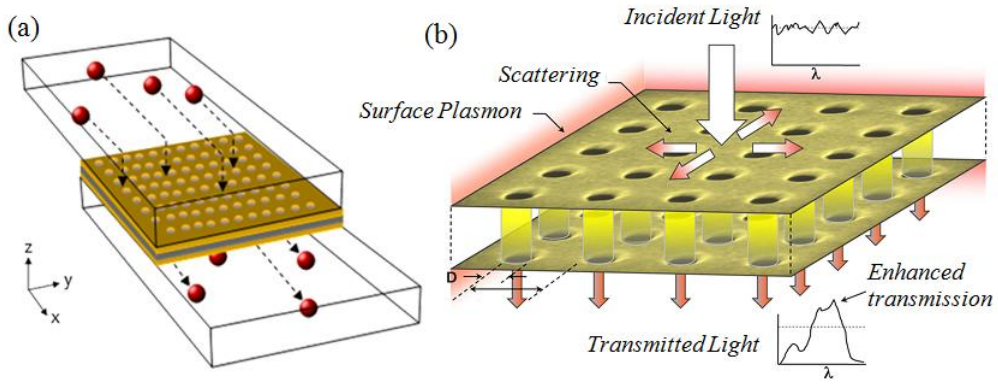

Figure 5.1: (a) Particles flow through an array of nanoholes at the junction of two microfluidic channels. (b) A conceptual diagram illustrating incident light scattering into surface plasmon modes and enhanced transmission at selected wavelengths.

5.2 Theory

Relevant nanoscale phenomena are introduced including: dielectrophoresis in nanoholes, hydrodynamic drag, and Brownian motion.

5.2.1 Dielectrophoresis in Nanoholes

Dielectrophoresis is a phenomenon in which motion of polarizable particles results from the application of non-uniform electric fields [Hughes (2002)]. Traditionally, these non-uniform electric fields have been created using insulating objects to disrupt electric field lines [Lapizco-Encinas (2004), Lapizco-Encinas (2005)] or using planar electrode arrangements [Molla and Bhattacharjee (2007), Cui et al. (2001)], as shown in Figure 5.2a. Extension of the planar electrode arrangement to an axis-symmetric format, as shown in Figure 5.2b, generates highly localized non-uniform

electric fields that can create stronger field gradients achieving higher dielectrophoretic forces.

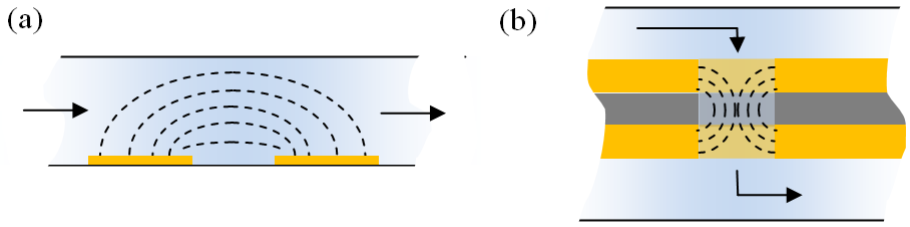

Figure 5.2: Non-uniform electric fields can be created using (a) a traditional planar electrode arrangement or using (b) an axis-symmetric electrode arrangement that offers enhanced electric field localization.

In this work, two axis-symmetric electrode configurations were designed to maximize electric field strength, and electric field gradients, while remaining viable with respect to nanohole-based sensing and available manufacturing methods. The first configuration, shown in Figure 5.3a, is comprised of two 100nm thick gold layers separated by a 100nm layer of silicon nitride (Si_3Ni_4); arrays of nano-sized holes penetrate through all three layers allowing passage of fluid through the membrane. Silicon nitride is a hard ceramic having high strength, moderately high elastic modulus and unusually high fracture toughness [Carter and Norton (2007)]. This combination of properties permits very thin layers of silicon nitride (~25-100nm) to withstand structural loading from pressures typical of microfluidic devices [Tong et al. (2004)].

The size of the nanoholes is largely dictated by the optical effects employed in sensing. Specifically, hole sizes larger than the wavelength of incident light generally allow too much direct light transmission for surface based sensing. Likewise, the relevant particle sizes must be less than the hole size. With these aspects in mind a 300 nm diameter hole size was selected. The electric field strength, for an applied AC voltage of 400mV, is shown in Figure 5.3b for the first membrane configuration with a schematic of the electric field line distribution inset. All numerical work was carried out using finite element modeling software Comsol Multiphysics with post processing carried out using Matlab. In all cases, a grid independence study was performed on structured

meshes to ensure solution convergence. It should be noted that this first electrode configuration acts as a very large parallel plate capacitor, where the capacitance is given as:

$$C = \frac{\epsilon_s \epsilon_0 A_S}{d} \tag{5.1}$$

Here, ϵ_s and ϵ_0 are the relative permittivity of silicon nitride and permittivity of a vacuum respectively, A_S is the surface area of the gold layers, and d is the separation between them; in this case d is 100 nm. When a voltage is applied, movement of charge between the upper and lower electrode can take place through the conductive solution or through direct capacitive coupling across the silicon nitride layer separating electrodes. Large conductance makes electron transport through the silicon nitride a more feasible path for electrons. Operation at high frequency further reduces the impedance offered by direct capacitive coupling, and thus it will be difficult to generate electric fields in the conductive solution using intermediate to high applied frequencies. As a result, this configuration must operate at low frequencies and therefore must also operate at lower applied voltage to avoid potentially disruptive electrolysis or faradaic reactions.

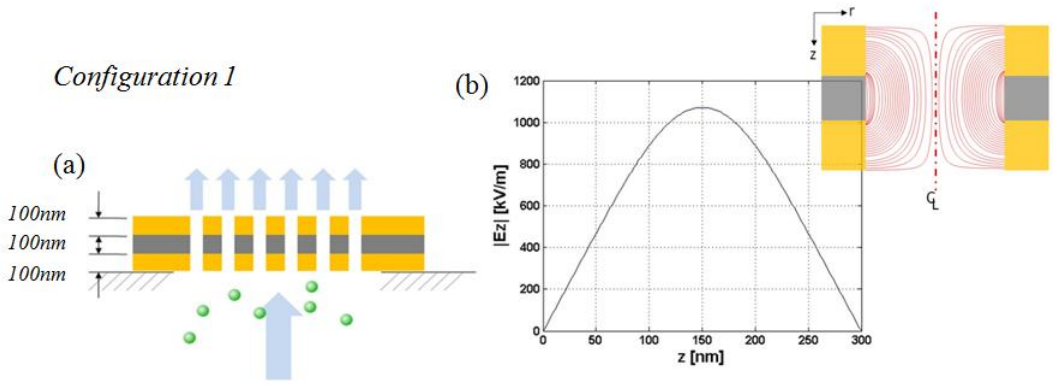

Figure 5.3: (a) The first configuration is comprised of two 100nm thick gold layers separated by 100nm of silicon nitride (Si3Ni4). (b) The electric field strength, as calculated along the center axis of the nanohole, for an applied AC voltage of 400mV is shown with a plot of the electric field line distribution inset.

In the second electrode configuration, shown in figure 5.4a, two 100nm layers of gold are separated by a 100nm layer of silicon nitride (Si_3Ni_4) and a gap of 300 microns

where working solution resides during operation. Similarly, arrays of nano-sized holes penetrate through both layers allowing fluid flow across the membrane. The additional electrode spacing avoids the capacitive coupling issues of the first configuration. Higher applied frequencies are therefore permitted, allowing greater operating voltages without the onset of electrolysis or faradaic reactions. Despite the additional electrode spacing, high electric field gradients are preserved. The electric field strength and distribution are shown in Figure 5.4b.

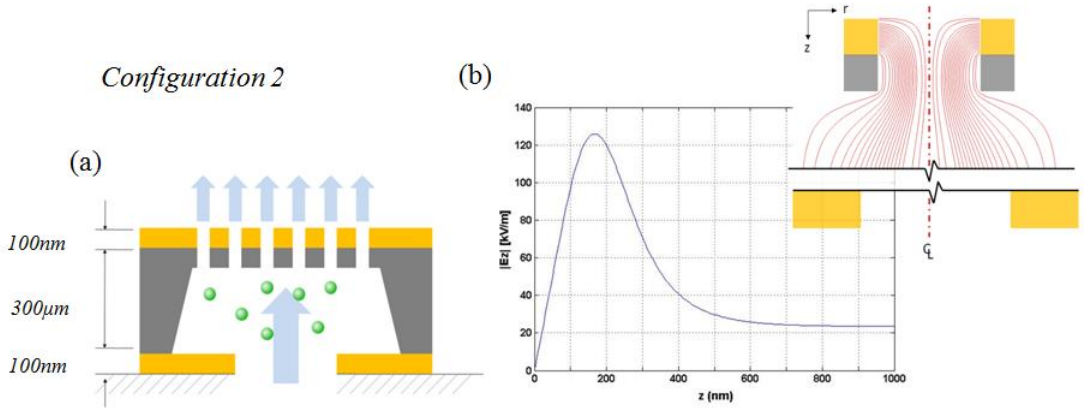

Figure 5.4: Schematic of (a) the second configuration comprising two 100nm thick gold layers separated by 100nm of silicon nitride (Si3Ni4) in addition to a 300μm gap where working fluid resides during operation. (b) The electric field strength, measured along the center axis of the nanohole, for an applied AC voltage of 10V is shown with a plot of the electric field line distribution inset.

The dielectric force acting on particles is highly dependent on particle size, as well as electric field strength gradients and the Clausius-Mossotti factor [Hughes (2002)]:

$F_{DEP} = 2\pi\epsilon_m\epsilon_0 r_p^3 Re[(\omega)]\nabla|E_{rms}^2|$; with

$$K(\omega) = \frac{\epsilon_p^* - \epsilon_m^*}{\epsilon_p^* + 2\epsilon_m^*} \tag{5.2}$$

The Clausius-Mossotti factor dictates the direction of dielectrophoretic force varying between -0.5 and 1.0 for strongly repulsive and attractive DEP respectively, as shown in

Figure 5.5. Repulsive, or negative, DEP in the context of nanohole arrays is well suited for separation of channel constituents, pre-concentration of analyte or, potentially, removal of contaminants from the sensor.

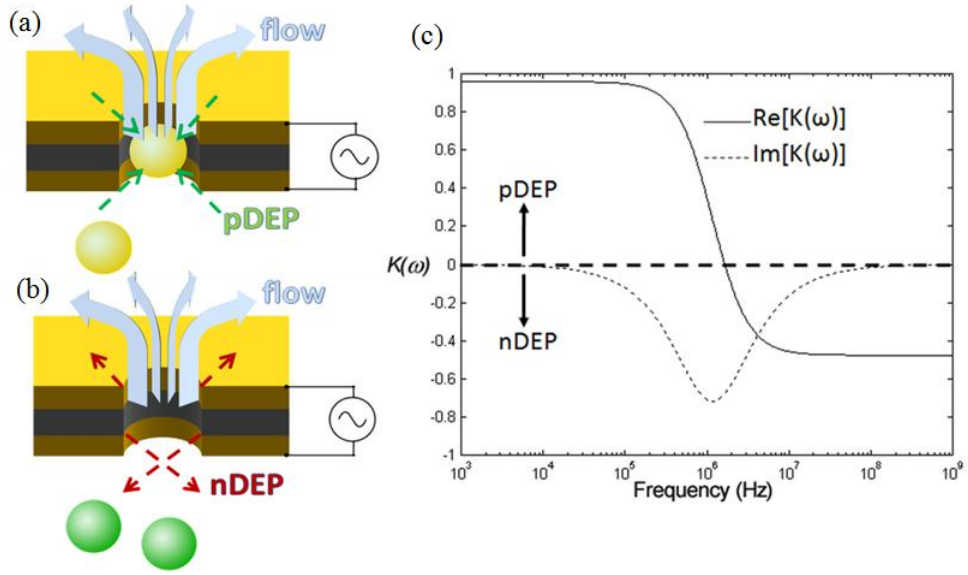

Figure 5.5: Application of a non-uniform electric field creates tuneable transport through nanohole arrays using both (a) negative dielectrophoresis and (b) positive dielectrophoresis as shown. (c) The direction of the dielectric force is determined by the sign of the Clausius-Mossotti factor, *K(w)*, as shown by the schematic.

Dielectrophoretic particle manipulations become more complex as surface conductance is taken into account. For a given ionic strength, the volume of the double layer increases with the square of the particle radius while the volume of the particle increases with the cube of its radius [Gascoyne and Vykoukal (2002)]. Thus these double layer effects become particularly prominent at the nanoscale. The total conductivity of a particle can be expressed as the sum of bulk conductivity and that arising from the electric double layer [Hughes et al. (1999)]:

$$\sigma_p = \sigma_{native} + \frac{2K_S + 2K_d}{r_p} \tag{5.3}$$

where σ_{native} is the native conductance of the particle, r is the particle radius, and K_s and K_d are the Stern and diffuse layer contributions to surface conductance respectively.

While this will have a minimal effect with highly conductive particles, such as gold nano-particles, surface conductance will affect the behaviour of dielectric particles, such as latex nano-spheres, at lower frequencies where the influence of conductivity on dielectrophoretic force is more prominent. That being said, all modelled dielectrophoretic interactions are taken here to be perfectly repulsive or attractive in order to benchmark the attainable performance of both proposed configurations. Little error is incurred by this assumption when high frequencies are used minimizing the influence of surface conductance.

5.2.2 Hydrodynamic Drag on Nano-particles

Hydrodynamic drag is exerted on a particle where the velocity of a particle differs from that of the surrounding fluid. In the context of nanohole arrays, there are two situations where this arises: when particles are prevented from entering a nanohole and when particle are trapped inside a nanohole. Particles prevented from entering a nanohole will be repelled from high electric field gradients by negative dielectrophoresis and remain situation in the relatively unbounded fluid. In this case, assuming a spherical particle, the viscous drag on a sphere can be expressed using the Stokes' drag formula (see equation 3.8). Drag force scales linearly with particle size and therefore, at a critical particle size, we can expect the hydrodynamic drag force to overwhelm the dielectrophoretic force prohibiting the passage of particles through the nanohole array.

Similarly, particles located inside nanoholes are attracted to the region of high electric field by positive dielectrophoresis. In this case, fluid flowing past the particle is confined by the walls of the nanohole, and therefore a correction factor, for a sphere moving trapped against Poiseuille flow, must be applied to the Stokes' drag formula. The correction factor applied here is that of [Haberman and Sayre (1958)]:

$F_{drag} = 6\pi\mu r_p(VK)$; where

$$K = \frac{1-(2/3)\left(r_p/R_0\right)^2-0.20217\left(r_p/R_0\right)^5}{1-2.1050\left(r_p/R_0\right)+2.0865\left(r_p/R_0\right)^3-1.7068\left(r_p/R_0\right)^5+0.72603\left(r_p/R_0\right)^6} \quad (5.4)$$

Here, R_0 is the radius of the nanohole and V is the approach velocity of the fluid. As quantified by the correction factor ($K>1$), stationary particles confined inside a nanohole will experience more drag from passing fluid than those located outside the nanohole. For this reason positive DEP forces used to hold particles within nanoholes will have to be greater than negative DEP forces used to hinder transport through nanohole arrays.

5.2.3 Brownian Motion

Dielectrophoretic manipulation of nanoparticles has been demonstrated [Zhang et al. (2009), Green and Morgan (1997)], but is often hindered by Brownian diffusion unless electrode arrays are of similar proportions to particles; thus generating significant field strength and electric field inhomogeneity [Duerr et al. (2003)]. Carbon nanotubes, for example, have been used as electrodes to overcome Brownian motion in particles as small as 2 nm [Zheng et al. (2004)]. DEP force is proportional to the cube of particle radius and is thus less effective for small particles where the effects of Brownian motion are more significant. Brownian motion is based on the notion that smaller particles will move at faster rates than large particles, at a given temperature, where all particles have equivalent kinetic energy:

$$KE = \frac{1}{2}mV^2 \tag{5.5}$$

Coupled with a cubic reduction in dielectrophoretic force with decreasing particle size, the effect of trapping small particles against Brownian motion can often be problematic. The influence of Brownian motion on particle trapping with dielectrophoresis in nanoholes is analyzed later in this chapter.

5.3 Experimental

5.3.1 Microfluidic Chip Fabrication

The microfluidic chip used in the work was assembled from several separately fabricated components. Central to the microfluidic chip is the nanohole array membrane,

shown in Figure 5.6. Arrays of circular nanoholes were fabricated by focused-ion beam (FIB) milling through a free standing, 100nm thick silicon nitride (Si_3Ni_4) membrane coated with 100 nm layer of thermally evaporated gold, held in place with a 5nm layer of thermally evaporated chromium (this fabrication was performed at Simon Fraser University 4D Labs facility by collaborating group members). All evaporation was done commercially (EMF Corp, Ithaca, NY). The general milling parameters were as follows: the gallium ion beam was set to 30 keV for milling with a beam current of 50 pA, the typical beam spot size was 10 nm, and the dwell time of the beam at one pixel was 4 ms. Each array consisted of 30 x 30 nanoholes with periodicity between 450 and 700 nm. The final membrane is shown in Figure 5.6.

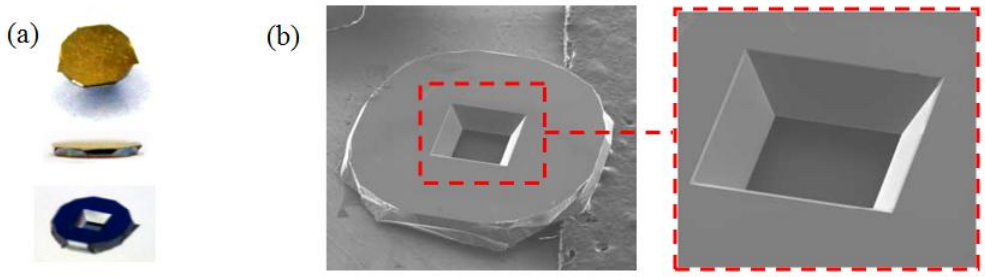

Figure 5.6: (a) Photographs showing the top, front and bottom views of a gold coated silicon nitride membrane. (b) SEM images of the underside of the silicon nitride membrane mounted on silicon frame. The membrane frame assembly has a width of roughly 3mm. The membrane window is square with sides of length 0.5mm. The larger outside square measures 0.75mm x 0.75mm.

The membrane, shown in Figure 5.6, is coated on a single side and therefore a second electrode is required for dielectrophoresis. The first electrode configuration, as shown in Figure 5.3, can be realized by coating the underside of the silicon nitride membrane with gold prior to focused ion beam milling. The second electrode configuration, as shown in Figure 5.4, on the other hand, can be realized by placing the silicon frame onto a second gold electrode as depicted in Figure 5.7. This second electrode configuration was found to facilitate electrical connections more easily and was therefore employed in all experimental work.

Membrane-to-chip electrical contacts were created using gold on glass substrates. The gold on glass substrates were fabricated using the following procedure: a 3”x1” glass slide was cut into equal halves and small through holes (~1-2mm), offset by 0.5” from

three edges, were drilled using diamond tipped drill bits. A thin layer of negative photoresist (SU-8 25; Microchem, Newton , MA) was spin-coated (Specialty Coating Systems, Indianapolis, IN) with ramping at 2,000 rpm/30 seconds on onto each prepared glass slide followed by a two-step soft bake on covered hot plates at 65ºC/5 minutes and 95ºC/10 minutes. A photomask, generated in CAD software, that defines the desired gold electrode pattern was placed onto the substrate prior to exposure under UV columnated light (Tamarack Sci., Corona, CA) for 30 seconds. The substrate then underwent a post-exposure bake at 65ºC/3 minutes and 95ºC/5 minutes before cooling and being immersed in SU-8 developer liquid (Microchem) to dissolve the unexposed portion of the photoresist. Gold (Kurt J. Lesker, Clairton, PA) was coated over the whole substrate in a two-stage process: a thin (20 nm) adhesive coating of chromium (Kurt J. Lesker, Clairton, PA) was evaporated under vacuum at 0.3-0.6 Angstoms per second, and then a substantially thicker layer (150 nm) of gold was evaporated at 0.6-0.8 Angstroms per second over the chromium layer. After cooling the substrate was soaked in an acetone bath for 2 hours to lift off the gold-coated photoresist sections, thus revealing the final microband gold electrode structure adhered to the glass substrate.

The gold on silicon nitride membrane, immobilized on a silicon frame was tightly fixed to two gold on glass substrates separated by a thin membrane of poly(dimethylsiloxane). The gold on glass substrates facilitated electrical connections to the membrane while a 300 μm thick membrane of PDMS served as an electrically insulating layer between the top and bottom gold contacts. Chip-to-instrument electrical connections were completed by attaching external wires to gold contacts using silver conductive epoxy (MG Chemical, Toronto, Ontario). Electrical signals were delivered to the membrane using an Agilent 33220A waveform generator (Agilent, Santa Clara, CA).

The chip was finished by integrating a poly(dimethylsiloxane), or PDMS, layer containing a microchannels and inlet ports fabricated by soft lithography rapid prototyping [Duffy et al. (1998)]. This PDMS layer facilitated all fluidic connections to the chip, carrying fluid to the nanohole array. A second PDMS layer to carry fluid away from the nanohole array to an outlet was not employed in these experiments, but would likely be helpful in later stages of development.

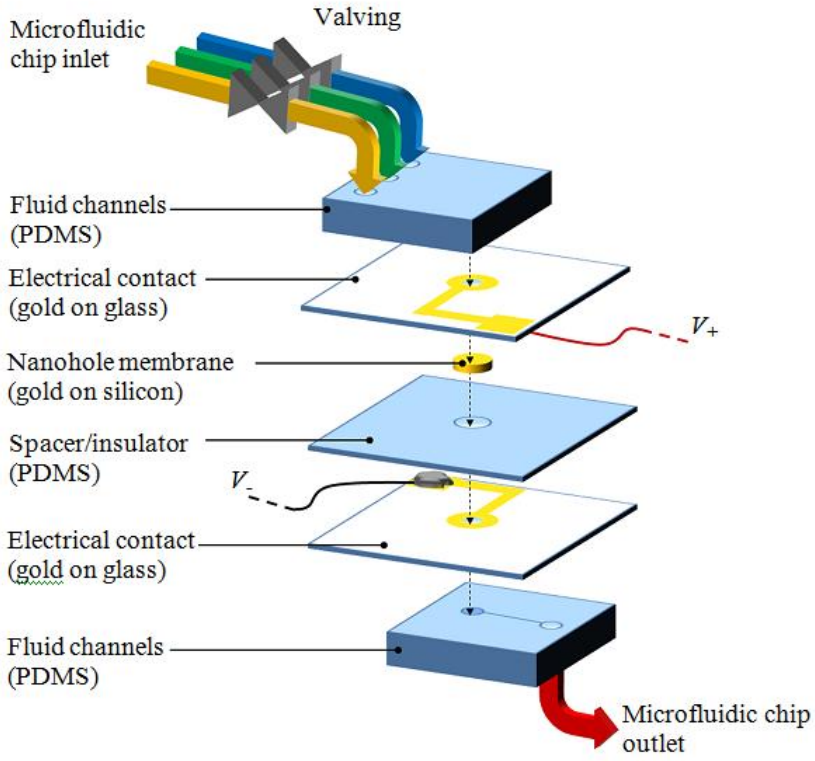

Figure 5.7: The microfluidic chip assembly accommodates multiple inlet ports for wetting the membrane, controlling membrane pressure, and delivering nanoparticles to the nanohole array. A silicon nitride membrane of a silicon frame was gold coated and focus ion beam (FIB) milled to produce nanohole arrays.

5.3.2 Sample Preparation and Visualization

Filtered 1mM fluorescein aqueous solution was used as the working fluid for flow visualization experiments. Ethanol anhydrous (Sigma-Aldrich) was used to induce wetting in the microfluidic chip before introducing fluorescein, using pressure driven flow provided by flow rate controlled syringe pumps (PHD 2000, Harvard Apparatus) via Teflon Tubing (1/16 in. Diameter, S.P.E. Limited, North York, ON), into the reservoir below the silicon nitride side of the nanohole arrays. Once both sides of the nanohole array were wet with ethanol, which possesses a low surface tension, a pressure-regulated argon source was used to drive the fluid through the nanohole arrays, so as not to exceed the breaking pressure of the membrane (~1-2 atmosphere). When connecting inlet tubing, much care was required to avoid spurious pressure sufficient to rupture the membrane.

The experimental set-up is shown in Figure 5.8 below. Fluid was injected from the underside of the microfluidic chip with all visualization done from above. Digital images were captured using a Regita 1300i CCD camera (QImaging, Surrey, BC) in combination with a Leica DM/LM microscope (Leica Microsystems Inc., Richmond Hill, ON).

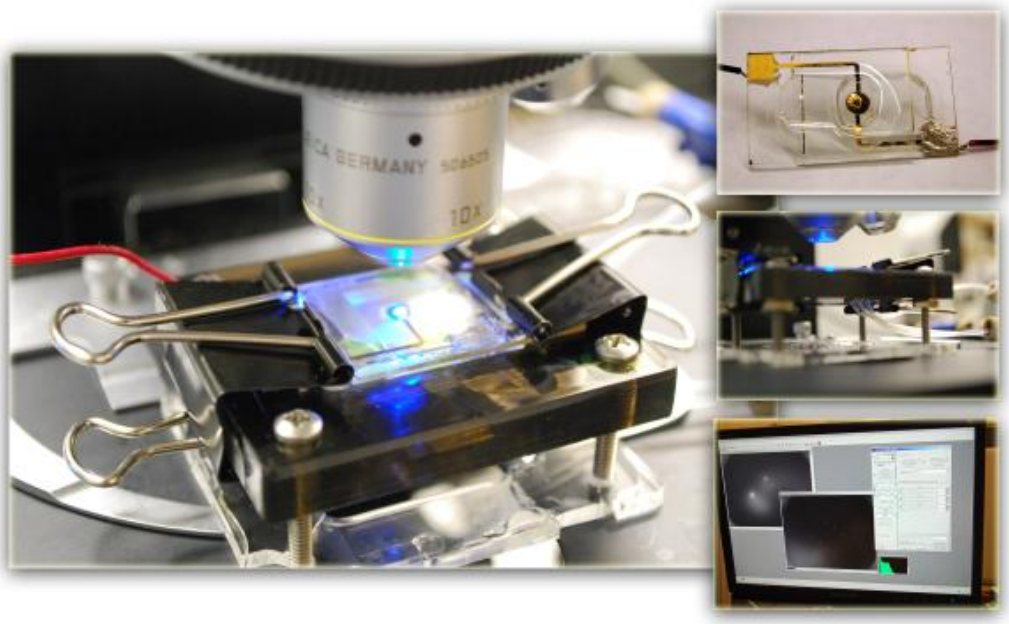

Figure 5.8: Particles are detected as they emerge onto the gold surface of the nanohole membrane using fluorescence microscopy. The microchip (top right), tubing connections (middle right) and software user interface (bottom right) are inset as shown.

5.4 Results and Discussion

As particles approach the nanohole array they are subject to dielectrophoretic force and hydrodynamic drag while undergoing Brownian motion. Particles trapped inside nanoholes, however, benefit from spatial constriction in two degrees of freedom leaving them free to move only axially along the nanohole, reducing the influence of Brownian motion, as shown in Figure 5.9a. To quantify the relative effects of DEP and Brownian motion, the condition where DEP potential exceeds the thermal energy is given by the integration of the DEP force equation [Washizu et al. (1994)]:

$$2\pi r_p^3 \epsilon_m \epsilon_0 Re[K(\omega)] E_{rms}^2 \geq \frac{1}{2} kT \tag{5.6}$$

where k is the Boltzmann constant and T is temperature. Here, Brownian motion is confined to a single degree of freedom. Assuming idealized dielectric and conducting particles, the electric field strength required to trap particles against Brownian motion are summarized in Figure 5.9b. When compared with the electric field strengths generated by both electrode configurations, we see that both configurations are capable of overwhelming Brownian motion when the particle diameter is greater than 50 nm. When the particle experiences more degrees of freedom, the minimum particle size will increase.

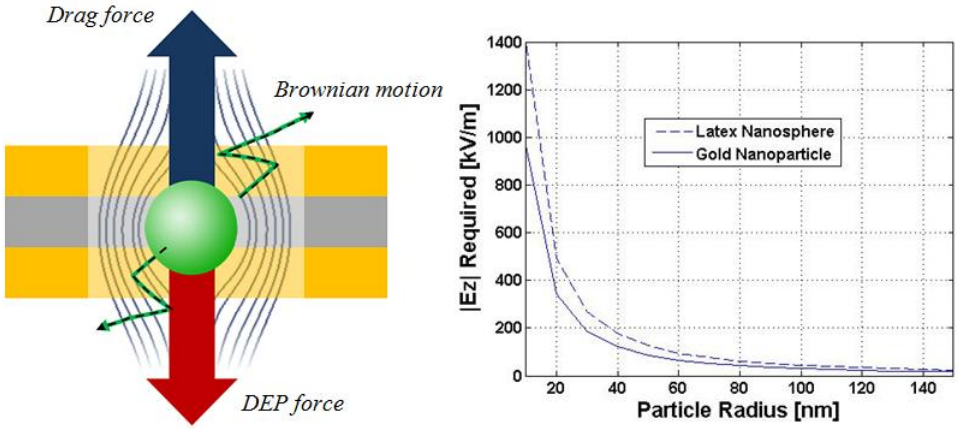

Figure 5.9: (a) Nanoparticles experience hydrodynamic drag and dielectrophoretic forces and undergo Brownian motion. (b) The electric field strength required to negate Brownian motion for a variety of particle sizes is also shown both for the cases of gold nano-particles in positive dielectrophoresis and latex nano-particles in negative dielectrophoresis.

Similarly, an effective flow velocity (or flow rate per nanohole) can be determined by equating dielectrophoretic force with hydrodynamic drag force. For the case of negative dielectrophoresis, where particles are located outside of the nanohole, the force balance is given as:

$$2\pi r_p^3 \epsilon_m \epsilon_0 Re[K(\omega)] \nabla E_{rms}^2 \geq 6\pi\mu r_p V \tag{5.7}$$

Figure 5.10 shows the results of this force balance, as a function of particle diameter, for conducting (gold) nanoparticles and dielectric (latex) nanoparticles for configuration 1 (Figure 5.10a) and configuration 2 (Figure 5.10b). The shape of the plot is noteworthy,

indicating that the maximum allowable flow rate increases proportionally with particle radius squared. Typical flow rates per hole shown in the plots correspond to flow rates per array on the order of 10 nL/hr (configuration 1) and 0.1 nL/hr (configuration 2). These flow rates are compatible with the flow rate ranges of interest as prescribed by biomarker transport and membrane strength [Eftekhari (2009)] and therefore dielectrophoretic trapping is shown here to be viable in these systems.

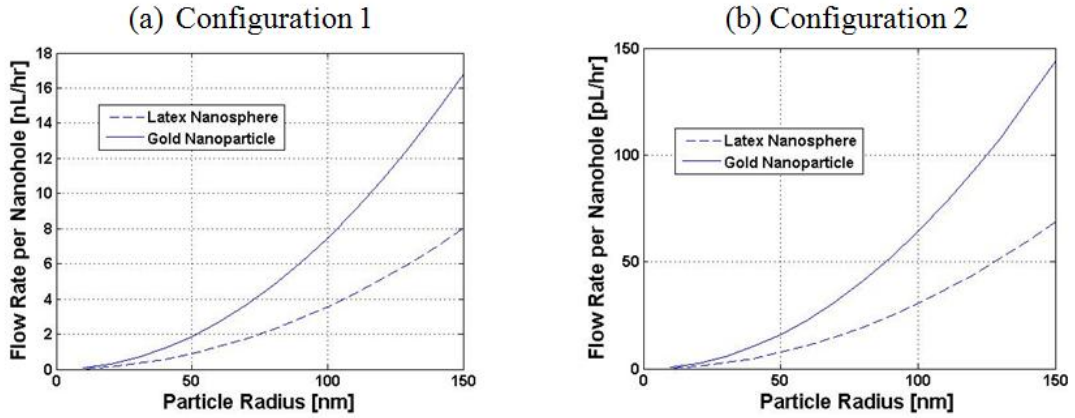

Figure 5.10: Computational results showing the maximum allowable flow rate per nanohole as a function of particle size using (a) an applied voltage of 400 mV with the first electrode configuration and (b) an applied voltage of 10V for the second configuration. In both cases, an aqueous solution with conductivity of 50 mS/cm was used; relatively high ion concentration was desired to reduce EDL thickness and thus minimize unwanted electrostatic repulsion.

Operation of the nanohole membrane was investigated through preliminary flow-through experiments using fluoroscein solution. The progression of flow through the nanohole membrane is shown in Figure 5.11 below. Pressures of 10 psi were sufficient to drive flow through the nanohole arrays. The fluorescent streams observed exiting from the nanohole array enter an ethanol environment and subsequent movement of the streams was due to thermal and surface tension related currents in a much larger ethanol environment. In an all microfluidic/nanofluidic environment, these oscillations would not be present [Eftekhari (2009)].

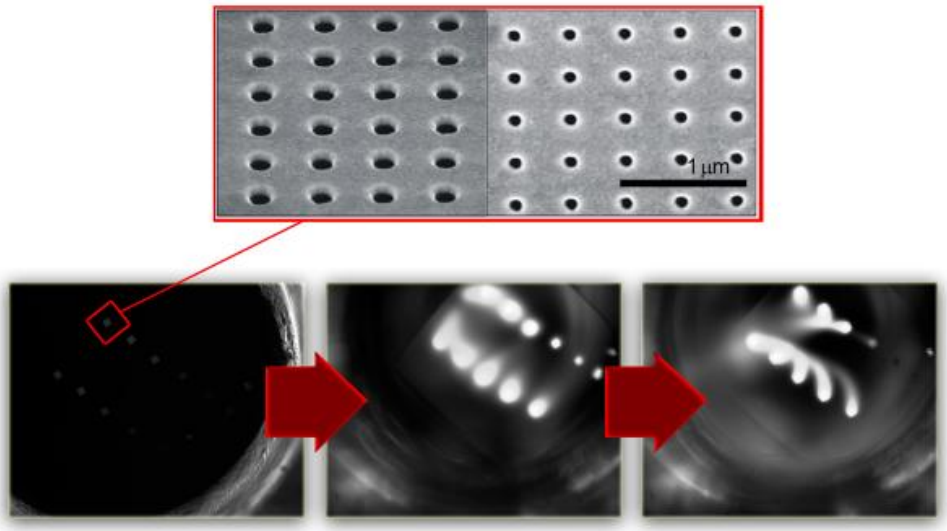

Figure 5.11: (a) Time lapsed images of fluorescein emerging from an array of nanohole arrays under an applied pressure of 10 psi. (b) A magnified Scanning electron microscope (SEM) image of the nanoholes is shown.

For a 10 psi pressure drop across the membrane containing 240 nanoholes (measuring 300 nm in diameter), flow rates per nanohole on the order of roughly 4µL/hr can be expected, and seems appropriate given experimental observations. This value exceeds the maximum allowable flow rate permitted for dielectrophoretic trapping or sieving but could easily be reduced to accommodate trapping, particularly when larger particles are used.

This experiment was repeated with fluorescent, polystyrene microspheres that were 100nm in diameter. At an applied pressure of 10 psi, no fluorescent microspheres were observed to flow through the nanohole array. Possible reasons for the apparent hindered particle transport include: electrostatic repulsion between electrical double layers surrounding both particles and nano-pores; conglomeration of microspheres and subsequent clogging of nanoholes; a weak fluorescent signal from particles emerging from the nanohole arrays; and the creation conical hole geometries during the FIB milling process which would result in characteristic dimensions that are smaller than anticipated. In the case of undesired electrostatic interactions, these could be further reduced by increasing the relative size difference between particles and nanoholes, or by increasing the concentration of the bulk solution, thus reducing the size of electrical double layers.

Given the size limitations imposed through DEP scaling, increasing the size of the nanoholes is more favourable than reducing particle size. An increase in hole size to 400 nm would enhance flow-through transport of larger particles without significant degradation in optical sensing through direct light transmission. The use of gold nanoparticles would also create stronger dielectrophoretic trapping forces than polystyrene particles, and would extend to the utility of the device to SERS based sensing.

5.5 Summary

When the nanoholes are considered as nanochannels, that is, if the nanoholes are through-holes, rapid diffusive transport on the nanoscale may be exploited and a solution sieving action is possible. Considering nanohole perforated gold film as an electrode, the application of dielectrophoresis to influence particle transport in flow-through nanohole arrays was examined. Two electrode configurations were developed and studied using analytical and numerical methods. It was found that resulting dielectrophoretic forces were equivalent to drag forces with flow rates ranging from 0.1 – 10 nL/hr per hole. The confinement of particles within nanoholes using the proposed configuration reduces the effects of Brownian motion, and thus dielectrophoretic trapping of particles as small 50 nm in a quiescent medium is shown to be viable. These simulations indicate that equivalent dielectrophoretic forces are compatible with drag forces for flow rates in the range defined in the context of biomarker transport and membrane strength considerations. Importantly, these results suggest that dielectrophoretic trapping is viable in these systems, provided issues such as particle agglomeration and membrane clogging can be effectively mitigated.

Successful flow-through experiments using fluoroscein solution served as preliminary proof of concept for flow-through operation with sub nanometers particles. Nevertheless, when larger 100nm fluorescent particles were employed, no transport of particles through the nanohole array was observed. Possible reasons for the apparent hindered particle transport include: electrostatic repulsion between electrical double layers surrounding both particles and nano-pores; conglomeration of microspheres and

subsequent clogging of nanoholes; a weak fluorescent signal from particles emerging from the nanohole arrays; and the creation conical hole geometries during the FIB milling process which would result in characteristic dimensions that are smaller than anticipated. The use of larger nanoholes is expected mitigate transport hindrance with little to no degradation to the dielectrophoretic force exerted on the particles of interest.

6.0 AC Electrochemical Diagnostics in Microfluidics with Audio Signals

6.1 Introduction

The use of AC fields for electrochemical (EC) detection in microfluidics [Pumera et al. (2006)] can offer several advantages over fluorescence, mass spectroscopy and other detection methods including: low cost and availability of supporting infrastructure (electronics); small size of supporting infrastructure; and the ability to interface directly with electronic signal processing and transmission. These advantages are particularly relevant to decentralized diagnostics, field testing and so-called point-of-care applications. In contrast to chapters 4 and 5, that focused on AC microfluidics inside the channel, this chapter focuses primarily on external infrastructure that enables AC microfluidic diagnostics, with particular relevance to portable device applications.

The promise of point-of-care (POC) testing is that it will allow untrained personnel to obtain rapid and accurate diagnostic test results, expediting the treatment process [Price and Kricka (2007), Kost (2002), Park and Kricka (2007), Lauks (1998)]. The inherent portability and throughput associated with microfluidic devices make them well-suited to POC applications. Most current POC devices are based on a single biomarker and provide binary (yes/no) output [Herr et al. (2007), Martinez et al. (2008)]. In order to satisfy requirements for the diagnosis or prognosis of many diseases, more quantitative and multiplexed testing is required. For such applications, effective devices will need to satisfy many constraints. Specifically, the devices will need to be small in size, be highly accurate, require minimal additional external infrastructure, facilitate complete sample extraction/preparation/analysis, be operable by untrained personnel, and be extremely low cost [Sia and Kricka (2008), Meagher et al. (2008), Yager et al. (2006), Yager et al. (2008)]. Existing technology sectors with strong track records in the delivery of high performance, low cost, portable consumer products may provide the most immediate and promising solutions.

Detection schemes that leverage existing and well-developed technologies have been recently demonstrated [Yager et al. (2008), Chin et al. (2007), Lange et al. (2006), Mandaji et al (2007), Martinez et al. (2008)]. Lange et al. [Lange et al. (2006)] employed

existing CD technology in combination with silver precipitation to detect binding events in immunoassays for developing regions using optical reflection. Martinez at al. [Martinez et al. (2008)] recently identified camera phones as means for acquisition and transfer of medical results for off-site diagnostics. In this case, colorimetric assays in combination with camera phones were used to detect glucose and protein levels in blood. Mandaji et al [Mandaji et al. (2007)] used a personal computer sound card as a data acquisition system in conjunction with a photomultiplier tube to detect fluorescence in capillary electrophoresis.

EC detection has been employed in POC applications for detection of parasite infected red blood cells [Kuttel et al. (2007)] and also for automated glucose detection and insulin injection [Huang et al. (2007)]. The combination of EC detection and electroosmotic flow enables all-electrical flow control and detection [Jackson et al. (2003)]. Although electroosmotic flow requires higher voltages, the currents are generally small, and suitably miniaturized high voltage systems have been developed [Erickson et al. (2004), Behnam et al. (2008)]. Other compatible technologies for flow control in POC applications include electrically actuated shape memory alloy valves [Vyawahare et al. (2008)], vacuum pressure induced by a simple hand operated syringe [Sia et al. (2004)], or capillary forces [Walker and Beebe (2002), Juncker et al. (2002)].

Despite the small cost and volume of microfluidic chips, applications of the technology require supporting infrastructure that is commonly bulky and orders of magnitude more expensive [Weigl et al. (2008), Kling (2006)]. Before health related microfluidic diagnostics can be applied widely, the supporting infrastructure must also be easily operable, inexpensive and widely available [Yager et al (2006), Yager et al. (2008)]. Such requirements may be more easily met by adapting existing technologies rather than developing new ones. Well established, ubiquitous technologies will not only be better understood by end users, but their capital cost is heavily discounted due to high volumes in other markets.

There were an estimated ~3.3 billion cell phones in use world-wide in 2007 [International Telecommunication Union (2007)]. This number continues to grow at a steady pace with developing countries accounting for about two-thirds of all cell phones in use worldwide [Jordans (2009)]. While laptops and mp3 players are less prevalent in

developing nations, initiatives such as the One Laptop per Child project and the Classmate PC (Intel Corp.) aim to shrink the digital divide between rich and poor [Lemon (2007)]. In 2008, market estimates suggested that 33% of the population in the US and 25% of the population in Europe own mp3 players [Apple Inc. (2009)]. To date, Apple has sold more than 163 million portable music players alone [Apple Inc. (2009)]. The relatively low cost and ubiquitous nature of these technologies presents an opportunity for POC technologies.

In this chapter electronic AC voltage signals from portable audio electronics are employed to perform on-chip electrochemical diagnostic functions. As shown in Figure 6.1, standard audio jacks (TRS connectors) connect the microfluidic chip to supporting devices. The 'play' feature of these devices outputs pre-programmed electrical signals to the on-chip electrodes, and the 'record' feature enables input, or data acquisition. The frequency response characteristics of different consumer electronic devices are measured and compared to those required of EC measurements in lab-on-chip systems. Audio device based measurements of concentration, conductivity, flow rate and particle detection are compared with more traditional test equipment.

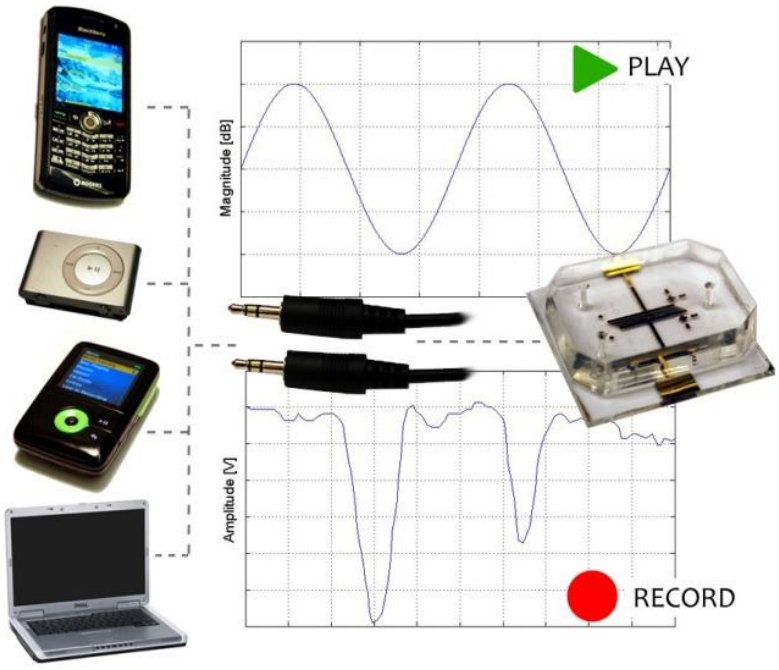

Figure 6.1: Schematic of the audio signal based electrochemical diagnostics for POC applications. Systems designed for sound generation and acquisition, such as cell phones and mp3 players, and laptop sound cards provide an inexpensive and effective means of running impedance based microfluidic tests.

6.2 Theory

6.2.1 Equivalent Circuit Modelling

Electrochemical (EC) cells are commonly modelled by electrical circuits [Hong et al. (2005)]. These electrically equivalent circuits can be used to calculate the complex impedance of an EC detector, or more generally, to characterize the electrochemical behaviour. The impedance across a pair of electrodes immersed in solution is well represented by the equivalent circuit shown in Figure 6.2.

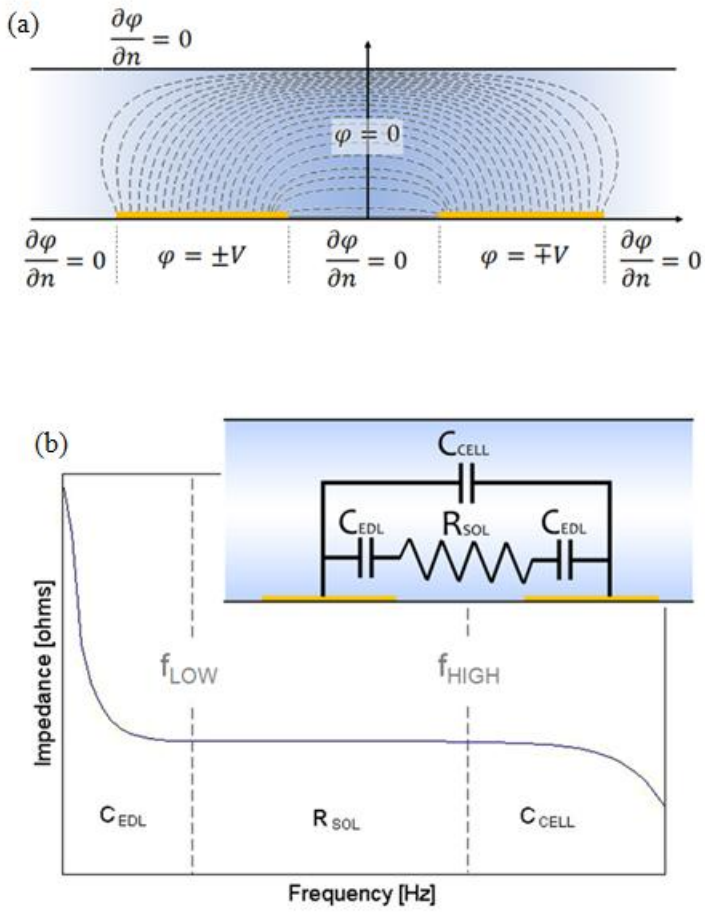

Figure 6.2: Schematic representation of: (a) microchannel geometry, electric field lines and corresponding boundary conditions. (b) The equivalent electrical circuit (right) and a plot of the impedance versus frequency relationship with the dominating circuit elements indicated over each range (left).

The bulk solution resistance, R_{Sol}, is governed by ion concentration and mobility within the solution. It is also largely governed by the geometry of the electrodes. In addition to bulk solution resistance a small parasitic resistance is also present. This resistance accounts for losses in chip-to-instrumentation connections, and is often negligible. Direct capacitive coupling between the electrodes is represented by the cell capacitance, C_{cell}. The value of C_{cell} is determined by the dielectric constant of the electrolyte and the geometry of the electrodes. The solution resistance and cell

capacitance is expressed in terms solution parameters and cell constant, K_{cell} [Timmer et al. (2002)]:

$$R_{Sol} = K_{cell}\left(\sum_i \Lambda_i C_i\right) \tag{6.1}$$

$$C_{cell} = \frac{\epsilon_r \epsilon_0}{K_{cell}} \tag{6.2}$$

where Λ_i is ion conductivity, c_i is ion concentration, ϵ_r is the relative dielectric constant of the solution, ϵ_0 is the permittivity of free space, and K_{cell} is the cell constant as determined by the electrode geometry.

When a charged surface, such as a metal electrode, is placed in contact with solution, ions from the electrolyte will accumulate near the electrode forming the electrical double layer, EDL [Hong et al. (2005)]. As described by the Gouy-Chapman-Stern model, the EDL consists of an absorbed fixed layer, known as the stern layer, that is independent of electrolyte concentration, and a diffuse layer that is concentration dependent [Probstein (2003)]. The charge distribution results in the EDL layer capacitance, C_{EDL}. The total capacitance is the sum of the stern layer capacitance, C_{Stern}, and diffuse layer capacitance, C_{Diff}, placed in series:

$$\frac{1}{C_{EDL}} = \frac{1}{C_{Stern}} + \frac{1}{C_{Diff}} \tag{6.3}$$

If the electrolyte solution is very dilute, $C_{Stern} \gg C_{Diff}$ and $C_{EDL} \approx C_{Diff}$. Similarly, if the solution is highly concentrated, $C_{Stern} \ll C_{Diff}$ and $C_{EDL} \approx C_{Stern}$ [Hong et al. (2005)]. The stern layer capacitance per unit area is typically on the order of 20μF/cm^2 [Timmer et al. (2002)]. The diffusive layer capacitance per unit area, on the other hand, is concentration dependent and varies inversely with Debye length [Timmer et al. (2002)]:

$$C_{diff} = \frac{\epsilon_r \epsilon_0}{\lambda_D} = \sqrt{\frac{2F^2 z^2 \epsilon_r \epsilon_0 C}{RT}} \tag{6.4}$$

where, z is the valence of the ion, e the electron charge, c the ion concentration, F is Faraday's constant, R is the universal gas constant, and T is temperature.

Assuming negligible resistance in all instrument-to-device connections, the remaining overall cell impedance is then [Hong et al. (2005)]:

$$Z(j\omega) = \frac{R_{Sol} + \frac{2}{j\omega\, C_{DL}}}{j\omega\, C_{cell}\left(R_{Sol} + \frac{2}{j\omega\, C_{DL}}\right) + 1} \tag{6.5}$$

The value of C_{cell} is proportional to electrode area and inversely proportional to electrode spacing. Electrode area scales with size to the second power, while electrode spacing scales with size. For this reason, microscale electrodes typically exhibit very small values of C_{cell}. The double layer capacitance will be distributed over roughly the same electrode area as C_{cell}, but is inversely proportional to the to the Debye length, which is typically only about 1 to 10 nm [Timmer et al. (2002)]. For this reason, the double layer capacitance is significantly larger than the capacitance arising from direct capacitive coupling and thus generates much lower impedance. Therefore, the flow of current will bypass the direct capacitive coupling at low to intermediate applied frequencies, where impedance will be dominated by C_{EDL} and R_{Sol} respectively. In the range of frequencies where impedance is dominated by R_{Sol}, the impedance is effectively frequency independent. The limits of the frequency independent region are partitioned by low and high cut-off frequencies. The first point of transition, the low cut-off frequency [Hong et al. (2005)], is a function of the solution resistance, R_{Sol}, and the electrical double layer capacitance, C_{EDL}:

$$f_{low} \approx \frac{1}{\pi R_{Sol}\, C_{EDL}} \tag{6.6}$$

where f_{low} is the low cut-off frequency. The second transition point takes place at higher frequencies where the impedance of C_{cell} becomes lower than R_{Sol}. Beyond the high cut-off frequency, the impedance is no longer frequency independent, but rather will decrease

with increasing frequency. This high cut-off frequency may be expressed as a function of solution resistance and cell capacitance [Hong et al. (2005)]:

$$f_{high} \approx \frac{1}{2\pi R_{Sol} \frac{C_{EDL} C_{Cell}}{C_{EDL} + 2C_{Cell}}} \tag{6.7}$$

Dependencies in each frequency range may be used to determine parameters in the equivalent circuit model. Furthermore, these parameters depend on physical phenomena within the channel. For example, counter-ions are accumulated at the electrode-electrolyte surface resulting in the screening effect, and the rate of EDL formation is influenced by flow rate. The flow rate may in turn be determined by measuring the capacitance of the EDL using frequencies below f_{low} [Han et al. (2009)]. The bulk solution resistance, on the other hand, may be used to determine the concentration of a solution with known composition using the intermediate frequency range ($f_{low} < f < f_{high}$). The same frequency range is also well suited for particle detection, where the bulk solution resistance becomes the volume weighted sum of the particle and bulk solution impedance. The direct capacitive coupling, measureable at very high frequencies ($f > f_{high}$), could be used to probe the characteristics of non-conductive solutions.

6.2.2 Coplanar Electrodes

Parallel facing electrodes offer low cell constants and have been shown to offer superior sensitivity to changes in impedance [Sun et al. (2007)]. The ease with which coplanar electrode configurations (as shown in Figure 6.2) are fabricated, however, make them more attractive candidates for POC applications. Several impedance-based analytical works have been presented for coplanar electrodes [Sun et al. (2007), Jacobs et al. (1995), Olthuis et al. (1995), Linderholm and Renaud (2005)]. The approach here follows that of Sun et al. [Sun et al. (2007)]. The coplanar electrode geometry and accompanying boundary conditions are illustrated in Figure 6.2. Dirichlet boundary conditions (Φ = constant) are applied to the electrode-solution interface and along the plane symmetrically dividing the electric field lines. Neumann boundary conditions (zero

flux) are applied at all other solid-liquid interfaces. Two successive Swartz-Christoffel mappings (SCM) are applied, mapping the original geometry into a closed, parallel plate capacitor geometry, where the cell constant can be more readily determined. The detailed transformation procedure is described elsewhere [Sun et al. (2007)]. The final cell constant for two coplanar electrodes is as follows:

$$K_{Cell} = \frac{2K(k)}{K(k')} \tag{6.8}$$

where the modulus, k, is related to the electrode lay-out, $K(k)$ is the complete elliptical integral of the first kind, and k' is the complimentary modulus. The complimentary modulus is given as:

$$k' = \sqrt{1 - k^2} \tag{6.9}$$

This method can be extended for application with interdigitated electrodes on the basis that the addition of electrode pairs are electrically equivalent to adding resistive components in parallel. Each finger in an interdigitated layout will interact with two adjacent electrodes and thus will effectively reduce the modelled electrode width by one half, in addition to reducing overall impedance by a factor of $N - 1$, where N is the number of electrode fingers in an interdigitated set. For an interdigitated electrode arrangement, the cell constant is inversely proportional to the number of electrodes:

$$K_{Cell} = \frac{2K(k)}{K(k')} \times \frac{1}{N-1} \tag{6.10}$$

where the modulus, k, is adjusted to account for the effective reduction of electrode width. Once determined, the value of K_{cell} can be used to calculate both the solution resistance, R_{Sol}, and the direct capacitive coupling term, C_{cell}.

6.3 Experimental

6.3.1 Microchip Fabrication and Assembly

All microfluidic assemblies were fabricated in-house. A complete microchip was assembled using upper and lower substrates of PDMS and gold-patterned glass, respectively.

The base substrates were gold coated microscope slides, purchased from EMF-Corp (Ithaca, NY), on which electrodes were patterned. The gold coated slides were first immersed in acetone and sonicated for 3 minutes, rinsed in isopropanol and air dried. A thin layer of negative photoresist (SU-8 10; Microchem, Newton, MA) was spin-coated (Specialty Coating Systems, Indianapolis, IN) onto the substrate with ramping at 3,000 rpm/30 s. The substrate was baked on covered contact hot plates at 65°C for 5 min and 95°C for 10 minutes. A photomask that defines the desired electrode pattern was generated in CAD software and printed by a high-resolution image setter on a transparency (Island Graphics, Victoria, BC). The substrate, placed under the photomask, was then exposed to collimated UV light (Tamarack Scientific, Corona, CA) for 60 seconds to ensure adequate polymerization of SU-8 to gold for subsequent steps. The substrate was then baked at 65°C for 5 minutes and 95°C for 10 minutes. The substrate was allowed to cool, and then immersed in SU-8 developer liquid (Microchem) to dissolve the unexposed portions of the photoresist. After developing, the substrate was rinsed with isopropanol and air dried. Ethanol was added to the substrate to induce wetting between small SU-8 features in the subsequent etching steps. Gold etchant (Transene Company, Danvers, MA) was carefully added to the substrate using an eye dropper to preserve the desired pattern and avoid excessive lateral gold etching under the SU-8 mask. The substrate was then rinsed with isopropanol and air dried. Chromium etchant (Sigma Aldrich, St. Louis, MO) was also applied using an eye dropper, following a pre-wetting step with ethanol, to remove the chromium adhesion layer. Substrates were then rinsed in isopropanol and air dried. With etching complete, the substrate was then immersed in Remover PG (Microchem) to remove the cross linked SU-8 mask.

The top substrate was fabricated by replica moulding in poly(dimethylsiloxane) (PDMS; Dow Corning, Midland, MI), following established soft-lithography protocols

[Duffy et al. (1998)]. The specific equipment and procedure employed is detailed elsewhere [Coleman et al. (2006)]. Holes for inlet and outlet tubing were punched in the PDMS prior to assembly. Both PDMS and glass surfaces were plasma-treated (Harrick Scientific, Pleasantville, NY) for 30 seconds to yield silanol surface groups that covalently bind glass to PDMS to render hydrophilic channel walls. The PDMS channels were aligned on top of the electrodes, leaving the external gold contacts exposed. Lastly, external wires were attached to the gold contacts using silver conductive epoxy (MG Chemical, Toronto, Canada). As shown in Figure 6.3, three different electrode configurations were fabricated; each configuration corresponding to a different measurand (conductivity, flow rate, and particle count).

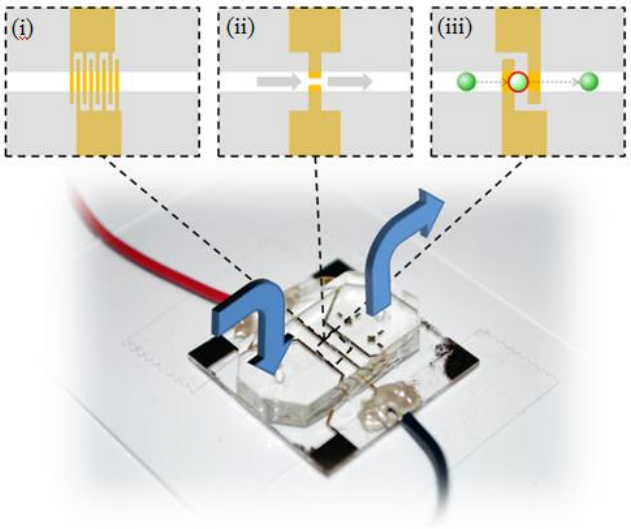

Figure 6.3: Schematic of completed chip layout with various bottom substrate electrode layouts use for conductivity (i), flow rate (ii), and particle counting (iii) measurements.

6.3.2 Solution Preparation and Delivery

Fresh sodium hydroxide (NaOH) solutions were prepared using de-ionized water and sodium hydroxide tablets (ACP Chemical, Montreal, Quebec). For particle counting experiments, high conductivity solutions were used to maximize the impedance fluctuations resulting from the transport of polystyrene microspheres through the detection zone. Dry fluorescent polystyrene microspheres (Duke Scientific, Fremont, CA), 32μm in diameter were wet with ethanol to prevent agglomeration before being combined with solution.

Once prepared, all solutions were loaded into 1mL disposable syringes (Becton-Dickenson, Franklin Lakes New Jersey). Fluid delivery was accomplished using positive pressure at the inlet induced by syringe pumps (PHD 2000; Harvard Apparatus, Holliston, MA) via Teflon tubing (1/16 in. Diameter; S.P.E. Limited, North York, ON, Canada).

6.3.3 Impedance Measurement Hardware Specifications

To connect audio devices to the microfluidic chip, standard audio cables with TRS connections, as employed in headphones or microphones, were used. Chip connections can be made by permanently soldering wires to the bottom substrate or by fitting the chip with female TRS jacks. Several consumer electronics were employed: (i) a laptop (Dell Inspiron model 1720, Round Rock, TX) with built-in SigmaTel 9200 HD audio card, Austin, TX); (ii) a mp3 audio player/recorder (Creative Zen, 2 GB, V Plus, Creative Technology, Singapore); (iii) a cellular phone (Blackberry Pearl 8100, Waterloo, ON); and (iv) a compact mp3 audio player (2^{nd} generation, 1 GB iPod Shuffle, Cupertino, California). Devices were connected using standard audio cables with 3.5mm TRS connectors on the audio device end, and stripped insulation to reveal conductors for connection on the chip-end.

Current across the electrodes was inferred from the measured voltage drop across a 5kΩ resistor placed in series with the microchannel. To accommodate the otherwise low input impedance of the consumer electronics, a unity gain buffer amplifier was integrated in-line. Such amplifiers are widely available, analog, inexpensive (< 1USD) and compactly packaged as microelectronic components.

Results obtained with the audio electronic equipment were compared with benchmark data produced using an Agilent 33220A 20MHz waveform generator for signal output (Agilent, Santa Clara, CA), and a National Instruments USB-6212 multifunction data acquisition card for signal input (National Instruments, Austin, Texas). Labview 8.0 software (National Instruments; Austin, Texas) was used to facilitate signal generation and acquisition in the case of the sound card and was used to extract all acquired signals from all other devices. Furthermore, Labview was used to generate all sound files that were later used as AC voltage excitation signals.

6.4 Results and Discussion

6.4.1 Device Characterization

Devices were characterized to determine their suitability and identify any need for calibration. The operable frequency range of most audio devices corresponds closely with the limits of human hearing: 20 Hz to 20 kHz. The Agilent 33220A waveform generator shows no detectable voltage attenuation in this frequency range and outputs signals at a sampling frequency exceeding the input sampling frequency of the audio electronics tested; in this sense it serves as an ideal voltage source benchmark for these tests. Similarly, a USB-6212 multifunction data acquisition card showed no detectable attenuation when acquiring signals in the 20Hz - 20MHz range and has a sampling frequency exceeding that output by the audio electronics employed.

Employing the function generator and data acquisition card, the input and output frequency response of each audio device was characterized with the results shown in Figure 6.4. Figure 6.4a shows the input frequency response of each device equipped with a record function (devices i, ii, and iii). The magnitude is expressed as the fraction of the maximum voltage (output or input) for the corresponding device. The laptop soundcard demonstrates the most constant input frequency response followed by the mp3 player/recorder. Figure 6.4b shows the output frequency response of each device. Both the laptop soundcard and the mp3 audio player/recorder can provide relatively constant output over the range of frequencies of interest (20Hz to 20 kHz). The compact mp3 player also provides output over this frequency range, however, it exhibits an increased output voltage bias at low frequencies corresponding to the bass audio signal. While this bias deviates from a more desirable flat frequency response, it is systematic and may be accounted for through proper calibration.

The cellular phone contained a line in/line out connection that was used to transfer electrical signals via an audio cable during testing. The lack of response from the cellular phone to frequencies over 1 kHz coupled with low signal to noise ratio, however, rule out the applicability of that device to conductivity and particle count testing at higher ion concentrations in microfluidics. Nevertheless, the broader frequency response of the

laptop soundcard and both mp3 players indicate their applicability to electrochemical lab on chip diagnostics.

The combined, input/output frequency response of the laptop and mp3 devices is plotted in Figure 6.4c. In the case of the laptop soundcard, it is possible to play and record simultaneously. In the case of the mp3 player, this is not possible and the two devices were used together; the compact player provided the voltage signal (in play mode), and the player/recorder was in audio record mode. The low range amplification bias of the compact mp3 player was apparent in the output at low frequencies, however from 400 Hz to 20 kHz, the response is relatively constant (± 0.25 dB).

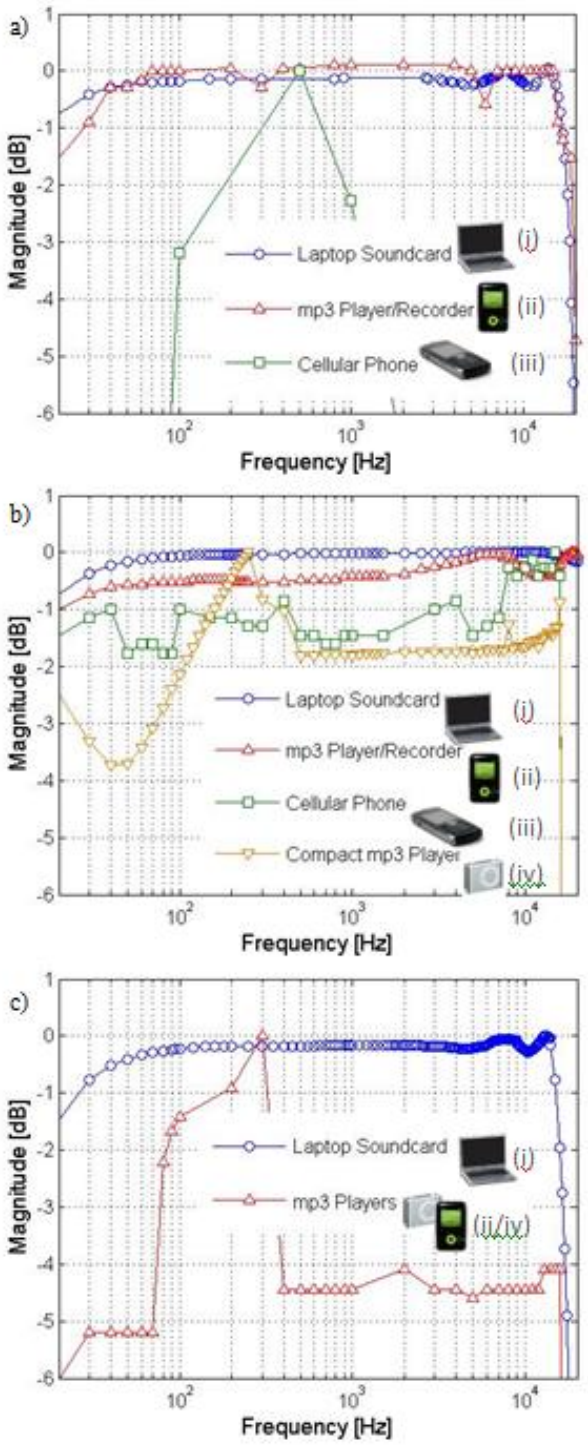

Figure 6.4: Frequency response of audio devices: (a) input frequency response of device i, ii and iii, as indicated; (b) output frequency response of device i, ii, iii and iv, as indicated; and (c) combined I/O frequency response of device i operated in full duplex and device iv operated in output (play) mode in conjunction with device ii operated in input (record) mode.

The consumer electronics tested have relatively low input impedance and thus are not well suited for impedance based measurement. As noted earlier, this shortcoming was rectified by incorporating an inexpensive high input impedance preamplifier. The excitation frequency, however, must be limited to that which can be accurately measured by the limited devices. This is known as the Nyquist criterion:

$$f_{sampling} \geq 2 \times f_{max} \tag{6.11}$$

where $f_{sampling}$ is the sampling frequency and f_{max} is corresponding maximum allowable excitation frequency. This restricts operation within frequency ranges where impedance is dominated by C_{EDL} and R_{Sol}. This restricted range conveniently corresponds to those frequencies of interest in this work. The sampling frequency offered by most soundcards and the mp3 player (device ii) is in excess of 40,000 samples per second, making them suitable for frequencies up to 20 kHz, but not suitable for measurement in the MHz frequency range where C_{cell} dominates impedance (ie. right portion of the plot in Figure 6.2b) [Hong et al. (2005)]. To make the measurements of interest here, however, only the low and intermediate frequency ranges (indicated in Figure 6.2b) are required.

6.3.2 Electrochemical Conductivity Detection

Solution conductivity, and species concentration via conductivity, may be accurately measured at frequencies where bulk solution resistance dominates overall impedance (i.e. the middle portion of the plot in Figure 6.2b). To facilitate measurements of low conductivity solutions, an interdigitated electrode was employed (as shown in Figure 6.3-i). The interdigitated structure reduces the impedance encountered across the microchannel for a given species concentration, and improves the limits of detection [Timmer et al. (2002)].

Sodium hydroxide (NaOH) solutions of varying concentration were prepared and injected into a microchannel 50μm tall and 400μm wide. The electrode pattern contained 32 interdigitated fingers, 130μm in width and spaced 75μm apart. Current measurement across the microchannel was inferred through voltage recordings across a 5kΩ resistor

placed in series with the microchannel, and all measurements were taken at no flow conditions.

Figure 6.5 shows the results of the audio-based conductivity measurements. The steep slope followed by the relatively constant impedance indicate the capacitance- and resistance-dominant regions, respectively, and a low frequency cut-off of roughly 600 Hz. The plateau region above 5 kHz is thus well-suited to probing conductivity with this setup. The results indicate the efficacy of the method in determining conductivity, or concentration via conductivity, at concentrations on the order of 0.1 – 10 mM.

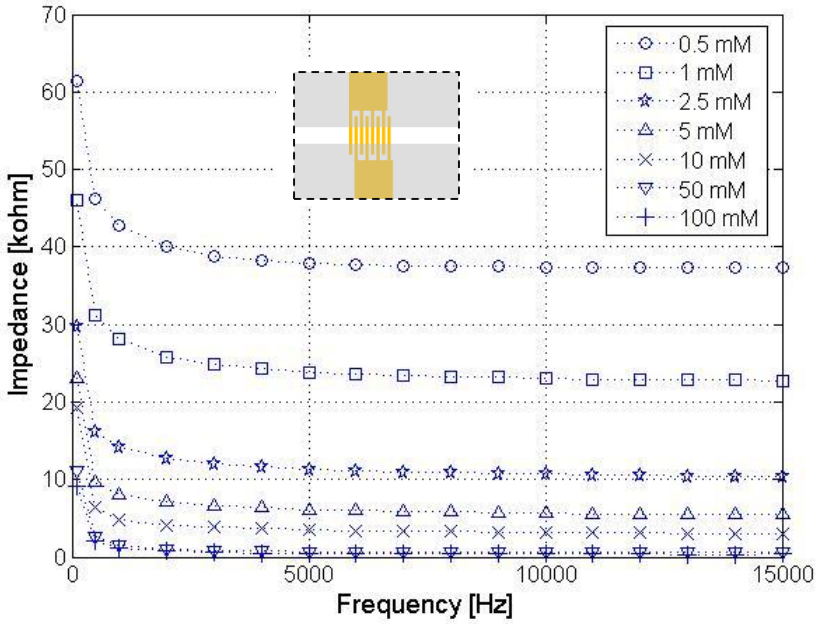

Figure 6.5: Audio signal based conductivity measurement results. Measured impedance is plotted versus frequency with the electrode and channel configuration shown inset. Higher concentration solutions exhibit higher conductivity. These results were obtained using frequency sweeps from 20 Hz to 20 kHz using both input and output via audio play/record functions of the laptop soundcard (device i). Thirty-two interdigitated electrode with widths of 70µm and spacing of 50µm extended across the microchannel and were oriented perpendicular to the direction of flow.

The impedance measurements taken using the conductivity measurement device are compared with analytically predicted impedances as shown in Figure 6.6. In the analytical model, it was assumed that NaOH dissociates completely. Molar conductivities of 5.01 x 10^3 Sm^2/mol and 19.8 x 10^3 Sm^2/mol were used for sodium and hydroxide ions respectively [Probstein (2003)].

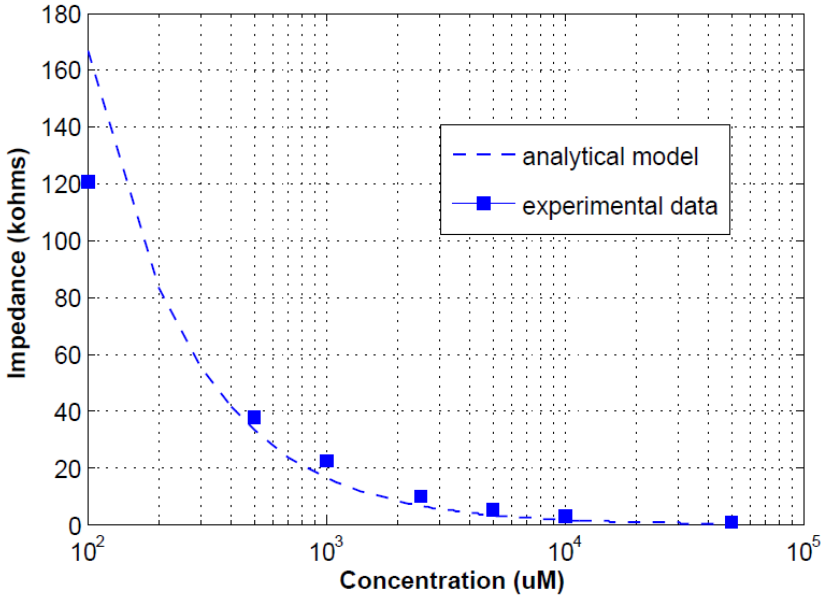

Figure 6.6: Comparison of experimentally measured impedance with that predicted by analytical modeling. Molar conductivities of 5.01 x 103 Sm2/mol and 19.8 x 103 Sm2/mol were used for dissociated sodium and hydroxide ions respectively.

Slight discrepancies between the experimental and analytical values may be the result of incomplete ion dissociation or electrode fouling between trials. Nevertheless, the analytical model and experimental data show very close correlation over a wide range of solution concentrations.

6.4.3 Flow Rate Detection

Electrical double layer capacitance is sensitive to changes in flow rate and thus flow rate measurements were performed at frequency values below the low cut-off frequency where the double layer capacitance dominates (i.e. the left portion of the plot in Figure 6.2b). Electrochemical flow rate measurement has been demonstrated previously with electrodes perpendicular [Ayliffe and Rabbitt (2003), Kjeang et al. (2007), Wu and Ye (2005)] and parallel to the flow [Collins and Lee (2004)], however, the same mechanisms of flow rate measurement apply to both configurations. Here, electrodes running parallel to the flow were employed, as shown in Figure 6.3(ii).

Results of the audio-based electrochemical flow rate measurement tests are plotted in Figure 6.6. A 50mM sodium hydroxide solution dissolved in de-ionized water

was used in combination with a 100Hz, 125mV excitation signal. The input and output signals were facilitated by the audio play and record functions of sound card (device i).

The small excitation voltages employed here negate the possibility of Faradaic reactions (i.e. transfer of electrons at the electrode-electrolyte interface). Nevertheless, the period of the applied signal, 10ms, was less than that of the charging time of the electrical double layer which is on the order of 10-100ms [Han et al. (2009)]. The result is a continuous flux of counter-ions and co-ions toward and away from the electrode surface respectively, and a corresponding increase in double layer capacitance. The applied voltage creates an oscillating surface charge at the electrode, and thus anions and cations will interchangeably assume the roles of counter-ions and co-ions. The progression of EDL formation is measured by increasing capacitance and thus reduced impedance at frequencies below the low cut-off frequency. In the case of Faradaic reactions taking place at a microelectrode, convection can be used to overcome mass transport limited reactions where large regions of depleted reactant form above electrodes, as demonstrated by previous findings and scaling laws for electrochemical velocimetry in microfluidics [Kjeang et al. (2007)]. Our findings and those of previous works [Collins and Lee (2004)] suggest that convection can also be used to overcome mass transport limitations associated with the diffusion and corresponding electrostatic attraction of ions towards an electrode-electrolyte interface. Convection of ions across electrodes is believed to increase the rate of EDL formation. The result is the decaying relationship between current and velocity, as shown in Figure 6.6.

The relationship between flow rate and measured current was non-linear, but can be approximated as linear over small flow rate ranges. While the measured current shows a consistent response to flow rate it is more sensitive at lower flow rates; particularly flow rates up to 25μL/min. Flow rates on the order of 10μL/min correspond to average velocities on the order of 10-100 mm/s, typical of many lab-on-chip applications [Auroux et al. (2002)]. The unoptimized audio-based electrochemical system employed here was capable of reliably detecting flow rates as low as 2 μL/min.

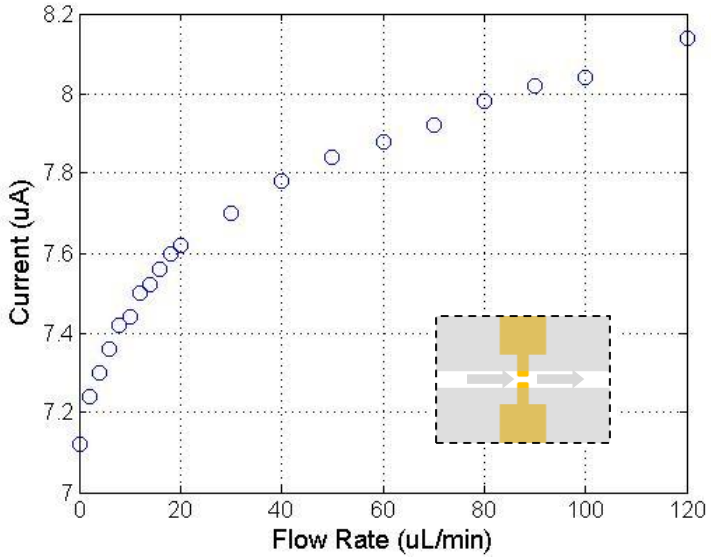

Figure 6.7: Audio signal based flow rate measurement results. Measured current values are plotted as a function of flow rate in a 400µm x 50µm cross-section microchannel with the electrode and channel configuration shown inset. The current signal was determined from the voltage recorded across a 5KΩ resistor placed in series with the microchannel. These results were obtained at a fixed frequency of 100Hz using both input and output via audio play/record functions of the laptop soundcard (device i). Electrodes 100µm in width protruded 50µm from the edges of the microfluidic channel and were oriented orthogonal to the direction of flow.

6.4.4 Particle Detection

Particles may be detected and analyzed in microsystems using optical methods, such as scattering and/or fluorescence, or by electrical methods. Optical methods, typically provide more diagnostic information than electrical methods but often must be integrated with pre-treatment steps, require much larger supporting infrastructure and are typically more expensive [Chung and Kim (2007)]. Electrochemical detection is attractive in terms of miniaturization and cost effectiveness and is thus better suited for use in portable, POC devices.

Particle detection was carried out using two gold electrodes perpendicular to the direction of flow in a microchannel (Figure 6.3-iii). The gap between electrodes (20-30µm) was minimized to maximize impedance fluctuations generated by particles passing through the detection zone. The width of the electrodes was also minimized to

increase impedance sensitivity, although this is less influential then gap size. In these experiments fabrication constraints dictated a lower limit for electrode width of 50μm.

A classical Coulter counter comprises two parallel facing electrodes separated by an aperture smaller than the area of those electrodes [Gawad et al. (2001)]. In that case, the change in impedance for a passing dielectric particle in a conductive solution is given as [Gawad et al. (2001)]:

$$\Delta R = \frac{2}{\sigma}\left[\frac{arctan\left(\sqrt{\frac{A_C}{r_p^2}}\right)}{\pi\sqrt{\frac{A_C}{\pi}-r_p^2}} - \frac{r_p}{A_c}\right] \tag{6.12}$$

where σ is the conductivity of the solution, A_c is the cross-sectional area of the aperture, and r_p is the radius of the particle. For a square 50μm x 50μm aperture and a dielectric particle in a solution with 13 mS/cm conductivity, the change in resistance for various particle diameters was determined. Based on Eq. (6.12) a particle radius of 16μm (32μm diameter) was expected to produce a detectable resistance change of 6%.

To demonstrate particle counting using audio-based diagnostics, 32μm beads were suspended in a NaCl solution with a measured conductivity of 13 mS/cm. Particle counting throughput was determined by the maximum speed at which a particle could travel through the detection zone without evading detection and the size of the detection zone. The number of particles counted per second was found by determining the minimum residence time of a particle within the detection zone needed for a count to be registered.

Figure 6.7 shows the variation in measured current as a dielectric particle flows through the detection zone. The measured current is reduced by 1.2% in response to a passing particle. This change in voltage corresponds to a 3.6% change in impedance across the electrodes. As expected this value is slightly smaller than that predicted by an idealized Coulter counter due to electric field non-uniformities created by the planar electrodes. The magnitude of the impedance change nonetheless indicates the size of the passing particle. These results demonstrated proof-of-concept particle detection using the audio-based technique.

With the audio-based voltage measurement accuracy (±0.1 mV on 1V, corresponding to a conservative signal to noise ratio of 80dB) and the high frequency cut-off (20kHz) as discussed earlier, it is possible to estimate the limits of particle counting with this technique. Specifically with reference to the classical coulter dependence, the voltage measurement accuracy limits application of the audio-based technique to particles on the order of 20µm diameter or larger. Smaller particles would require further signal conditioning or amplification.

The audio frequency response limit implies a maximum particle crossing frequency of about 1500 particles per second for particle counting. While these particle frequencies do not compare to large-scale, high through-put cell/particle sorting instruments, they are applicable to crossing frequencies in typical microchannel flows. Most notably, these results demonstrate the efficacy of audio-based diagnostics for particle detection and counting applications relevant to POC lab-on-chip systems.

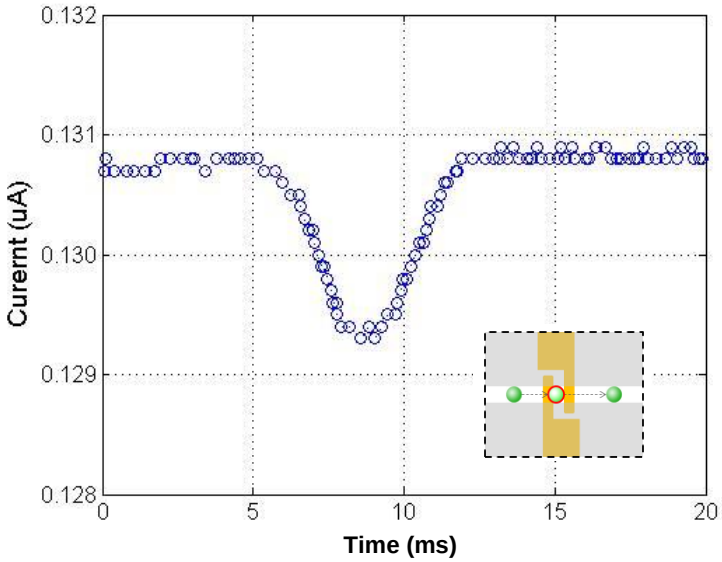

Figure 6.8: Audio signal based particle detection. Measured current is plotted versus time in as a dielectric particle flows through the detection zone with the electrode and channel configuration shown inset. These results were obtained at a frequency of 5 kHz using both input and output audio play/record functions on the laptop soundcard (device i). Electrodes with widths of 50µm extended perpendicularly across the 40µm (tall) x 50µm (wide) microfluidic channel and were spaced 20µm apart.

In practice, both the signal to be sent from the device to the chip and the resulting measured signal from the chip must be transmitted to and from an external source. The

prevailing audio file format, mp3, was found to be suitable for this application. Specifically, signal conversion to and from mp3 format resulted in negligible distortion error for single, sine waveforms in the frequency ranges used here. Thus, established methods for transmitting music files to and from portable audio devices serve the requirements of the diagnostic operations here. In the case of the portable music players, this would involve periodic synchronization of the device via a cable to an internet-connected computer. Analogous to a music 'playlist', a set of mp3 files can contain (admittedly less inspiring) signals required for a variety of on-chip tests. The corresponding recorded mp3 file list containing test data can be sent back through established means to a centralized lab for analysis. Real-time data analysis is also possible with the laptop or potentially with more advanced handheld electronics, such as smart phones.

The retail cost of materials used to fabricate microfluidic chip, excluding gold electrodes but including all chip to instrument connections, is less than 10 USD. The retail cost of supporting infrastructure including the mp3 player/recorder (~50 USD), cell phone (~100 USD) or laptop (~500 USD), is much higher than the microfluidic system, however, these devices afford the user a great deal more utility than specialized instrumentation and, most importantly, are already in widespread use. A comparable waveform generator and data acquisition card set-up would cost significantly more (~4000 USD) in addition to requiring a computer for interfacing with the data acquisition system, and a loss of portability.

6.5 Summary

AC electric fields can be leveraged to reduce both the size and cost of the external infrastructure enabling microfluidics-based tests and are thus well suited for portable applications. Microfluidic, point-of-care diagnostic technologies promise streamlined healthcare in the developed world and the delivery of much needed medical diagnostics in developing regions. The device requirements to achieve widespread use include: ease of operation for non-technical end users, low cost of device procurement, and capacity for meaningful, quantitative test results. It was demonstrated here that it is possible to

perform quantitative electrochemical measurements in a lab-on-chip platform employing the audio functions of existing consumer electronics. Specifically, the audio output (play) and input (record) signals are voltage-based and contain frequency and amplitude information.

A cell phone, laptop sound card and two mp3 players were compared, with respect to frequency response including signal to noise ratio, input and output voltage ranges, and sampling rate. Based on these measures, the cell phone performance was found to be insufficient. However, the common portable music players and laptop soundcard were found to be applicable to impedance based electrochemical diagnostics in microfluidic systems. Audio signal based conductivity/concentration (0.5mM – 100mM), flow rate (2 – 120 μL/min), and particle detection (32μm diameter) measurements were demonstrated and compared with results obtained analytically and with more traditional test equipment.

With respect to implementation, the audio signal format enables transmission of input signals to the device prior to testing, and transmission of test results to a centralized lab using established methods for transmitting music files to and from portable audio devices. The prevailing mp3 file format was found to be suitable for data transmission, although it is expected that many music file formats would also be applicable. With respect to cost, the microfluidic chip including all chip to instrument connections was roughly 10 USD, not including gold electrodes, in the absence of volume discounts. This price compares favourably to the capital cost of performing similar electrochemical tests with typical laboratory hardware (~ 4K USD). Leveraging the ubiquitous nature of audio electronics, audio signal based electrochemical diagnostics offer new opportunities for point of care diagnostics.

7.0 Conclusions and Future Work

This thesis was devoted to an investigation of the utility of electric fields in microfluidic channels for measurement and manipulation, with relevance to biomedical applications. Analytical, numerical and experimental methods were employed throughout. The contribution of this work included: (i) the development of a dielectrophoretic particle focusing device utilizing a planar electrode arrangement, (ii) a feasibility study on the use of dielectrophoresis for tuneable transport in flow-through nanohole arrays with applications in optical biosensing, and (iii) the development of a portable diagnostic system that combines audio-based consumer electronics with microfluidic chips to carry out impedance based measurements; specifically flow rate measurement, particle counting, and conductivity measurements.

7.1 Continuous DEP Based Particle Focusing Using a Planar Electrode Arrangement

A particle focusing strategy was developed that utilizes a combination of dielectrophoretic and hydrodynamic forces to focus particles using a simple, interdigitated, planar electrode arrangement constructed by single step photolithography. The scheme achieves focusing without additional fluid streams by leveraging the electric field gradients within a microchannel, and is shown to be effective in focusing both polystyrene microspheres as well as red blood cells contained in porcine whole blood.

Future experimental metrics aimed at validating the proposed model would be of benefit to this work. In particular, the dependence of particle displacement on applied voltage, frequency, flow rate and particle composition are of interest. Towards this goal, experimentation with biological samples, such as whole blood, is promising.

This focusing mechanism is well suited to both particle alignment used in cytometry and particle alignment for sample separation or pre-concentration biosensing. In either case, integration of this mechanism into a larger device with analysis capabilities

would verify the effectiveness of upstream particle pre-treatment offered by the dielectrophoretic focusing device.

7.2 DEP for Tuneable Transport in Flow-Through Nanohole Arrays

Dielectrophoretic manipulation of particle transport through metallic nanohole arrays was investigated. These nanohole arrays operate as enhanced surface plasmon resonance sensors while offering highly localized, non-uniform electric fields within each nanohole, which can be exploited for tuneable transport of nanoparticles used in conjunction with analyte. Furthermore, the use of many nanoholes in parallel offers a significantly reduced flow resistance at microfluidic to nanofluidic junctions. Numerical and analytical modeling indicate the feasibility of the proposed mechanism. Initial flow-through tests using fluorescein solution serve as preliminary proof of concept.

There are, however, many opportunities to develop this work further. The most apparent avenue of exploration is the experimental validation of dielectrophoresis based trapping with nanohole arrays using larger fluorescently stained nano-particles. Only flow-through with fluoroscein solution, containing particles on the order of a few nanometers, was reported. The effective particle size will increase and the effective pore size will decrease with the formation of electrical double layers. It is still relatively uncertain, however, exactly how much clearance between particle and pore diameters is needed to avoid all electrostatic repulsion while maintaining flow-through transport of particles sufficient for visualization; although a clearance of at least two Debye lengths is considered essential.

Use of dielectrophoresis-manipulated transport in combination with current microfluidics-based surface plasmon resonance sensing is a goal of this work. Pending favourable dielectrophoretic trapping of metallic nanoparticles, an extension of this work to Surface Enhanced Raman Spectroscopy (SERS) serves as a promising avenue of exploration.

7.3 AC Electrochemical Diagnostics in Microfluidics with Audio Signals

In contrast to chapters 4 and 5, that focused on leveraging non-uniform, AC electric fields inside microchannels, this chapter focused primarily on external infrastructure enabling AC microfluidic diagnostics for portable applications. The use of audio signals to achieve on-chip electrochemical diagnostic tests was demonstrated. Cell phones and mp3 players are examples of consumer electronics that output (play) and input (record) signals, are voltage-based and contain frequency and amplitude information. A cell phone, laptop sound card and two mp3 players were compared with respect to frequency response including signal to noise ratio, input and output voltage ranges, and sampling rate. Based on these measures, the cell phone performance was found to be insufficient. However, audio signals in the common portable music players and laptop soundcard operate in the range of 20 Hz to 20 KHz and were found to be applicable, as voltage input and output signals, to impedance based electrochemical measurements in microfluidic systems. Audio signal based concentration, conductivity, flow rate, and particle detection measurements were demonstrated and compared with results obtained analytically and with more traditional test equipment. The prevailing audio file format, mp3, was found to be suitable for data transmission to and from external sources, such as a centralized lab. The utility demonstrated, in combination with the ubiquitous nature of portable audio electronics, offers new opportunities for point of care diagnostics.

While audio based consumer electronics have been demonstrated in conjunction with idealized solutions and particles, further proof of concept could be demonstrated through testing with biological samples. Use of biological samples introduces problems relating to cross contamination and therefore a disposable chip separate from more expensive integrated electronics would be beneficial. Such a device would likely consist of a microfluidic channel with a thin (nanometer/micron thickness) dielectric layer between electrodes and fluid carrying channels to ensure re-use of electrodes without fouling. PDMS is susceptible to non-specific adhesion from biological samples and solvent swelling and therefore, PMMA may be more suitable. Inexpensive and well-established rapid prototyping techniques are available for PMMA and therefore little

additional cost would be incurred by adopting this material in place of PDMS. Also, a portable, field-operable device would require an integrated fluid pumping mechanism such as a passive capillary or thumb operated pumping scheme. Lastly, this platform could be extended to applications requiring DC signals, such as those using faradaic reactions (ie. glucose concentration testing) using a rectifier and low voltage inverter for AC to DC and DC to AC conversion respectively.

8.0 Bibliography

Apple Inc. (2009) “Apple Reports First Quarter Results” *Apple*, 21 January 2009.

Auroux, P.A., Iossifidis, D., Reyes, D.R., Manz, A. (2002) “Micro total analysis systems: 2. Analytical standard operations and applications” *Analytical Chemistry*, 74(12), 2637-2652.

Ayliffe, H.E. and Rabbitt, R.D. (2003) “An electric impedance based microelectromechanical system flow sensor for ionic solutions” *Measurement Science and Technology*, 14(8), 1321-1327.

Becker, H. (2008) “Microfluidics: A Technology Coming of Age” *Medical Device Technology Magazine*, 19, 21-24.

Becker, H. (2009a) “Chips, money, industry, education and the killer application” *Lab on a Chip*, 9, 1659-1660.

Becker, H. (2009b) “Hype, hope and hubris: the quest for the killer application in microfluidics” *Lab on a Chip*, 9, 2119-2122.

Beebe, D., Mensing, G., Walker, G. (2002) “Physics and Applications of Microfluidics in Biology” *Annual Review of Biomedical Engineering*, 4, 261-286.

Behnam, M., Kaigala, G.V., Khorasani, M., Marshall, P, Backhouse, C.J., Elliott, D.G. (2008) “An integrated CMOS high voltage supply for lab-on-a-chip systems” *Lab on a Chip*, 8(9), 1524-1529.

Benavente, J., Ramos-Barrado, J.R., Cabeza, A. (1996) “Electrical behaviour of an inorganic film from ac to dc measurements” *Journal of Colloid and Interface Science*, 180 (1), 116-121.

Bennett, D.J., Khusid, B., James, C.D., Galambos, P.C., Okandan, M., Jacqmin, D., Acrivos, A. (2003) “Combined field-induced dielectrophoresis and phase separation for manipulating particles in microfluidics” *Journal of Applied Physics Letters*, 83, 4866-4868.

Bhattacharjee, S., Chen, J.C., Elimelech, M. (2001) “Coupled model of concentration polarization and pore transport in crossflow nanofiltration” *AICHE Journal*, 47(12), 2733-2745.

Bird, R.B., Stewart, W.E., Lightfoot, E.N. (1960) “Transport Phenomena” *John Wiley and Sons*, New York, NY.

Blakely, J.T., Gordon, R., Sinton, D. (2008) "Flow-Dependent Optofluidic Particle Trapping and Circulation" *Lab on a Chip*, 8, 1350-1356.

Carter, C.B., Norton, M.G. (2007) "Ceramic Materials: Science and Engineering" *Springer*, New York, NY.

Casanella, R., Samitier, J., Errachid, A., Madrid, C., Paytubi, S., Juarez, A. (2003) "Aggregation profile characterization in dielectrophoretic structures using bacteria and submicron latex particles", *IEEE Proceedings Nanobiotechnology*, 150, 70-74.

Childress, A.E., Elimelech, M. (2000) "Relating nanofiiltration membrane performance to membrane charge (electrokinetic) characteristics" *Environmental Science and Technology*, 34(17), 3710-3716.

Chin, C.D., Linder, V., Sia, S.K. (2007) "Lab-on-a-chip devices for global health: Past studies and future opportunities" *Lab on a Chip*, 7(1), 41-57.

Choi, S. and Park, J.K. (2008) "Sheathless Hydrophoretic Particle Focusing in a Microchannel with Exponentially Increasing Obstacle Arrays" *Analytical Chemistry*, 80, 3035-3039.

Choi, S. and Park, J.K. (2005) "Microfluidic system for dielectrophoretic separation based on trapezoidal electrode arrays" *Lab on a Chip*, 5, 1161-1167.

Chu, H., Doh, I., Cho, Y.H. (2009) "A three-dimensional (3D) particle focusing channel using the positive dielectrophoresis (pDEP) guided by a dielectric structure between two planar electrodes" *Lab on a Chip*, 9, 686-691.

Chung, T.D. and Kim, H.C. (2007) "Recent advances in miniaturized microfluidic flow cytometry for clinical use" *Electrophoresis*, 28(24), 4511-4520.

Coleman, J.T., McKechnie, J., Sinton, D., (2006) "High-efficiency electrokinetic micromixing through symmetric sequential injection and expansion", *Lab on a Chip*, 6, 1033-1039.

Collins, J. and Lee, A.P. (2004) "Microfluidic flow transducer based on the measurement of electrical admittance" *Lab on a Chip*, 4(1), 7-10.

Conlisk, A.T. (2005) "The Debye-Hückel approximation: its use in describing electroosmotic flow in micro- and nanochannels" *Electrophoresis*, 26, 1896-1912.

Cook, R.L, Lucia, F.C.D, Helminger, P. (1974) "Molecular force field and structure of water: Recent microwave results" *Journal of Molecular Spectroscopy*, 53(1), 62-76.

Cui, L., Holmes, D., Morgan, H. (2001) "The dielectrophoretic levitation and separation of latex beads in microchips" *Electrophoresis*, 22(18), 3893-3901.

Cummings, E. and Khusid, B. (2007) "Dielectrophoretic Microfluidics" *Microfluidic Technology for Miniaturized Analysis Systems*, Ed. Senturia, S.D., *Springer*, New York, NY.

Deen, W. (1998) "Analysis of Transport Phenomena" *Oxford University Press*, New York, NY.

De Leebeeck, A., Kumar, L.K.S., de Lange, V., Sinton, D., Gordon, R., Brolo, A.G. (2007) "On-Chip Surface-Based Detection with Nanohole Arrays" *Analytical Chemistry*, 79(11), 4094-4100.

Demierre, N., Braschler, T., Muller, R., Renaud, P. (2008) "Focusing and continuous separation of cells in a microfluidic device using lateral dielectrophoresis" *Sensors and Actuators B, Chemical*, 132, 388-396.

Dittrich, P.S., Schwille, P. (2003) "An integrated microfluidic system for reaction, high-sensitivity detection, and sorting of fluorescent cells and particles" *Analytical Chemistry*, 75(21), 5767-5774.

Duerr, M., Kentsch, J., Mueller, T., Schnelle, T., Stelzle, M. (2003) **"**Microdevices for manipulation and accumulation of micro- and nanoparticles by dielectrophoresis" *Electrophoresis*, 24, 722-731.

Duffy, D.C., McDonald, J.C., Schueller, O.J.A., Whitesides, G.M. (1998) "Rapid Prototyping of Microfluidic Systems in Poly(dimethylsiloxane)" *Analytical Chemistry*, 70(23), 4974-4984.

Eftekhari, F., Escobedo, C., Ferreira, J., Duan, X., Girotto, E.M., Brolo, A.G., Gordon, R., Sinton, D. (2009) "Nanoholes as Nanochannels: Flow-Through Plasmonic Sensing" *Analytical Chemistry*, 81(11), 4308-4311.

Eijkel, J.C.T. and van den Berg, A. (2005) "Nanofluidics: what is it and what can we expect from it?" *Microfluidics and Nanofluidics*, 1, 249-267.

Einstein, A. (1956) "Investigations on the Theory of the Brownian Movement" *Dover Publications*, New York, NY.

Erickson, D., Mandal, S., Yang, A.H.J., Cordovez, B. (2008) "Nanobiosensors: optofluidic, electrical and mechanical approaches to biomolecular detection at the nanoscale" *Microfluidics and Nanofluidics*, 4, 33-52.

Erickson, D., Sinton, D., Li, D. (2004) "A miniaturized high-voltage integrated power supply for portable microfluidic applications" *Lab on a Chip*, 4(2), 87-90.

Falokun, C.D., Markx, G.H. (2007) “Electrorotation of beads of immobilized cells” *Journal of Electrostatics,* 65, 475-482.

Farahi, R.H., Passian, A., Ferell, T.L., Thundat, T. (2004) “Microfluidic manipulation via Marangoni forces”, *Applied Physics Letters,* 85 (18), 4237=4329.

Farahi, R.H., Passian, A., Ferell, T.L., Thundat, T. (2005) “Marangoni forces created by surface plasmon decay”, *Optics Letters,* 30, 616-618.

Fenn, J. and Raskino, M. (2008) “Mastering the Hype Cycle: How to Choose the Right Innovation at the Right Time”, *Harvard Business Press,* Cambridge, MA.

Ferreira, J., Santos, M.J.L., Rahman, M.M., Brolo, A.G., Gordon, R., Sinton, D., Girotto, E.M. (2009) “Attomolar Protein Detection Using in-Hole Surface Plasmon Resonance” *Journal of the American Chemical Society*, 131(2), 436-437.

Gao, Z., Bobacka, J., Ivaska, A. (1993) “Electrochemical Impedance Spectroscopy of Cobalt(II)-Hexacyanoferrate Film Modified Electrodes” *Electrochimica Acta,* 38, 379-385.

Gascoyne, P. R. C.; Vykoukal, J. (2002) “Particle separation by dielectrophoresis” *Electrophoresis*, 23(13), 1973-1983.

Gawad, S., Schild, L., Renaud, P. (2001) “Micromachined impedance spectroscopy flow cytometer for cell analysis and particle sizing” *Lab on a Chip*, 1(1), 76-82.

Ghallab, Y. and Badawy, W. (2004) “Sensing methods for dielectrophoresis phenomena: from bulky instruments to lab-on-a-chip” *IEEE Circuits and Systems Magazine*, 4(3), 5-15.

Giannuzzi, L.A. and Stevie, F.A. (2005) “Introduction to Focused Ion Beams: Instrumentation, Theory, Techniques and Practice” *Springer*, New York, NY.

Gordon, R., Sinton, D., Kavanagh, K.L., Brolo, A.G. (2008) “A New Generation of Sensors Based on Extraordinary Optical Transmission” *Accounts of Chemical Research*, 41(8), 1049-1057.

Gorman, C., Cray, D., Crumley, B., Park, A. (1999) “Drugs by Design” *Time Magazine*, 11 January 1999, 153(1).

Green, N.G. and Morgan, H. (1997) “Dielectrophoretic separation of nano-particles” *Journal of Physics D: Applied Physics*, 30(11), L41-L44.

Guilbault, G.G. (1990) “Practical Fluorescence: Second Edition” *Marcel Dekker*, New Orleans, LA.

Gupta, A.K., Coelho, D., Adler, P.M. (2007) "Influence of the Stern layer on electrokinetic phenomena in porous media" *Journal of Colloid and Interface Science*, 316, 140-159.

Haberman, W.L. and Sayre, R.M. (1958) "David Taylor Model Basin" *Report No. 1143*, US Navy Department, Washington, DC.

Happel, J. and Brenner, H. (1973) "Low Reynold's Number Hydrodynamics: with Special Applications to Particulate Media" *Noordhoff International*, Leyden, Netherlands.

Han, Z.J., Morrow, R., Tay, B.K., McKenzie, D. (2009) "Time-dependent electrical double layer with blocking electrode" *Applied Physics Letters*, 94(4), 043118, 1-3.

Harrison, D.J., Fluri, K., Seiler, K., Fan, Z., Effenhauser, C.S., Manz, A. (1993) "Micromachining a Miniaturized Capillary Electrophoresis-Based Chemical Analysis System on a Chip" *Science*, 261, 895-897.

Herr, A.E., Hatch, A.V., Throckmorton, D.J., Tran, H.M., Brennan, J.S., Glannobile, W.V., Singh, A.K. (2007) "Microfluidic immunoassays as rapid saliva-based clinical diagnostics" *Proceedings of the National Academy of Sciences*, 104(13), 5268-5273.

Hogg, R., Healy, T., Fuerstenau, D.W. (1966) "Mutual Coagulation of Colloidal Dispersions" *Tranactions of the Faraday Society*, 62, 1638-1651.

Holmes, D., Morgan, H., Green, N.G. (2006): "High throughput particle analysis: Combining dielectrophoretic particle focusing with confocal optical detection" *Biosensors and Bioelectronics*, 21, 1621-1630.

Hong, J., Yoon, D.S., Kim, S.K., Kim, T.S., Kim, S., Pak, E.Y., No, K. (2005) "AC frequency characteristics of coplanar impedance sensors as design parameters" *Lab on a Chip*, 5(3), 270-279.

Howell, P.B., Golden, J.P., Hilliard, L.R., Erickson, J.S., Mott, D.R., Ligler, F.S. (2008) "Two simple and rugged designs for creating microfluidic sheath flow", *Lab on a Chip*, 8, 1097-1103.

Hu, Y.S., Chung, A.J., Cordovez, B., Erickson, D. (2009) "Enhanced on-chip SERS based biomolecular detection using electrokinettically active microwells" *Lab on a Chip*, 9, 433-439.

Huang, C.J., Chen, Y.H., Wang, C.H., Chou, T.C. Lee, G.B. (2007) "Integrated microfluidic systems for automatic glucose sensing and insulin injection" *Sensors and Actuators B-Chemical*, 122(2), 461-468.

Hughes, M. (2002) “Strategies for dielectrophoretic separation in laboratory-on-a-chip systems” *Electrophoresis*, 23(16), 2569-2582

Hughes, M.P. and Green, N.G. (2002) “The Influence of Stern Layer Conductance on the Dielectrophoretic Behaviour of Latex Nanospheres” *Journal of Colloid and Interface Science*, 250, 266-268.

Hughes, M.P., Morgan, H., Flynn, M.F. (1999) “The Dielectrophoretic Behaviour of Submicron Latex Spheres: Influence of Surface Conductance” *Journal of Colloid and Interface Science*, 220, 454-457.

Im, H., Lesuffleur, A., Lindquist, N.C., Oh, S.H. (2009) “Plasmonic Nanoholes in a Multichannel Microarray Format for Parallel Kinetic Assays and Differential Sensing” *Analytical Chemistry*, 81, 2854-2859.

International Telecommunication Union (2007) “Market Information and Statistics: 2007” *http:www.itu/ITU D/ict/statistics/at_glance/KeyTelecom99.html* (Accessed February 2, 2009)

Jackson, D.J., Naber, J.F., Roussel, T.J., Crain, M.M., Walsh, K.M., Keynton, R.S., Baldwin, R.P. (2003) “Portable high-voltage power supply and electrochemical detection circuits for microchip capillary electrophoresis” *Analytical Chemistry*, 75(14), 3643-3649.

Jacobs, P., Varlan, A., Sansen, W. (1995) “Design optimization of planar electrolytic conductivity sensors” *Medical and Biological Engineering and Computing*, 33(6), 802-810.

Jones, T.B. (2003) “Basic theory of dielectrophoresis and electrorotation” *IEEE Engineering in Medicine and Biology Magazine*, 22(6), 33-42.

Jordans, F. (2009) “World’s Poor Drive Growth in Global Cell Phone Use” *Associated Press*, 2 March 2009.

Juncker, D., Schmid, H., Drechsler, U., Wolf, H., Wolf, M., Michel, B., de Rooij, N., Delamarche, E. (2002) “Autonomous Microfluidic Capillary System” *Analytical Chemistry*, 74(24), 6139-6144.

Kamholz, A.E. (2004) “Proliferation of microfluidics in literature and intellectual property” *Lab on a Chip*, 4, 16-20.

Kamholz, A. and Yager, P. (2001) “Optical measurement of transverse molecular diffusion in a microchannel” *Biophysical Journal*, 80(4), 1967-1972.

Kang, J.S., Shim, J.K., Huh, H., Lee, Y.M. (2001) "Colloidal Adsorption of Bovine Serum Albumin on Porous Polypropylene-g-Poly(2-hydroxyethyl methacrylate) Membrane" *Langmuir*, 17(14), 4352-4359.

Kjeang, E., Roesch, B., McKechnie, J., Harrington, D.A., Djilali, N., Sinton, D. (2007) "Integrated electrochemical velocimetry for microfluidic devices" *Microfluidics and Nanofluidics*, 3(4), 403-416.

Kling, J. (2006) "Moving diagnostics from the bench to the bedside" *Nature Biotechnology*, 24(8), 891-893.

Kost, G.J. (2002) "Principles and Practice of Point-of-Care Testing" *Lippincott Williams & Wilkins*, Philadelphia, PA.

Kralj, J., Lis, M., Schmidt, M., Jensen, K. (2006) "Continuous Dielectrophoretic Size-Based Particle Sorting" *Analytical Chemistry*, 78, 5019-5025.

Kuttel, C., Nascimento, E., Demierre, M., Silva, T., Braschler, T., Renaud, P., Oliva, A.G. (2007) "Label-free detection of Babesia bovis infected red blood cells using impedance spectroscopy on a microfabricated flow cytometer" *Acta Tropica*, 102(1), 63-68.

Lange, S.A., Roth, G., Witteman, S., Lacoste, T., Vetter, A., Graessle, J., Kopta, S., Killeck, M., Breitinger, B., Wick, M., Hoerber, J.K.H., Duebel, S., Bernard, A. (2006) "Measuring biomolecular binding events with a compact disc player device" *Angewandte Chemie International Edition*, 45(2), 270-273.

Lapizco-Encinas, B.H., Davalos, R.V., Simmons, B.A., Cummings, E.B., Fintschenko, Y. (2005) "An insulator-based (electrodeless) dielectrophoretic concentrator for microbes in water" *Journal of Microbiological Methods*, 62(3), 317-326.

Lapizco-Encinas, B.H., Simmons, B.A., Cummings, E.B., Fintschenko, Y. (2004) "Insulator-based dielectrophoresis for the selective concentration and separation of live bacteria in water" *Electrophoresis*, 25, 1695-1704.

Lauks, I.R. (1998) "Microfabricated biosensors and microanalytical systems for blood analysis" *Accounts of Chemical Research*, 31(5), 317-324.

Lei, U., Huang, C.W., Chen, J., Yang, C.Y., Lo, Y.J., Wo, A., Chen, C.F., Fung, T.W. (2009) "A travelling wave dielectrophoretic pump for blood delivery" *Lab on a Chip*, 9, 1349-1356.

Lemon, S. (2007) "Three Minutes with Intel on Low-Cost Laptops" *International Data Group*, 11 June 2007.

Li, P.C.H., Harrison, D.J. (1997) "Transport, manipulation, and reaction of biological cells on-chip using electrokinetic effects" *Analytical Chemistry*, 69(8), 1564-1568.

Lin, C.H., Lee, G.B. (2003) "Micromachined flow cytometers with embedded etched optic fibers for optical detection" *Journal of Micromechanics and Microengineering*, 13(3), 447-453.

Lin, C.M., Lai, Y.S., Liu, H.P., Wo, A.M. (2008) "Microvortices and recirculating flow generated by an oscillatory microplate for microfluidic applications" *Applied Physics Letters*, 93, 133503, 1-3.

Linderholm, P. and Renaud, P. (2005) "Comment on AC frequency characteristics of coplanar impedance sensors as design parameters" *Lab on a Chip*, 5(12), 1416-1417.

Lyklema, J. (1991) "Fundamentals of Interface and Colloid Science" *Academic Press*, London, UK.

Ma, H.M., Bowman, C.N., Davis, R.H. (2000) "Membrane fouling reduction by backpulsing and surface modification" *Journal of Membrane Science*, 173(2), 191-200.

Mandaji, M., Buckup, T., Rech, R., Correia, R.R.B., Kist, T.L. (2007) "Performance of a sound card as data acquisition system and lock-in emulated by software in capillary electrophoresis" *Talanta*, 71(5), 1998-2002.

Manz, A., Graber, N., Widmer, H. (1990) "Miniaturized Total Chemical Analysis System: a Novel Concept for Chemical Sensing" *Sensors and Actuators*, B1, 244-248.

Mao, X., Lin, S., Dong, C., Huang, T. (2009): "Single-layer planar on-chip flow cytometer using microfluidic drifting based three-dimensional (3D) hydrodynamic focusing" *Lab on a Chip*, 9, 1583-1589.

Martinez, A.W., Phillips, S.T., Carrilho, E., Thomas, S.W., Sindi, H., Whitesides, G.M. (2008) "Simple telemedicine for developing regions: Camera phones and paper-based microfluidic devices for real time, off-site diagnosis" *Analytical Chemistry*, 80(10), 3699-3707.

McClain, M.A., Culbertson, C.T., Jacobson, S.C., Ramsey, J.M. (2001) "Flow cytometry of Escherichia coli on nucrifluidic devices" *Analytical Chemistry*, 73(21), 5334-5338.

McDonald, J.C., Duffy, D.C., Anderson, J.R., Chiu, D.T., Wu, H., Schueller, O.J.A., Whitesides, G.M. (2000) "Fabrication of microfluidic systems in poly(dimethylsiloxane)" *Electrophoresis*, 21, 27-40.

McKechnie, J. (2006) "Fabrication of Microfluidic Devices with Application to Membraneless Fuel Cells*" M.A.Sc Thesis*, University of Victoria.

Meagher, R.J., Hatch, A.V., Renzi, R.F., Singh, A.K. (2008) "An integrated microfluidic platform for sensitive and rapid detection of biological toxins" *Lab on a Chip,* 8(12), 2046-2053.

Molla, S. and Bhattacharjee, S. (2008) "Tunable Filtration Media Employing Alternating Current Electrokinetics" *Langmuir,* 24, 5659-5662.

Molla, S.H., Bhattacharjee, S. (2007) "Dielectrophoretic levitation in the presence of shear flow: Implications for colloidal fouling of filtration membranes" *Langmuir,* 23(21), 10618-10627.

Moore, G.A. (2002) "Crossing the Chasm: Marketing and Selling Distributed Products to Mainstream Customers" *Harper Collins Publishers,* New York, NY.

Moukheiber, Z. (1998) "A dynamite mix of chips and biotech" *Forbes Magazine,* 26 January 1998, 161(2).

Nguyen, N.T. and Wereley, S.T. (2002) "Fundamentals and applications of microfluidics" *Artech House,* Norwood, MA.

Olthuis, W., Streekstra, W., Bergveld, P. (1995) "Theoretical and experimental determination of cell constants of planar interdigitated electrolyte conductivity sensors" *Sensors and Actuators B-Chemical,* 24(1-3), 252-256.

Oskooei, A.K. (2008) "Gas-Liquid Segmented Flow Microfluidic Reactors" *M.A.Sc Thesis,* University of Victoria.

Orloff, J., Utlaut, M., Swanson, L. (2002) "High Resolution Focused Ion Beams: FIB and Its Applications" *Springer,* New York, NY.

Pamme, N., Koyama, R., Manz, A. (2003) "Counting and sizing of particles and particle agglomerates in a microfluidic device using laser light scattering: application to a particle-enhanced immunoassay" *Lab on a Chip,* 3(3), 187-192.

Park, J.Y. and Kricka, L.J. (2007) "Prospects for nano- and microtechnologies in clinical point-of-care testing" *Lab on a Chip,* 7(5), 547-549.

Pennathur, S., Meinhart, C.D., Soh, H.T. (2008) "How to exploit the features of microfluidics technology" *Lab on a Chip,* 20(8), 20-22.

Pohl, H.A. (1958) "Some effects of non-uniform fields on dielectrics" *Journal of Applied Physics,* 29, 1182-1188.

Price, C.P. and Kricka, L.J. (2007) "Improving healthcare accessibility through point-of-care technologies" *Clinical Chemistry,* 53(9), 1665-1675.

Probstein, R.F. (2003) “Physicochemical Hydrodynamics: An Introduction Second Edition” *John Wiley and Sons*, Hoboken, NJ.

Pumera, M., Merkoci, A., Alegret, S. (2006) “New materials for electrochemical sensing: Microfluidic chip platforms” *Trends in Analytical Chemistry*, 25(3), 219-235.

Raicu, V. And Popescu, A. (2008) “Integrated Molecular and Cellular Biophysics” *Springer*, New York, NY.

Rahaman, M.N. (2003) “Ceramic Processing and Sintering” *Marcel Dekker*, New York, NY.

Rice, C.L. and Whitehead, R. (1965) “Electrokinetic Flow in a Narrow Cylindrical Capillary” *Journal of Physical Chemistry*, 69, 4017-4024.

Rost, F.W.D. (1992) “Fluorescence microscopy” *Cambridge University Press*, Cambridge, UK.

Saffman, P.G. (1965) “The lift on a small sphere in a slow shear flow” *Journal of Fluid Mechanics*, 22, 385-400.

Schabas, G. (2007) “Microfluidic Self-Assembly of Quantum Dot Compound Micelles” *M.A.Sc Thesis*, University of Victoria.

Schabas, G., Yusuf, H., Moffitt, M.G., Sinton, D. (2008) “Controlled Self-Assembly of Quantum Dots and Block Copolymers in a Microfluidic Device” *Langmuir*, 24(3), 637-643.

Schoch, R.B., Han, J.,Renaud, P. (2008) “Transport phenomena in nanofluidics” *Review of Modern Physics*, 80(3), 839-884.

Sedra, A.S. and Smith K.C. (2004) “Microelectronic Circuits: Fifth Edition” *Oxford University Press*, New York, NY.

Shi, J., Mao, X., Ahmed, D., Colletti, A., Huang, T.J. (2008), “Focusing microparticles in a microfluidic channel with standing surface acoustic waves (SSAW)” *Lab on a Chip*, 8, 221-223.

Sia S.K. and Kricka, L.J. (2008) “Microfluidics and point-of-care testing” *Lab on a Chip*, 8(12), 1982-1983.

Sia, S.K., Linder, B.A., Siegel, A., Whitesides, G.M. (2004) “An integrated approach to a portable and low-cost immunoassay for resource-poor settings” *Angewandte Chemie International Edition*, 43(4), 498-502.

Walker, G.M. and Beebe, D.J. (2002) “A passive pumping method for microfluidic devices” *Lab on a Chip*, 2(3), 131-134.

Sinton, D. (2004) “Microscale flow visualization”, *Microfluidics and Nanofluidics*, 1, 2-21.

Sinton, D., Gordon, R., Brolo, A.G. (2008) “Nanohole arrays in metal films as optofluidic elements: progress and potential” *Microfluidics and Nanofluidics*, 4, 107-116.

Squires, T.M. and Quake, S.R. (2005) “Microfluidics: Fluid physics at the nanoliter scale” *Review of Modern Physics*, 77(3), 977-1026.

Stephan, M.M. (2005) “Microfluidic Meets its Market” *The Scientist*, 19(10), 28-31.

Stephan, M.M. (2004) “Survival in the microfluidics market” *The Scientist*, 18(11), 38-40.

Sun T., Green, N.G., Gawad, S., Morgan, H. (2007) “Analytical electric field and sensitivity analysis for two microfluidic impedance cytometer designs” *IET Nanobiotechnology*, 1(5), 69-79.

Szymezyk, A., Sbai, M., Fievet, P. (2005) “Analysis of the pressure-induced potential arising through composite membranes with selective surface layers” *Langmuir*, 21(5), 1818-1826.

Tabeling, P. (2006) “Introduction to Microfluidics” *Oxford University Press*, New York, NY.

Terry , S.C., Jerman, Angell, J.B. (1979) “A gas chromatographic air analyzer on a silicon wafer” *IEEE Transactions on Electronic Devices*, 26(12), 1880-1886.

Timmer, B., Sparreboom, W., Olthuis, W., Bergveld, P., van den Berg, A. (2002) “Optimization of an electrolyte conductivity detector for measuring low ion concentrations” *Lab on a Chip*, 2(2), 121-124.

Tong, H.D., Jansen, H.V., Gadgil, V.J., Bostan, G.C., Berenschot, E., van Rijn, C.J.M., Elwenspoek, M. (2004) “Silicon Nitride Nanosieve Membrane” *Nano Letters*, 4(2), 283-287.

Tsiper, E.V. and Soos Z.G. (2002) “Electronic polarization at surfaces and thin films of organic molecular crystal: PTCDA” *Chemical Physics Letters*, 360(1-2), 47-52.

Tung, Y.C., Zhang, M., Lin, C.T., Kurabayashi, K., Skerlos, S.J. (2004) “PDMS-based opto-fluidic micro flow cytometer with two-colour, multi-angle fluorescence detection capability using PIN photodiodes” *Sensors and Actuators B-Chemical*, 98(2-3), 356-367.

Vogel, S. (2003) “Comparative Biomechanics: Life’s Physical World” *Princeton University Press*, Princeton, NJ.

Vyawahare, S., Sitaula, S., Martin, S., Adalian, D., Scherer, A. (2008) "Electronic control of elastomeric microfluidic circuits with shape memory actuators" *Lab on a Chip*, 8(9), 1530-1535.

Wakiya, S. (1957) "Viscous Flow Past a Spheroid" *Journal of the Physical Society of Japan*, 12(10), 1130-1141.

Wang, S.S., Jiao, Z.J., Huang, X.Y., Yang, C., Nguyen, N.T. (2009) "Acoustically induced bubbles in a microfluidic channel for mixing enhancement" *Microfluidics and Nanofluidics*, 6, 847-852.

Wang, Z., Hansen, O., Petersen, P., Rogeberg, A., Kutter, J.P., Bang, D.D., Wolff, A. (2006) "Dielectrophoresis microsystem with integrated flow cytometers for on-line monitoring of sorting efficiency", *Electrophoresis*, 27(24), 5081-5092.

Wang, X.L., Tsuru, T., Togo, M., Nakao, S.L. and Kimura, S. (1995) "Transport of Organic Electrolytes with Electrostatic and Steric-Hindrance Effects through Nanofiltration Membranes" *Journal of Chemical Engineering of Japan*, 28(4), 372-380.

Washizu, M., Suzuki, S., Kurosawa, O., Nishizaka, T., Shinohara, T. (1994) "Molecular Dielectrophoresis of Biopolymers" *IEEE Transactions of Industry Applications*, 30(4), 835-843.

Washizu, M. and Kurosawa, O. (1990) "Electrostatic manipulation of DNA in microfabricated structures" *IEEE Transactions on Industry Applications*, 26(6), 1165-1172.

Weigl, B., Domingo, G., LaBarre, P., Gerlach, J. (2008) "Towards non- and minimally instrumented, microfluidics-based diagnostic devices" *Lab on a Chip*, 8(12), 1999-2014.

White, F.M. (2003) "Fluid Mechanics: Fifth Edition" *McGraw-Hill*, New York, NY.

Whitesides, G.M. (2006) "The origins and future of microfluidics" *Nature*, 442, 369-373.

Wu, Z. znd Nguyen, N.T. (2005) "Convection-diffusion transport in parallel lamination micromixers" *Microfluidics and Nanofluidics*, 1, 208-217.

Wu, J. and Ye, J. (2005) "Micro flow sensor based on two closely spaced amperometric sensors" *Lab on a Chip*, 5(12), 1344-1347.

Yager, P., Edwards, T., Fu, E., Helton, K., Nelson, K., Tam, M.R., Wiegl, B.H. (2006) "Microfluidic diagnostic technologies for global public health" *Nature*, 442(7101), 412-418.

Yager, P., Domingo, G.J., Gerdes, J. (2008) "Point-of-care diagnostics for global health" *Annual Review of Biomedical Engineering*, 10, 107-144.

Yao, B., Luo G.A., Feng, X., Wang, W., Chen, L.X., Wang, Y.M. (2004) "A microfluidic device based on gravity and electric force driving for flow cytometry and fluorescence activated cell sorting" *Lab on a Chip*, 4(6), 603-607.

Yu, C., Vykoukal, J., Vykoukal, D.M., Schwartz, J.A., Shi, L., Gascoyne, P.R.C. (2005) "A Three-Dimensional Dielectrophoretic Particle Focusing Channel for Microcytometry Applications" *Journal of Microelectromechanical Systems*, 14, 480-487.

Zhang, C., Khoshmanesh, K., Mitchell, A., Kalantar-zadeh, K. (2009) "Dielectrophoresis for manipulation of micro/nano particles in microfluidic systems" *Analytical and Bioanalytical Chemistry*, Online July 4, 2009.

Zhang, X., Sun, C., Fang, N. (2004) "Manufacturing at Nanoscale: Top-Down, Bottom-Up and System Engineering", *Journal of Nanoparticle Research*, 6(1), 125-130.

Zheng, L., Li, S., Brody, J.P., Burke, P.J. (2004) "Manipulating Nanoparticles in Solution with Electrically Contacted Nanotubes Using Dielectrophoresis" *Langmuir*, 20, 8612-8619.